



**Carlos Alberto
Bastos de Oliveira**

**Estudo de Monte Carlo da electroluminescência em
detectores gasosos**

**Monte Carlo study of electroluminescence in
gaseous detectors**

Tese apresentada à Universidade de Aveiro para cumprimento dos requisitos necessários à obtenção do grau de Doutor em Física, realizada sob a orientação científica do Doutor João Filipe Calapez de Albuquerque Veloso, Professor Auxiliar do Departamento de Física da Universidade de Aveiro e co-orientação do Doutor António Luís Campos de Sousa Ferreira, Professor Associado do Departamento de Física da Universidade de Aveiro.

Apoio financeiro do POCTI no âmbito
do III Quadro Comunitário de Apoio.

Apoio financeiro da FCT e do FSE no
âmbito do III Quadro Comunitário de
Apoio.

À minha mãe.

o júri

presidente

Prof. Doutor António Ferreira Pereira de Melo
professor catedrático da Universidade de Aveiro

Prof. Doutor Joaquim Marques Ferreira dos Santos
professor catedrático da Faculdade de Ciências e Tecnologia da Universidade de Coimbra

Prof. Doutor Juan José Gómez Cadenas
professor de investigación do Conselho Superior de Investigaciones Científicas do Instituto de Física Corpuscular (IFIC), València, España

Prof. Doutora Maria Luísa Carvalho Leonardo
professora associada com agregação da Faculdade de Ciências da Universidade de Lisboa

Prof. Doutor António Luís Campos de Sousa Ferreira
professor associado da Universidade de Aveiro (Co-orientador)

Prof. Doutor João Filipe Calapez de Albuquerque Veloso
professor auxiliar da Universidade de Aveiro (Orientador)

agradecimentos

Durante os últimos quatro anos muitas foram as pessoas que contribuíram, directa ou indirectamente, para o sucesso do meu doutoramento. É chegada a hora de lhes dirigir algumas palavras.

Agradeço em primeiro lugar ao Professor Doutor João Veloso por me ter proporcionado a oportunidade de fazer parte da sua equipa – a DRIM *team* – e de sempre ter feito todos os possíveis para que as minhas condições de trabalho fossem as melhores. Por, além de partilhar a sua grande capacidade científica, me oferecer a sua amizade, o meu muito obrigado.

Agradeço também ao Professor Doutor António Luís Ferreira por ter aceitado a co-orientação dos meus trabalhos, por todo o suporte científico e encorajamento.

Obrigado pelo contínuo ambiente de grande companheirismo, entreajuda e boa disposição proporcionados pela DRIM *team*. Obrigado em especial ao Arouca, à Ana, à Andréa, ao Hugo, ao Lipe, ao Carlitos, à Lara, ao Daniel, ao Moutinho, ao Pedro.

Agradeço também a preciosa ajuda dos Doutores Alain Bellerive e Peter Gumpfinger na iniciação a algumas das plataformas de simulação que deram origem a este trabalho. Obrigado ao Doutor Rob Veenhof pela partilha de todo o seu conhecimento, pela ajuda na utilização do Garfield e pelas *brainstormings*. Obrigado ao Heinrich Schindler por toda a ajuda dispensada na programação em C++. Uma palavra de agradecimento vai também para o Doutor Stephen Biagi pelo seu apoio na utilização do programa Magboltz e pelo esforço colocado na actualização das secções eficazes dos gases estudados. Obrigado ao Doutor David Nygren pelas suas sugestões e pelo apoio na revisão deste documento.

Porque em momentos difíceis me apoiou, acreditou em mim e acabou por lançar a semente da investigação, obrigado ao Professor Doutor Ricardo Dias.

Agradeço à Maria Clara pelo afecto e por suportar os bons e os maus humores.

Por todos os momentos de alegria, obrigado ao meu sobrinho, Tiago. As palavras mais especiais vão para a minha mãe, Clara, e irmão, Pedro. Juntos vencemos grandes barreiras da vida, nem sempre fáceis. Juntos chegámos onde ninguém pensou um dia ser possível, nem mesmo nós! No fundo, superámo-nos... Mas não acaba aqui!

palavras-chave

Deriva de electrões, gases nobres, electroluminescência, detectores gasosos baseados em micro-estruturas, experiência NEXT.

resumo

Uma descrição detalhada do processo de electroluminescência é um pré-requisito na optimização de detectores gasosos para sistemas de imagiologia, astrofísica, física de altas energias e experiências de eventos raros.

Neste trabalho, é apresentada e caracterizada uma nova e versátil plataforma de simulação da emissão de luz durante a deriva de electrões em gases nobres, desenvolvida usando os programas Magboltz e Garfield. Propriedades intrínsecas da electroluminescência em gases nobres são calculadas e apresentadas em função do campo eléctrico aplicado, nomeadamente eficiências, rendimento e flutuações estatísticas associadas. São obtidos resultados em grande concordância com dados experimentais e simulações Monte Carlo anteriores.

A plataforma é usada para determinar as condições óptimas de funcionamento de detectores como o NEXT (*Neutrino Experiment with a Xenon TPC*) e outros baseados nas micro-estruturas GEM (*Gas Electron Multiplier*) e MHSP (*Micro-Hole & Strip Plate*).

keywords

Electron drift, noble gases, electroluminescence, micro-pattern gaseous detectors, NEXT experiment.

abstract

A good understanding of electroluminescence is a prerequisite when optimizing gaseous detectors for imaging systems, astrophysics, high energy physics and rare event experiments.

In this work, a new versatile simulation toolkit for calculating the emission of light through electron impact on noble gases, developed using the Magboltz and Garfield programs, is presented and characterized. Intrinsic electroluminescence properties of noble gases, such as efficiencies, yield and associated statistical fluctuations are calculated and presented as a function of the electric field. Excellent agreement with experiment and with early Monte Carlo simulations is obtained.

The toolkit is used to determine optimal operation conditions of detectors such as NEXT (Neutrino Experiment with a Xenon TPC) and those based in the GEM (Gas Electron Multiplier) and MHSP (Micro-Hole & Strip Plate) micro-structures.

Publicações e comunicações no âmbito desta Tese de Doutoramento

Publicações em jornais internacionais com arbitragem científica

C. A. B. Oliveira, H. Schindler, R. Veenhof, S. Biagi, C. M. B. Monteiro, J. M. F. dos Santos, A. L. Ferreira, J. F. C. A. Veloso. "A simulation toolkit for electroluminescence assessment in rare event experiments". *Physics Letters B*, vol. 703, pp 217 - 222, 2011.

C. A. B. Oliveira, M. Sorel, J. Martin-Albo, J. J. Gomez-Cadenas, A. L. Ferreira and J. F. C. A. Veloso. "Energy resolution studies for NEXT". *Journal of Instrumentation*, vol. 6, pp P05007, 2011.

J. F. C. A. Veloso, C. D. R. Azevedo, **C. A. B. Oliveira**, H. N. da Luz, A.L. Ferreira and J. M. F. dos Santos. "Gas VUV Photosensors Operating Face-to-Face". *Nuclear Instruments and Methods in Physics Research A*, vol. 610, pp. 238 - 241, 2009.

Publicações em actas de encontros científicos com arbitragem científica

C. D. R. Azevedo, **C. A. B. Oliveira**, H. Natal da Luz, A. L. Ferreira, J. M. F. Dos Santos, J. F. C. A. Veloso. "HpXe Gas VUV Photosensors Operating Face-to-Face". *IEEE Nuclear Science Symposium / Medical Imaging Conference Record*, pp. 960 - 964, October 19 - 25, 2008.

C. D. R. Azevedo, **C. A. B. Oliveira**, H. Natal da Luz, A. L. Ferreira, J. M. F. dos Santos and J. F. C. A. Veloso. "Development of a HpXe Hybrid Gamma Detector Aiming Scintigraphy". *IEEE Nuclear Science Symposium Conference Record*, vol.2, pp.1612 - 1617, October 26 - Nov. 3, 2007.

Outras publicações

The NEXT collaboration. "The NEXT-100 experiment for neutrinoless double beta decay searches (Conceptual Design Report)". arXiv:1106.3630v1 [physics.ins-det].

Apresentações orais em encontros internacionais com arbitragem científica

C. A. B. Oliveira, on behalf of the NEXT Collaboration. "The NEXT experiment at the LSC". Accepted for presentation at the 13th ICATPP Conference on Astroparticle, Particle, Space Physics and Detectors for Physics Applications, Villa Olmo, Como, Italy, 3 - 7 October, 2011.

C. A. B. Oliveira, A. L. Ferreira, J. F. C. A. Veloso, S. F. Biagi, R. Veenhof, J. M. F. dos Santos, C. M. B. Monteiro. "Electroluminescence assessment in micropattern gaseous avalanche detectors". NSSMIC2009 - Nuclear Science Symposium and Medical Imaging Conference, Orlando, Florida, USA, 25 - 31 October, 2009.

J. F. C. A. Veloso, H. Natal da Luz, **C. A. B Oliveira**, J. M. Maia, C. M. B. Monteiro, A. C. S. S. Bento, J. M. F. dos Santos. "Simultaneous readout of secondary charge and scintillation from GEM avalanches". *NSSMIC2008 - IEEE Nuclear Science Symposium and Medical Imaging Conference*, Dresden, Germany, October 19-25, 2008.

Apresentações orais em reuniões de colaborações internacionais

CERN - RD51 collaboration

C. A. B. Oliveira, A. L. Ferreira, S. Biagi, R. Veenhof, J. F. C. A. Veloso. "First simulation approach for Ar & Xe electroluminescence in the NIR region". *7th RD51 Collaboration Meeting*, CERN, Geneva, Switzerland, 13 - 15 April, 2011.

C. A. B. Oliveira, A. L. Ferreira, S. Biagi, R. Veenhof, J. M. F. dos Santos, C. M. B. Monteiro, D. Nygren, J. F. C. A. Veloso. "Update on EL simulations in noble gases using Garfield and Magboltz 7.1". *6th RD51 Collaboration Meeting*, Bari, Italy, 7 - 10 October, 2010.

C. A. B. Oliveira, A. L. Ferreira, J. F. C. A. Veloso, S. Biagi, R. Veenhof, J. M. F. dos Santos, C. M. B. Monteiro. "Electroluminescence in noble gases using Garfield and Magboltz 7.1" - *5th RD51 Collaboration Meeting*, Freiburg, Germany, 24 - 27 May, 2010.

C. A. B. Oliveira, A. L. Ferreira, J. F. C. A. Veloso, S. Biagi, R. Veenhof, J. M. F. dos Santos, C. M. B. Monteiro. "Xenon electroluminescence assessment in uniform field geometry and GEM using Garfield and Magboltz" - *4th RD51 Collaboration Meeting*, CERN, Geneva, Switzerland, 23 - 25 November, 2009.

C.A.B. Oliveira, A. L. Ferreira, J. F. C. A. Veloso, S. F. Biagi and R. Veenhof. "Simulation tool for electroluminescence assessment in gaseous avalanche detectors" - *3rd RD51 Collaboration Meeting*, Crete, Greece, June 16 – 17, 2009.

NEXT collaboration

C. A. B. Oliveira, A. L. Ferreira, S. Biagi, R. Veenhof, J. M. F. dos Santos, C. M. B. Monteiro, D. Nygren, J. F. C. A. Veloso. "Electroluminescence simulations in noble gases using Garfield and Magboltz 7.1" - *NEXT Collaboration Meeting*, Gandia, Spain, September 29 - October 1, 2010.

Posters em encontros internacionais com arbitragem científica

C. A. B. Oliveira, P. M. M. Correia, R. Veenhof, A. L. Ferreira, J. F. C. A. Veloso. "Electroluminescence Properties in Micropattern Gaseous Detectors: a Simulation Study Considering Charging-up Effect". Accepted for presentation at the *2011 IEEE Nuclear Science Symposium and Medical Imaging Conference*, Valencia, Spain, October 23 - 29, 2011.

C. A. B. Oliveira, A. L. Ferreira, J. F. C. A. Veloso, S. F. Biagi and R. Veenhof. "Simulation tool for electroluminescence assessment in gaseous avalanche detectors". *MPGD2009 1st International Conference on Micro Pattern Gaseous Detectors*, Kolympari, Crete, Greece, 12 - 15 June, 2009.

C. D. R. Azevedo, **C. A. B. Oliveira**, H. Natal da Luz, A. L. Ferreira, J. M. F. dos Santos and J. F. C. A. Veloso. "Gas VUV Photosensors Operating Face-to-Face at HpXe" - *2008 IEEE Nuclear Science Symposium and Medical Imaging Conference*, Dresden, Germany, October 19 - 25, 2008.

J. F. C. A. Veloso, C. D. R. Azevedo, **C. A. B. Oliveira**, H. Natal da Luz, A. L. Ferreira and J. M. F. dos Santos. "Gas VUV Photosensors Operating Face-to-Face". *5th International Conference on New Developments In Photodetection*, Aix-les-Bains, France, June 15 - 20, 2008.

J. F. C. A. Veloso, C. D. R. Azevedo, **C. A. B. Oliveira**, A. L. Ferreira and J. M. F. dos Santos. "Development of a HpXe Hybrid Gamma Detector Aiming Scintigraphy". *2007 IEEE Nuclear Science Symposium and Medical Imaging Conference*, Honolulu, Hawaii October 28 - November 3, 2007.

Outras comunicações

C. A. B. Oliveira. "Noble gases electroluminescence simulations for rare event experiments". Poster presented at *CLASHEP 2011 - Latin-American School of High-Energy Physics*, Natal, Brazil, March 23 - April 5, 2011.

C. A. B. Oliveira. "Development of simulation platforms for MPGDs". Oral presentation at *MAP-Fis PhD research conference*, Braga, Portugal, January 16 - 17, 2009.

Contents

List of Acronyms	5
Introduction	7
1 Gaseous detectors	13
1.1 Interaction of particles with matter	16
1.1.1 Gamma-rays	17
1.1.2 Fast electrons	19
1.1.3 W -value and the Fano factor	20
1.2 Detecting particles without amplification	21
1.2.1 Diffusion, recombination and attachment	22
1.2.2 Ionization Chamber	24
1.3 Detecting particles using amplification	24
1.3.1 Charge amplification	24
1.3.1.1 Proportional Counter	26
1.3.1.2 Multiwire Proportional Chamber	27
1.3.1.3 Time Projection Chamber	29
1.3.1.4 Micro-pattern Gaseous Detectors	30
Micro-Strip Plate	31
Gas Electron Multiplier	32
Micro-Hole & Strip Plate	34
1.3.2 Electroluminescence amplification	35
1.3.2.1 Gas Scintillation Proportional Counter	36
1.3.2.2 Scintillation Drift Chamber	38
1.3.3 Hybrid concepts	38
1.3.3.1 GSPC/MSGC hybrid detector	39
1.3.3.2 2D-MHSP GSPC gamma camera	40
1.3.3.3 PACEM	41
1.4 Energy Resolution	43
2 Electroluminescence process	45
2.1 Atomic energy structure of noble gases	47
2.2 Electroluminescence modes	50
2.3 VUV emission	52
2.4 Visible and Infra-Red emission	56

3 Simulation toolkit	57
3.1 Garfield	59
3.2 Magboltz	60
Electron transport	60
Null-collision technique	62
Anisotropic scattering	66
3.3 C++ toolkit	66
Simulation of EL	67
4 EL in uniform electric field	69
4.1 Simulation details	71
4.2 Collision rates	71
4.3 Energy distribution	73
4.4 Excitation efficiency	74
4.5 Intrinsic properties of VUV EL	76
4.5.1 VUV EL efficiency	76
4.5.2 VUV EL yield	77
4.5.3 Fluctuations	80
4.6 Vis-IR EL yield	82
4.7 Discussion	86
5 VUV EL in a cylindrical geometry	89
5.1 Simulation details	91
5.2 EL Yield	92
5.3 Fluctuations	94
5.4 Spatial distribution of excitations	96
5.5 Discussion	96
6 VUV EL in MPGDs	99
6.1 Electric field maps	101
6.2 GEM	102
6.2.1 Simulation details	102
6.2.2 VUV EL yield	103
6.2.3 Spatial distribution of excitations	105
6.2.4 Number of VUV photons vs number of electrons	107
6.3 MHSP	108
6.3.1 Simulation details	108
6.3.2 VUV EL yield	109
6.3.3 Spatial distribution of excitations	110
6.4 Discussion	110
7 NEXT - Neutrino Experiment with a Xenon TPC	113
7.1 NEXT & $\beta\beta^{0\nu}$ decay searches	115
7.2 Simulation details	116
7.3 VUV EL yield	117
7.4 Fluctuations and energy resolution	117
MWPC as an alternative VUV EL amplification stage . .	121

CONTENTS	3
-----------------	----------

7.5 Discussion	123
8 Conclusions & future work	125
8.1 Conclusions	127
8.2 Future work	129
A Cross sections used by Magboltz 8.9.5	133
B Toolkit C++ code and illustrative script	141
Bibliography	145

List of Acronyms

- $\beta\beta^{0\nu}$ – Neutrinoless double beta decay
- CF₄ – Tetrafluoromethane
- COMPASS – CCommon Muon Proton Apparatus for Structure and Spectroscopy
- DMA – Dimethylamine
- GEM – Gas Electron Multiplier
- EL – Electroluminescence
- FEM – Finite Element Method
- FWHM – Full Width at Half Maximum
- GEM – Gas Electron Multiplier
- GPM – Gaseous Photomultiplier
- GSPC – Gas Scintillation Proportional Counter
- IBF – Ion backflow
- LAAPD – Large Area Avalanche Photodiode
- LHC – Large Hadron Collider
- MHSP – Micro-Hole & Strip Plate
- MPGD – Micro-pattern Gaseous Detector
- MSGC – Micro-Strip Gas Chamber
- MSP – Micro Strip Plate
- MWPC – Mutiwire Proportional Counter
- NEXT – Neutrino Experiment with a Xe TPC

- NIR – Near Infrared
- PACEM – Photon-Assisted Cascaded Electron Multiplier
- PC – Proportional Counter
- PMT – Photomultiplier Tube
- RICH – Ring Imaging Cherenkov
- R&D – Research & Development
- SDC – Scintillation Drift Chamber
- SI – The International System of Units
- SNR – Signal-to-Noise Ratio
- TMA – Trimethylamine
- TOTEM – TOTal Elastic and diffractive cross section Measurement
- TPC – Time Projection Chamber
- UV – Ultraviolet
- Vis-IR – Visible-Infrared light range
- VUV – Vacuum Ultraviolet
- WIMP – Weakly Interacting Massive Particle

Introduction

Electroluminescence (EL) is an important process of signal amplification in particle gaseous detectors working with scintillating gases such as noble gases and/or CH₄ and CF₄. The process allows high gains that are very competitive when compared to those achieved when charge avalanche signals are used. In addition, the fluctuations associated with the production of secondary light (EL) are much lower than those associated with avalanches thus allowing to achieve very good energy resolutions. Using appropriate light readout systems it is also possible to integrate tracking capabilities in EL based detectors. The use of EL enables the operation of detectors without risk of sparks since the involved electric fields are much lower than those needed to produce avalanches and the amount of secondary charges, if produced, is very small. This makes EL based particle detectors very robust and stable.

Those properties of EL make it attractive for experiments with low event rates and/or high background levels, where the highest possible gain in the detector, together with outstanding energy resolution and tracking capability, are needed. Nowadays two main fields of Physics research have promoted such experiments: direct Dark Matter and neutrino-less double beta decay searches.

Weakly Interacting Massive Particles (WIMPs) are leading theoretical Dark Matter candidates. They are extremely massive and interact very weakly with normal matter. There is a great interest on the direct detection of those particles and on the measurement of the WIMP-nucleon collision cross section. With this aim, noble gas dual-phase liquid/gas Time Projection Chambers (TPCs) have been or are being developed. XENON100 [1] is a 100 Kg xenon detector currently operating in the Gran Sasso Underground Laboratory, Italy. Also in this laboratory, the WIMP Argon Programme (WARP), with argon at 87 K, is being operated [2, 3]. The Large Underground Xenon (LUX) [4] is a xenon detector and water shield that will be installed at Sanford Deep Underground Laboratory at the Homestake Mine, South Dakota. WIMPs are expected to interact with the nuclei in the dense liquid phase producing both primary scintillation and ionization. The electrons produced at this stage are driven to the gaseous phase where electroluminescence amplification happens due to a suitable electric field. In this way two light signals are obtained and the ratio between them is a unique signature of each elementary particle, which allows separating the WIMP signal from background.

During the last decade, different experiments have shown that neutrinos mix and have mass [5]. This property can be explained both by the Majorana or the Dirac nature of the neutrino. If the neutrino is a Majorana particle it is its own antiparticle and the neutrino-less double beta decay ($\beta\beta^{0\nu}$), a Standard Model forbidden process, is possible in some isotopes, including ¹³⁶Xe [6]. Besides giving an experimental proof of

the Majorana nature of neutrinos, the measurement of the half-time of the $\beta\beta^{0\nu}$ decay would allow the determination of the absolute scale of neutrino masses, a demanding and essential task in the understanding of these particles. Based in ^{136}Xe , there are two main experiments being developed for the detection of this decay. The Enriched Xenon Observatory (EXO) [7] is a detector using 200 Kg of liquid enriched Xe, currently being installed at the Waste Isolation Pilot Plant (WIPP) near Carlsbad, New Mexico, USA. The Neutrino Experiment with a Xenon TPC (NEXT) [8, 9, 10] is a 100 kg, high-pressure gaseous xenon Time Projection Chamber, approved for operation in the Canfranc Underground Laboratory (LSC), Spain. The two high energetic electrons emitted in the $\beta\beta^{0\nu}$ decay produce both primary scintillation and primary charge in the xenon volume. In EXO the primary scintillation is detected with Large Area Avalanche Photo-Diodes (LAAPDs) and the primary charge is amplified and collected by crossed-wire grids. In the case of NEXT the primary charge is amplified through the EL process and thus, both the primary scintillation and the ionization produce, ultimately, light signals to be detected with Photomultipliers (PMTs).

The high complexity and high cost of these detectors make it impossible to perform experimental R&D in the final prototypes. Thus, the understanding of the microscopic process of secondary light emission, EL, and the assessment of its different properties through detailed Monte Carlo tracking of electrons in gases, namely the yield and the corresponding fluctuations, is of great importance towards the design and construction of such detectors. With these parameters in hand, it is possible to predict the light gain and the energy resolution that are achievable with a particular detector geometry and its optimal conditions of operation.

Garfield is a widely used program for the detailed simulation of the drift of electrons in gas based detectors. It allows simulating nearly arbitrary field geometries thanks to its interfaces to finite element and boundary element methods programs. Among its various drift techniques, the Monte Carlo “microscopic technique” tracks the electrons at the molecular level using procedures and cross-sections available in Magboltz. The latest was developed to calculate the drift parameters of electrons in nearly arbitrary gas mixtures under the influence of electric and magnetic fields. It integrates an up-to-date database of electron-atom and electron-molecule cross sections for about 60 gases, obtained through detailed and careful compilation of data available in the literature. As an example, beyond cross sections for elastic collisions and ionizations, the program parametrizes the excited energy levels of argon and xenon as functions of 44 and 50 energy groups, respectively. Garfield and Magboltz are therefore extensively used and recognized by the international scientific community that develops gaseous detectors for High Energy Physics and other areas of research. Recently, an open-source and freely

available new simulation toolkit, implemented in C++ and based in these two state-of-art programs, was created. It provides a versatile and comprehensive parametrization of the microscopic physics processes involved in gaseous detectors.

The work presented in this document was developed during the design and implementation of this simulation toolkit, in close collaboration with their authors. Discussion, suggestions and benchmarking contributed for the actual form and available tools. Namely, work needed to provide the toolkit with capabilities for simulating the EL produced in gases, particularly neon, argon, krypton and xenon, was done. In the present thesis this toolkit is described and used. Simulations of the intrinsic properties of EL and detector performances, predicted by applying the method to particular geometries, namely to Micro-pattern Gaseous Detectors (MPGDs) and to NEXT, are presented.

This thesis is divided in 8 chapters. Along the document, are presented illustrations and plots which were created specially for this work, unless otherwise indicated in their caption. This includes illustrative example simulations, performed with Garfield 9, which help on the understanding of the studied microscopic processes.

Chapter 1 is intended to give some background in the physical processes involved in the studies done along the work. In a first stage, a summary of the most important interactions with matter of X- and γ -rays and fast electrons (the particles with interest in the applications considered in this work) are presented. After, the two types of signal amplification used in gaseous detectors (charge avalanches and EL) are also presented and characterized. An historical overview of the main devices using these two types of signal amplification is made. Since EL amplification is the topic of interest of this document, the most recent experimental measurements of its properties are presented.

In Chapter 2 the process of EL in pure noble gases, namely neon, argon, krypton and xenon, is reviewed. Since EL is the consequence of the de-excitation of atoms excited through electron impact, the atomic energy structure of such noble gases is shown and the decay channels of their excited states are analyzed. Infra-Red emission is addressed to atomic transitions between states in different excited shell configurations and VUV emission is addressed to excimers formed through three-body collisions of the excited atoms with the ground state atoms.

Chapter 3 describes the simulation toolkit developed and used in this work. The programs in which it is based, Garfield and Magboltz, are reviewed and their capabilities are shown. The model applied to the information about the excited atoms, produced during the drift of electrons under the effect of electric fields, is presented. With this model it is possible to predict the different EL properties, both in the Vis-IR and in the VUV regions, for a given detector setup.

In Chapter 4 the intrinsic properties of EL in pure neon, argon, krypton and xenon are assessed using the simulation toolkit. Electrons drifting in uniform electric fields are considered. This geometry, by its simplicity, allows a powerful understanding of the microscopic processes involved in EL. Properties related to the electron drift process itself, as collision rates and kinetic energy distribution as functions of the field, are presented. Regarding VUV EL, electroluminescence efficiency and yield are calculated, and the toolkit is validated by comparing the obtained results with earlier Monte Carlo simulations and measurements available in literature for argon and xenon. For the first time, the statistical intrinsic fluctuations associated with VUV EL are calculated, confirming that they are smaller than those related with primary and secondary charge production. The Vis-IR EL yield is estimated for argon and xenon by considering two initial possible approaches. Recent measured data, available in literature for argon, is compared and found to be between the considered approaches. This agreement states an initial starting point for the accurate simulation of Vis-IR light emitted after electron impact in noble gases.

Chapter 5 shows the results obtained by applying the simulation toolkit to the conditions of a cylindrical Gas Scintillation Proportional Counter, in order to extrapolate and evaluate the behavior of a plane of wires as an EL amplification device. This wire plane can overcome mechanical constraints in the construction of wide uniform electric field gaps needed at high pressures and allow the operation at lower voltages.

Also the EL produced during the avalanche developing in Micro-pattern Gaseous Detectors (MPGDs), when measured by Large Area Avalanche Photodiodes, can be a good option for signal amplification in certain applications, since it is possible to reach high gains by using low voltages. Thus, the EL response of MPGDs, namely the Gas Electron Multiplier and the Micro-Hole & Strip Plate, is estimated through simulations and compared with measurements in Chapter 6.

In Chapter 7 the simulation toolkit is used to estimate the signal response of the NEXT-EL detector and to determine the best voltages to be used. The light gain and the energy resolution which can be achieved, as a function of the applied electric field and for different photodetection efficiency scenarios, are presented.

In the conclusions, Chapter 8, the main results achieved in this work are described and some possible applications of the toolkit are presented. Future work, to be done in the sequence of this thesis, is also discussed.

CHAPTER 1

Gaseous detectors

Gaseous detectors are widely used in High Energy Physics, as well as in X-ray spectrometry and imaging systems. In general, a gaseous detector consists of a container filled with an active gas. Usually, pure noble gases or mixtures based on them are used. A schematic representation of the general gaseous detector concept is presented in Figure 1.1. An ionizing particle traversing the gas interacts with its atoms/molecules through a process that depends on the nature of the particle and on its energy (see Section 1.1 for further details). Whatever kind of particle or its energy, the final result is the production of excited and ionized molecules and/or atoms of the gas.

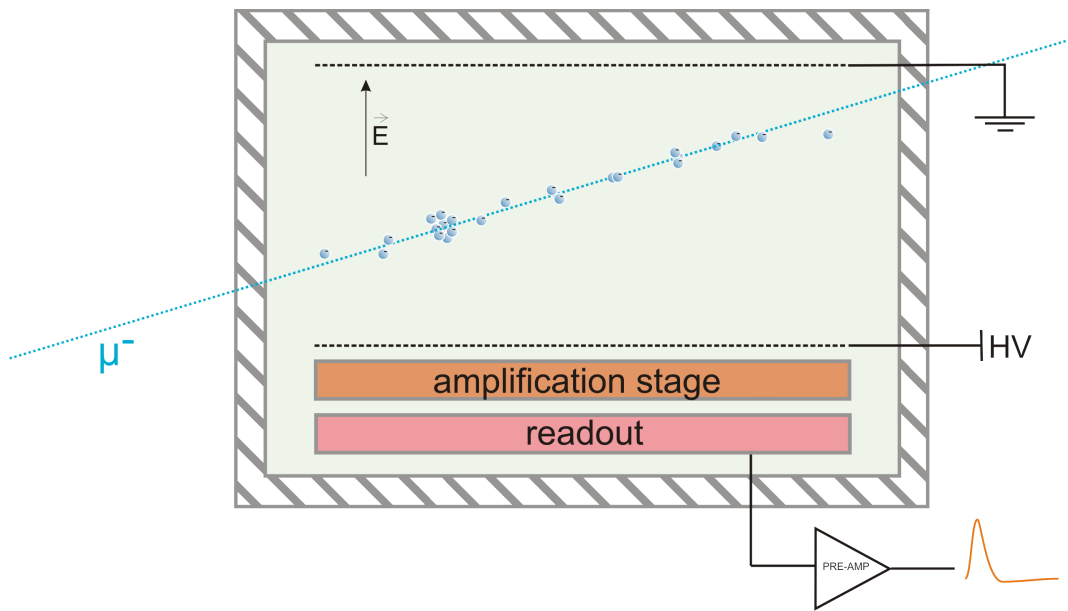


Figure 1.1: Schematic representation of a gaseous detector. A muon, e.g., traversing the detector volume and the negative charges created along its track are also represented.

Excited atoms can decay through the emission of light, usually in the range between Vacuum Ultraviolet (VUV) and Visible-Infrared (Vis-IR), producing what is called the *primary scintillation*. Although in many applications this light is not used, it can be detected with appropriate readouts and used for trigger or *start-of-event* signals. In noble gases, the de-excitation of excited atoms to the ground state happens through the intermediate formation of excimers, as explained in Chapter 2.

Each ionization produces an *ion pair* that consists in one ion and one free electron. In this way, the passage of the incoming particle leaves behind a trace or a cloud of primary charge carriers, depending on the nature of the particle. Due to their low mobility when compared with electrons, the ions produce very slow signals that are not suitable for most of the applications. Therefore, the detectors are usually developed in view of the drift of electrons and thus this document will focus the analysis on them.

If the number of primary electrons, generated by the energy deposition of the incoming particle, is high enough so that their signal is above the electronic noise, they can be directly collected without further amplification. This can be done by applying an electric field – the *drift field* – so low that electrons can collide only elastically with the gas atoms but high enough so that they don't recombine with the ions. This concept is explained in Section 1.2, where the example of the *ionization chamber* is presented.

In most of the applications, the number of primary electrons is low and can not be distinguished by the electronics or leads to poor Signal-to-Noise Ratio (SNR) signals. In this case, the primary charge signal needs to be amplified and thus the primary electrons are driven, under the effect of a drift field, to a region where higher fields are applied.

If the electric field is kept above the so-called *excitation threshold* of the gas and below the *ionization threshold*, the electrons are accelerated between collisions and gain enough energy to excite but not to ionize the gas atoms. The excited atoms, produced along the drift path of electrons, decay emitting secondary light called *electroluminescence* (EL). In this way, each primary electron can produce several photons and a measurable light signal is produced in suitable readout systems as explained in Section 1.3.2, where some examples of detectors based on EL are presented.

If the amplification field is higher than the ionization threshold, between collisions, the primary electrons gain enough energy to ionize new atoms of the gas, producing additional *ion pairs* and thus secondary electrons. Furthermore these secondary electrons can gain energy from the field and ionize more atoms. In this way, a charge avalanche is produced, ending up with a number of charge carriers orders of magnitude higher than the number of primary electrons. This amplification type is explained in Section 1.3.1 where some detectors are presented as examples. In this avalanche mode, electroluminescence is also produced since the electric field is higher than the excitation threshold.

1.1 Interaction of particles with matter

The purpose of gaseous detectors is to detect, identify, track and characterize particles. In order to design them, it is of major importance to understand in detail how the particles to be detected interact in the active volume, the gas. This Section has not the aim of covering all kinds of interactions undergone by all elementary particles. Instead it is intended to give the reader enough information about the main processes involved in the detectors and applications analyzed in this work. Considering X-ray

and / or Gamma-ray spectrometry and neutrinoless double beta decay studies the important particles to be studied are X- and Gamma-photons (for simplicity both are called in the following as γ -rays) and high-energy electrons.

1.1.1 Gamma-rays

When a mono-energetic beam with a given number of γ -rays, I_0 , passes through a gas volume with a thickness t , the number of transmitted photons, I , follows an exponential dependence with t [11]:

$$I = I_0 e^{-\mu t} \quad (1.1)$$

The *linear attenuation coefficient*, μ , is the probability per unit path length that a γ -ray is removed from the beam and includes the contributions of the three physical processes by which this can happen: *photoelectric absorption*, *Compton scattering* and *pair production*. This parameter, divided by the density of the medium, ρ , is the *mass attenuation coefficient* ($\mu_m = \mu/\rho$) which is shown in Figure 1.2 for e. g. xenon.

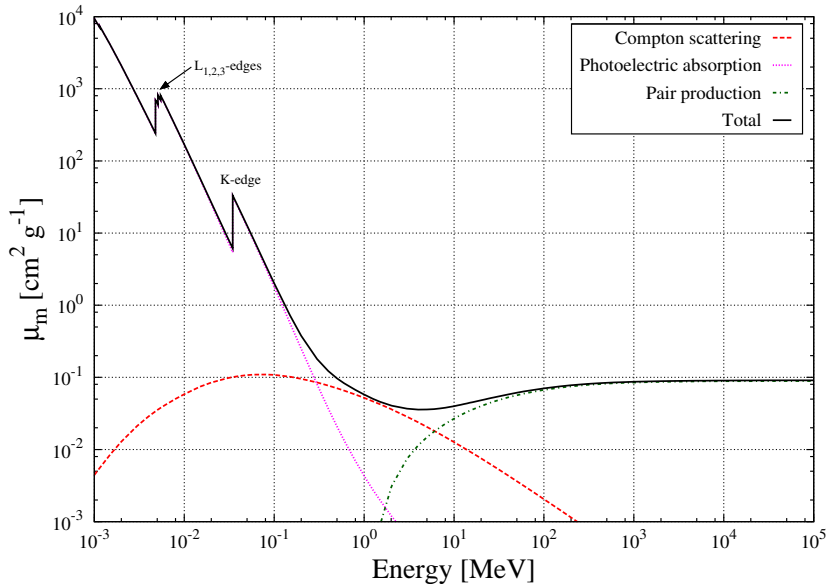


Figure 1.2: Total mass attenuation coefficient of xenon for γ -rays as a function of their energy. Partial coefficients of separated processes are also presented. The data was taken from [12].

For energies up to few hundreds of keV, involved in the applications mentioned in this work, the main process of interaction of γ -rays with the gas is the photoelectric absorption. In this process, the γ -ray ejects one electron from one shell of the atom, with higher probability for the most tightly bound K- and L-shells. The removed photoelec-

tron has an kinetic energy, E_{e^-} , given by the difference between the incoming photon energy, $h\nu$, and the binding energy of the shell where the photoelectron originated, E_b :

$$E_{e^-} = h\nu - E_b \quad (1.2)$$

The photoelectric mass attenuation coefficient (presented in Figure 1.2) is proportional to $E^{-3.5}$ [11], where E is the photon energy, but attenuation peaks are observed for energies corresponding to the binding energies of K- and L-shells. For energies slightly below each edge, only electrons in less bound shells can be removed from the atom. But, for energies slightly above, the electrons of the following shell can now be removed and therefore the probability of attenuation increases abruptly.

After the ejection of the photoelectron, the vacancy in a shell of the positive ion is quickly filled with one electron from an outer shell. This transition is accompanied by the emission of a fluorescent X-ray, with energy equal to the difference between the two shells, or by non-radiate processes as the emission of an Auger or Coster-Kronig electrons. In the latter case, the emitted electron has an energy equal to the difference between the electronic transition and the ionization energy of the shell from where the electron was emitted. If a fluorescent X-ray is produced it can be absorbed elsewhere in the gas producing additional photoelectrons.

The photoelectron ejected in the first step of the photoelectric absorption, the Auger or Coster-Kronig electrons, and the photoelectrons resulting from the absorption of fluorescent X-rays undergo several collisions in the gas. They have enough energy to ionize atoms ejecting further electrons which, in turn, have energy to produce extra ionizations. This process takes place until all electrons are thermalized and produces the *primary electron cloud*, i.e, the set of *primary electrons* that are the result of the energy deposition, in the form of ionizations, of the incoming γ -ray. During the formation of the primary cloud also excited atoms are formed, which decay by emission of photons in the range between VUV and Vis-IR, giving rise to the so-called *primary scintillation*.

As previously mentioned, the main physical process of interaction of γ -rays with matter, for the energies considered in this work is the photoelectric absorption. However it is worth to briefly describe the other two possible processes. Compton scattering is dominant for energies between 0.3 and 6 MeV and consists in the transfer of partial energy from the incident photon to an electron of the outer layers of the atom – the *recoil electron*. The photon can be deflected in any direction and therefore the Compton spectrum is a broad continuum.

For energies above twice the rest mass of the electron (1.02 MeV) it is possible to produce one electron-positron pair. This process is called *pair production* and results

from the interaction of the γ -ray with the Coulomb field of an atom's nucleus. The photon disappears and the excess energy above 1.02 MeV is transferred as kinetic energy to the electron and to the positron. The latter undergoes collisions with the medium until being thermalized and annihilated, producing two γ -photons of 511 keV each, in opposite directions.

1.1.2 Fast electrons

High-energy electrons follow a tortuous path when depositing energy in a material. Since their mass is equal to that of the orbital electrons of the atoms, a large fraction of their energy can be lost in each collision.

In addition to the Coulomb interactions (excitations and ionizations), fast electrons can lose their energy also by *bremsstrahlung*. Through this process electromagnetic radiation is emitted when the electron is inelastically deflected in the electrostatic field of the nucleous or of the orbital electrons. The *bremsstrahlung* yield increases with the electron energy being dominant for energies above few MeV.

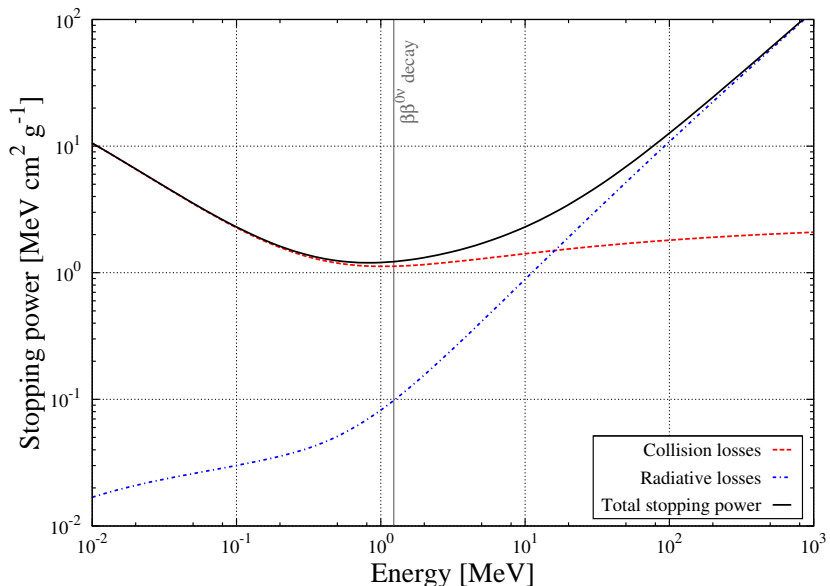


Figure 1.3: Total stopping power of xenon as a function of the electron energy. Separated contributions of the collisional and radiative losses are also shown. Values are normalized to the density of the gas. Data was taken from reference [13], where collision stopping powers are calculated from the theory of Bethe [14, 15] and radiative stopping powers are evaluated using theoretical *bremsstrahlung* cross sections described by Seltzer and Berger [16]. In the plot, it is also represented, with a gray vertical line, the energy of each of the two electrons emitted in the ${}^{136}\text{Xe}$ $\beta\beta^{0\nu}$ decay: 1.229 MeV.

The *linear stopping power*, also called *specific energy loss*, is defined as the differ-

ential energy lost in an infinitesimal path length of the particle track:

$$S(E) = -\frac{dE}{dx} \quad (1.3)$$

In Figure 1.3 it is shown the total stopping power of electrons in xenon as a function of the electron energy. It is the sum of the collisional and radiative contributions, also plotted:

$$\frac{dE}{dx} = \left(\frac{dE}{dx} \right)_c + \left(\frac{dE}{dx} \right)_r \quad (1.4)$$

The two electrons emitted in the neutrinoless double beta ($\beta\beta^{0\nu}$) decay of the ^{136}Xe isotope (a detailed description of this process is presented in Chapter 7) are examples of fast electrons, with an initial energy of 1.229 MeV each (represented in Figure 1.3 as a gray vertical line). As each electron drifts in the gas with decreasing energy, the stopping power increases and a peak of energy deposition is formed at the end of its trajectory – the *Bragg peak*. This phenomenon leads to a specific topological signature of the $\beta\beta^{0\nu}$ decay, similar to a “spaghetti with two meat balls”, as shown in Figure 1.4.

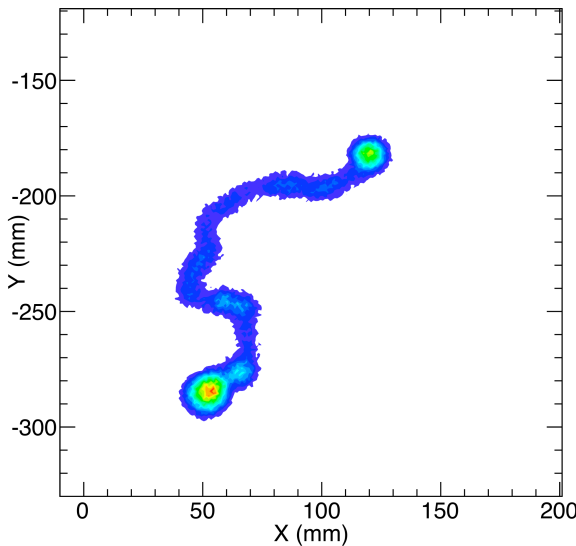


Figure 1.4: The topological signature of the $\beta\beta^{0\nu}$ decay in ^{136}Xe : a “spaghetti with two meat balls”. The track of each electron ends in a blob, corresponding to the Bragg peak. Figure retrieved from [10].

1.1.3 **W -value and the Fano factor**

Whatever the particle and the physical process by which it interacts on a gaseous detector, the practical and final result is the excitation and/or ionization of gas atoms. The de-excitation of atoms is made through emission of light that can be used as

trigger or start-of-event signal. The free electrons produced in the ionizations are the basic constituent of the electric signal developed by the detector, regardless of the amplification type.

The energy necessary to remove one electron from the less bounded shell is 21.56, 15.76, 14.00 and 12.13 eV for gaseous neon, argon, krypton and xenon, respectively [17]. However, the average energy required to produce an ion pair – the W -value – is substantially higher since other mechanisms, such as excitations, are possible: 36.6, 26.4, 24.1 and 21.9 eV for each of the gases [18, 19]. The average number of primary electrons produced by an incident particle, \bar{N}_e , will be proportional to its energy, E :

$$\bar{N}_e = \frac{E}{W} \quad (1.5)$$

Similarly, it is possible to define the mean energy, deposited by the incident particle, that is necessary to produce an excited atom and consequentially an EL photon, W_S . Values for gaseous xenon have been reported between 72 ± 6 and 111 ± 16 eV [20, 21, 22].

The number of primary electrons, N_e , produced by an incident particle is not always the same, having statistical fluctuations associated with it. If each ionization could be considered independent of the others, a Poisson process would describe these fluctuations and the variance would be $\sigma_{\text{Poisson}}^2 = \bar{N}_e$. However, it was experimentally verified that the processes that give rise to the creation of charge carriers are not independent, and the value of the observed variance is lower than that given by the Poisson distribution. For this reason it was introduced, in 1947 by U. Fano [23], the so-called *Fano factor* that is the ratio between the observed variance, σ_e^2 , and the predicted by the Poisson statistics model:

$$F = \frac{\sigma_e^2}{\bar{N}_e} \quad (1.6)$$

The literature of work measuring experimentally the Fano factor is extensive, reporting values between 0.19 and 0.23 for pure gaseous argon, between 0.17 and 0.23 for krypton and between 0.13 and 0.17 for xenon [24, 25, 26, 27, 28, 29, 30, 31, 32].

1.2 Detecting particles without amplification

The direct collection of the charge produced by an incident particle, with no additional amplification of its signal is the simplest method of detecting radiation. This process is used in *ionization chambers*, which are the simplest gas-filled detectors. Since the signal of these devices is due to the drift of the charge carriers in the gas under the effect of low electric fields, until they are collected by the electrodes, it is important to

understand the properties associated with the drift of ions and electrons.

The ions are heavy particles and thus, between collisions, are only slightly accelerated. Also due to their high mass, in each collision they lose a substantial fraction of its energy. Therefore, ions drift in gases following the field lines with only minor thermal fluctuations. Electrons are much lighter and thus can be highly accelerated between collisions. In addition, they lose only a small fraction of its energy since the ratio between their mass and the mass of the atom is very low. Therefore, their direction of motion is often changed and their path is a sinuous line with just a tendency to follow the field lines. This tendency usually increases with the increase of the field intensity.

The drift velocity of electrons is typically 1,000 times higher than that for ions, which makes the signals from electrons much faster. This is the reason why, in most of the applications, only the signal component of the electrons is used. For high radiation rates, the extremely low drift velocity of ions can even generate space charge effects distorting the electric field.

1.2.1 Diffusion, recombination and attachment

As mentioned previously, the propagation direction of electrons can be abruptly changed in each collision. Although, on average, they follow the direction of the electric field – the longitudinal direction – they diffuse transversely. A point-like primary electron cloud, drifting under the effect of a uniform electric field, spreads into a Gaussian spatial distribution (as illustrated in Figure 1.5) whose standard deviation projected into an arbitrary transverse axis, σ_x , will increase with time, t :

$$\sigma_x = \sqrt{2Dt}, \quad (1.7)$$

where D is the *transverse diffusion coefficient*.

Collisions between electrons and positive ions may result in *recombination*. In this process the electron is captured by the ion, forming a neutral atom or molecule and, therefore, does not contribute anymore to the signal collected in the detector. The frequency of the collisions leading to recombination is proportional to both the concentrations of electrons, n^- , and ions, n^+ . The recombination rate can be written using the recombination coefficient, α_{rec} :

$$\frac{dn^+}{dt} = \frac{dn^-}{dt} = -\alpha_{\text{rec}} n^+ n^- \quad (1.8)$$

There are two types of recombination: *columnar* recombination and *volume* recombination. In the first case the primary electrons are captured by positive ions still in the

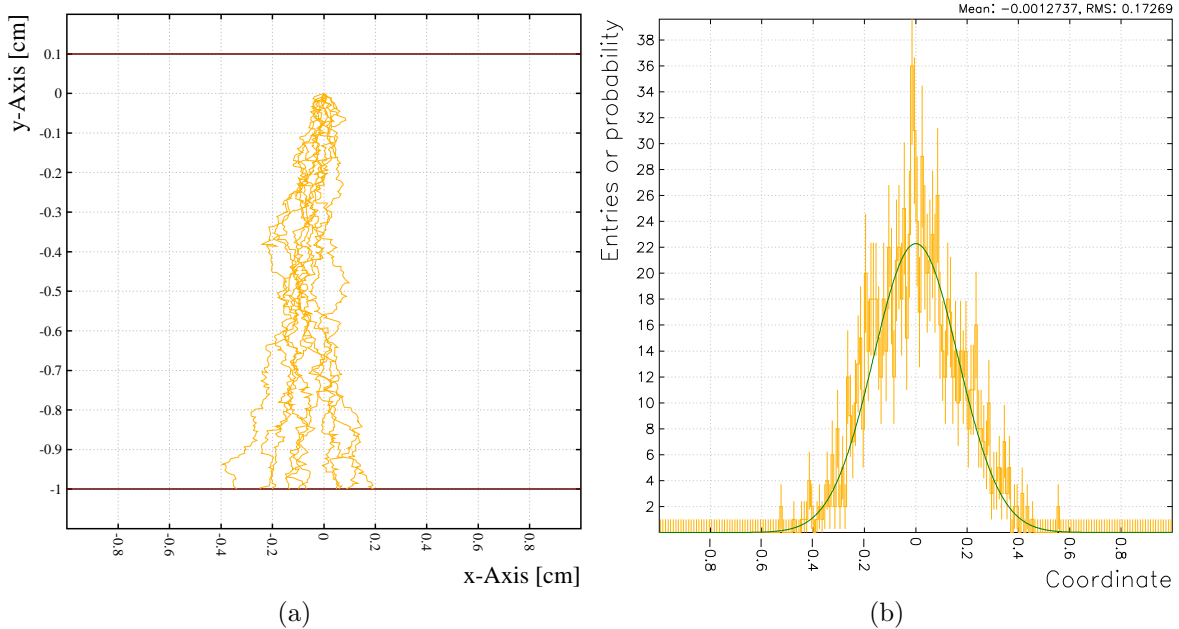


Figure 1.5: (a) Simulated 2D projection of the sinuous trajectories of 10 primary electrons starting at $(x, y, z) = (0, 0, 0)$. A nearly uniform electric field of 500 Vcm^{-1} along the y -axis is considered. The filling-gas is xenon at 293 K and 1 bar. (b) Spatial distribution projected into the x -axis, after 1 cm of drift at the same conditions as (a), of 1,000 primary electrons. The simulations were performed using Garfield 9.

region where the incoming particle deposited its energy. This type of recombination can be suppressed by applying a suitable and low electric field (usually with an intensity of a few hundred Vcm^{-1} for fast electrons and photons) which cause the ions and electrons to drift away from their formation point, in opposite directions. The volume recombination happens between electrons and ions of independent incoming particle hits since, specially for high rates, several tracks can be formed during the time that ions take to drift all the way towards the electrodes.

If the gas consists of a mixture containing an electronegative substance or if it contains impurities, there is the probability, in some collisions, of *attachment* of the drifting primary electron with a neutral atom or molecule. The resulting negative ion has similar properties as the ones created during the ionization process but drifts in the opposite direction due to its negative charge. Attachment, as recombination, also leads to the loss of the electron's contribution to the overall signal. When using noble gases, if their purity is carefully kept at high levels, attachment is unlikely and can be neglected.

1.2.2 Ionization Chamber

Ionization chambers are the simplest gaseous detectors since they directly collect the primary charge produced by incident particles, without additional amplification of its signal. They are often used as radiation dose measurement devices since they are able to measure irradiation rates. Figure 1.6 illustrates their operating principle. An electric field, below the excitation threshold of the gas, is created by applying an external voltage V inside a gas volume. Each incident particle creates a track of ion pairs. The motion of both electrons and ions, under the effect of the electric field, generates an electrical current which can be measured by an ammeter. If this volume is under steady-state irradiation and if the electric field is such that recombination is negligible, the electrical current is proportional to the radiation rate.

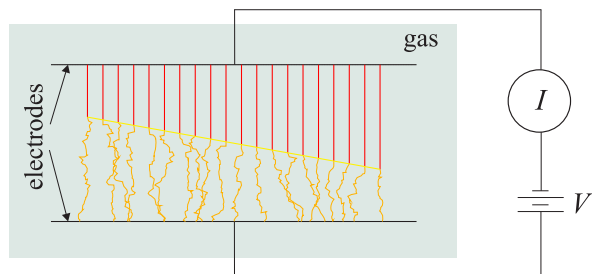


Figure 1.6: Operating principle of an ionization chamber. The yellow line represents schematically the trajectory of an hypothetical incident particle which creates ion pairs along its track. Red lines represent the trajectories of the ions that follow the field lines (a uniform field is considered in this scheme) and orange lines are the paths of the electrons, drifting sinuously in the opposite direction.

1.3 Detecting particles using amplification

When the number of primary charges produced by each incident particle is not sufficient to allow the generation of appropriate signals through its direct collection, signal amplification is needed. In the case of gaseous detectors, there are two different types of such process which are explained in the following sections: *Townsend avalanches* (charge amplification) and *electroluminescence* (light amplification).

1.3.1 Charge amplification

Under the effect of an electric field, the electrons are easily accelerated because of their reduced mass. If the applied electric field is sufficiently high, between collisions with gas atoms, the electrons can acquire energy above the ionization potential of the gas -

the field is thus above the *ionization threshold*. In this case, some of the collisions lead to ionizations of the gas producing additional negative charges - *secondary electrons*. These electrons, in turn, can also produce new ionizations as they are also under the influence of the same field. It is thus created a cascade charge multiplication, known as *Townsend avalanche*.

The fractional increase in the number of electrons, n , per unit path length, x , is described by the Townsend equation:

$$\frac{dn}{n} = \alpha dx, \quad (1.9)$$

where α is the *first Townsend coefficient* of the gas. This parameter is dependent on the strength of the electric field, being zero for values below the ionization threshold and usually increasing with the field above this value. From Equation (1.9) it results that, if the field is constant α is also constant, and the average number of electrons in the avalanche per primary electron – the *gas multiplication factor* or gain, M – increases exponentially with the distance:

$$\frac{n(x)}{N_e} = M = e^{\alpha x}. \quad (1.10)$$

If the intensity of the electric field is not constant, the gain is obtained through integration along the avalanche average path, Γ :

$$\ln M = \int_{\Gamma} \alpha(l) dl. \quad (1.11)$$

Each primary electron undergoes a process of multiplication ending up with a final number of charges, A , that fluctuates from avalanche to avalanche. The fluctuations are introduced by deviations of the electron trajectories relatively to the average path and by the fact that the energy acquired from the electric field is shared also with excitations. The relative variance of A is given by:

$$f = \left(\frac{\sigma_A}{\bar{A}} \right)^2. \quad (1.12)$$

The gain is the average multiplication factor from all the avalanches:

$$M = \frac{1}{N_e} \sum_{i=1}^{N_e} A_i = \bar{A}. \quad (1.13)$$

The relative variance in the detector pulse amplitude, Q , is due to the fluctuations

in the creation of primary electrons, as explained in Section 1.1.3, and to variations in the gain:

$$\left(\frac{\sigma_Q}{Q}\right)^2 = \left(\frac{\sigma_e}{\bar{N}_e}\right)^2 + \left(\frac{\sigma_M}{M}\right)^2 \quad (1.14)$$

Since each avalanche is independent of the others we can apply the error propagation obtaining:

$$\sigma_M^2 = \frac{1}{\bar{N}_e} \sigma_A^2 \quad (1.15)$$

and re-write Equation 1.14 as:

$$\left(\frac{\sigma_Q}{Q}\right)^2 = \left(\frac{\sigma_e}{\bar{N}_e}\right)^2 + \frac{1}{\bar{N}_e} \left(\frac{\sigma_A}{A}\right)^2 \Leftrightarrow \left(\frac{\sigma_Q}{Q}\right)^2 = \frac{F + f}{\bar{N}_e} \quad (1.16)$$

The parameter f describes the single-electron multiplication fluctuations and, under common operating conditions, is usually much larger than F (typical values between 0.2 and 0.6), being the critical parameter in the energy resolution optimization of detectors based in charge amplification. Geometries with higher gradients of the electric field, as Micro Pattern Gaseous Detectors, present lower avalanche fluctuations than others, as Proportional Counters [33].

1.3.1.1 Proportional Counter

The *Proportional Counter* (PC) is a type of gaseous detector introduced in the late 1940s and is used in low-energy X-ray spectroscopy and neutron detection [34].

Usually, its typical geometry consists of a grounded tube (cathode) with a thin wire (anode) passing at its axis, where a positive electrical potential, V , is applied. If a and b are the wire and tube radii, respectively, the electric field at a radial distance from the axis, r , is given by:

$$\|\vec{E}(r)\| = \frac{V}{r \ln\left(\frac{b}{a}\right)} \quad (1.17)$$

The previous dependency of the electric field intensity with the radial distance is schematically plotted in Figure 1.7a). An incoming particle interacts in the detector creating a set of primary electrons, whose number is proportional to the energy of the particle. These electrons drift towards the anode, in the *drift region*, under the effect of an increasing electric field lower than the ionization threshold of the gas. When a primary electron reaches the region where the field is higher than this threshold – the *multiplication region* –, the avalanche multiplication begins (see Figure 1.7b). In the

end, an electrical signal is produced resulting from the contribution of all produced secondary electrons.

The shape of the electric field in a proportional counter, given by Equation 1.17, allows the creation of a multiplication region confined to a very small volume when compared to the total volume of the detector. Therefore, most of the primary electrons are produced outside the multiplication region, undergoing the same multiplication gain on average, and generating an electrical signal with amplitude proportional to the number of primary electrons and thus, to the energy of the incoming particle.

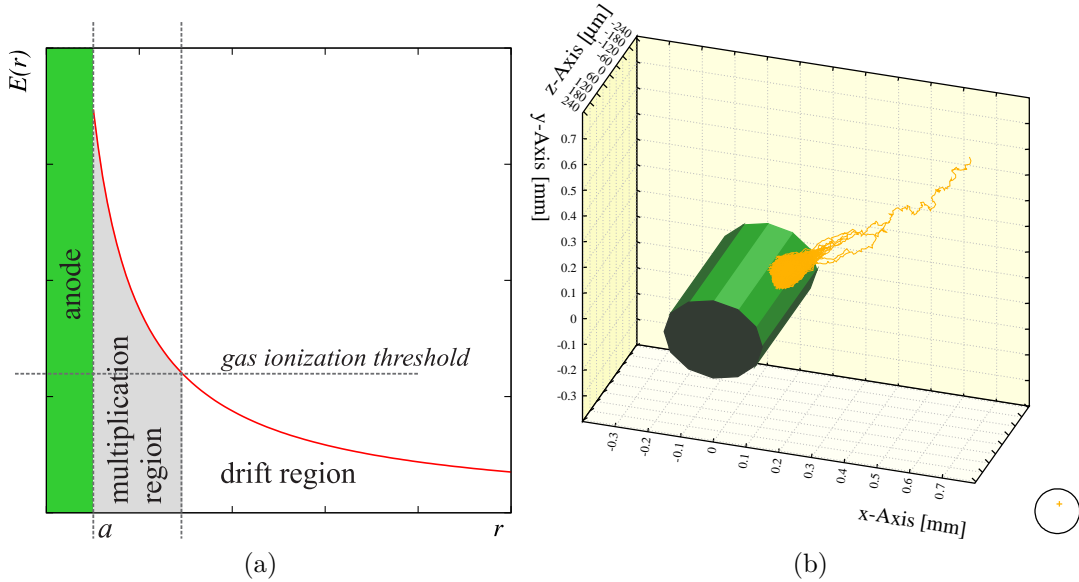


Figure 1.7: (a) Schematic dependence of the electric field in a Proportional Counter with the radial distance to the wire axis. Most primary electrons are formed in the drift region and drift toward the anode, entering in the multiplication region and undergoing an avalanche multiplication. (b) Development of a single-electron amplification near the anode wire. The simulation was performed using Garfield 9 considering xenon as the filling-gas at 293 K and 1 bar. The tube and wire radii were considered as 3 cm and 100 μm respectively.

1.3.1.2 Multiwire Proportional Chamber

The *Multiwire Proportional Counter* (MWPC) is based on the Proportional Counter and was introduced in 1968 by Georges Charpak [35], Nobel Prize laureate in 1992. It consists of a grid of thin wires between two large flat metal planes that run as cathodes. In Figure 1.8 the field lines and the equipotentials of such arrangement are shown. The primary electrons formed after interaction of the incoming particle drift under the effect of a nearly uniform drift field toward the plane of parallel wires. As each primary electron approaches the wire plane, the electric field increases and directs

it to one of the wires, where it undergoes an avalanche multiplication, similarly to what happens near the PC anode.

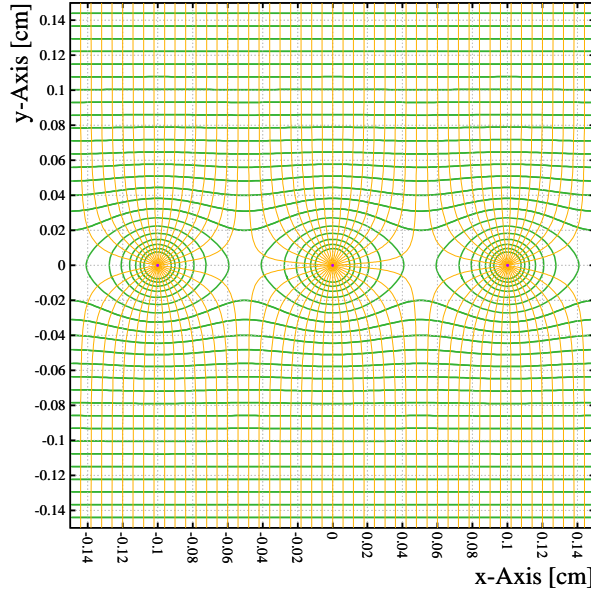


Figure 1.8: Field lines and equipotentials created in a Multiwire Proportional Counter. The device consists of a grid of thin wires between two large flat metal planes.

In the wire where the avalanche is collected a large induced signal appears, while in the neighboring wires a smaller signal is also induced. The position of a given point of the particle track can be measured by direct identification of the largest signal, corresponding to the closest wire, with a spatial resolution approximately equal to the wire spacing (typically between 1 and 2 mm). Resolutions better than the wire spacing can be achieved if the centroid is determined using also the signals from the neighboring wires. The wires can also be interconnected with resistors and, using center of charge algorithms, it is also possible to achieve spatial resolutions better than the wire spacing.

As signals, although less intense and of opposite polarity, are also induced in the cathodes, these can be fabricated as planes of strips, interconnect by resistors, and the same principle of charge division can be applied. The strips in one of the cathodes can be oriented orthogonally to the strips of the other, allowing simultaneous 2D spatial discrimination of the particle track.

Multiwire Proportional Chambers are, due to their economic construction and robustness, suitable for particle identification and tracking in High Energy experiments, easily covering large areas.

1.3.1.3 Time Projection Chamber

The first *Time Projection Chamber* (TPC) was proposed by David Nygren aiming full reconstruction of events of up to 20 particles resulting from electron-positron collisions in the PEP4 experiment [36, 37].

One of the main uses of this device is the reconstruction of trajectories of particles resulting from collisions in beam pipes. Usually the device consists of a cylinder with a long drift region. The particles resulting from the collisions leave a track of ionizations in their path. If the particle is charged, this track is curved by an external magnetic field and the radius of the trajectory gives information about its momentum. The electrons produced along the track, in the absorption / drift region, drift toward a multiplication and readout device with 2D spatial discrimination, usually placed at one or the two ends of the cylinder. The time that each primary electron takes to arrive to the readout system is a measurement of the third coordinate allowing 3D reconstruction of the track.

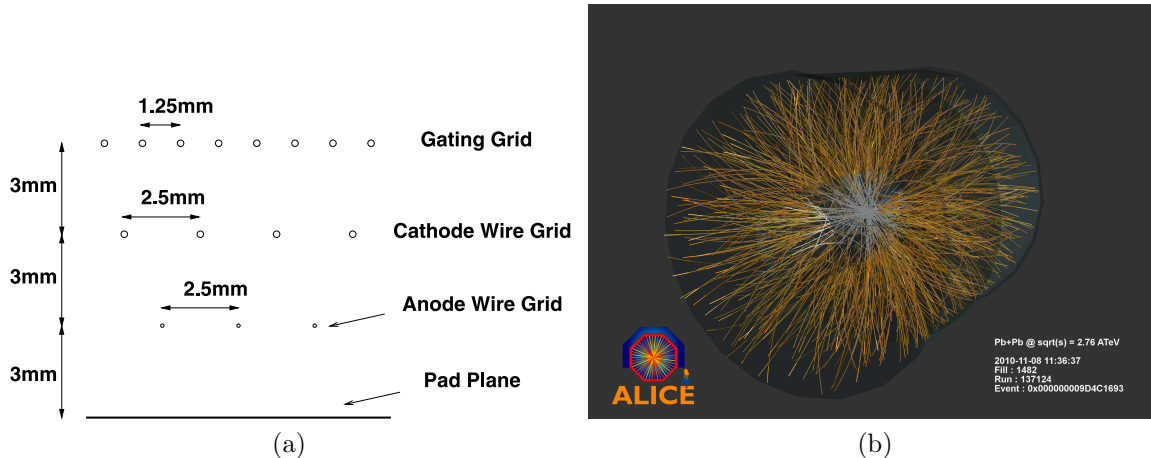


Figure 1.9: (a) Wire geometry of an ALICE TPC MWPC readout chamber [38]. All the wires are in the azimuthal direction. One of the metal planes of the standard MWPC is replaced by two layers of wires: the gating and the cathode grids. The other cathode is segmented in individual pads which provide 2D discrimination. (b) Reconstructed events of the first lead ions collisions at a centre-of-mass energy of 2.76 TeV per nucleon pair, recorded by ALICE in last November 8th 2010 [39]. Each collision produces thousands of tracks.

The typical readout system, as used e. g. in the ALICE TPC [38], part of the LHC machine [40], is made of individual modular MWPC chambers with azimuthal wires. One of the large metal planes of the standard MWPC is replaced by two layers of wires: the gating and the cathode grids (see Figure 1.9a)). If all the gating grid wires have the same potential, electrons from the drift volume enter the amplification

region. To reduce the charge deposit on the anode wires during background events, in the absence of a valid trigger, the gating grid is biased with a dipolar field, which prevents electrons from entering the amplification region. The other large metal plane is segmented into individual pads which provide polar position discrimination of the tracks (r and φ) through acquisition of the induced signals in those electrodes. The specific energy loss (explained in Section 1.1.2), dE/dx , as a function of the energy (or momentum) is different for each type of particle and thus, the pulse height of the signal induced in each wire is used to measure this quantity which, together with the momentum information, allows the particle identification.

In this way, the TPC provides 3D track recognition, momentum measurement and particle identification in a compact device, nowadays with event reconstruction capability for events with up to thousands of particles by making use of high density electronics (the reconstruction of a lead-lead ion collision is shown in Figure 1.9b) as an example).

1.3.1.4 Micro-pattern Gaseous Detectors

The invention of the MWPC was an impressive breakthrough allowing to easily track particles, as seen in Section 1.3.1.2. However, due to the long distances that ions formed in the process of avalanche multiplication need to travel until being collected and to their low drift velocity, in high rate environments (higher than 10^3 Hz mm $^{-2}$), these devices have limitations. In these conditions, the ions are not drained at the same rate at which new ionizations are created and accumulate in the gas volume, distorting the electric field and decreasing the gain. This is the so-called *space-charge* effect. In addition, as MWPC is based on an *open geometry*, the photons emitted during the de-excitation of excited atoms that are produced during the avalanche process can induce new undesirable avalanches by removing electrons from the walls of the detector and / or from the metal electrodes – *photon feedback*.

The technologies on precision circuit board printing techniques, available in the 1980s, triggered the creation of the Micro-pattern Gaseous Detectors (MPGDs), with very small distances between electrodes (a few dozens of μm) when compared to the spacing between wires in the MWPC, avoiding the space-charge effect and thus allowing higher rate capability. The first introduced detector was the Micro Strip Chamber (MSG), still an open geometry structure, but soon other *close geometry* structures appeared with reduced photon feedback effects, such as the Gas Electron Multiplier (GEM) or the more recent Micro-Hole & Strip Plate (MHSP), among others.

Nowadays, MPGDs are characterized by very good spatial resolution, fair energy resolution, high rate capability, operational stability and radiation hardness. It is

also possible to cover large sensitive areas. Due to these features, MPGDs are used in several particle, nuclear and astro-particle physics experiments. There is also a very strong interest on the R&D of these devices, carried out by the “CERN - RD51 collaboration” that involves 73 institutes from 25 countries, including the DRIM group, from University of Aveiro.

Micro-Strip Plate

The *Micro-Strip Plate* (MSP) was the first MPGD to be created and was introduced by Anton Oed [41] in 1988. It consists of a series of small metal strips (anodes and cathodes placed alternately in the same plane) supported by an insulator substrate. The anodes are constructed to be thin while cathodes are wider. As an example, the original MSP had a pitch of $200 \mu\text{m}$, with anode and cathode widths of 10 and $100 \mu\text{m}$, respectively, being their centers separated by $100 \mu\text{m}$. A schematic view of the MSP structure is shown in Figure 1.10. When a suitable voltage (much lower than those needed in MWPCs) is applied between anodes and cathodes, the electrons, arriving from the drift region, are focused toward the anodes, around which a strong electric field is created, and undergo multiplication. A gas-filled detector working with a MSP is commonly called *Micro-Strip Gas Chamber* (MSGC).

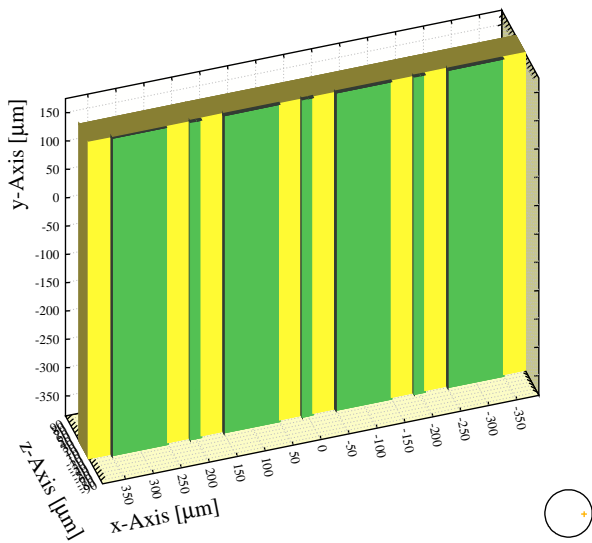


Figure 1.10: Schematic 3D view of the MSP structure. The device consists of a series of anodes and cathodes placed alternately on the top of an insulator plane. Anodes are thin while cathodes are wider.

The difference in the amplitudes or in the time of arrival of the signals induced in the strips can be used to discriminate one of the coordinates. This can be done by reading the signal from each strip independently or interconnecting them by resistive

lines and applying center of mass algorithms to the signals arriving at both ends of the lines. To determine the second coordinate, strips can be etched on the opposite side of the substrate, perpendicularly to the anode strips, and the same principle can be applied.

Energy resolutions of about 18 % for X-rays of 6 keV have been achieved for rates of up to 100 kHz mm⁻² using MSPs [42]. Spatial resolution of about 70 μm (FWHM) was obtained for minimum ionizing particles with momentum of 9 GeV/c [43]. More recently, spatial resolutions between 0.1 and 0.6 mm (FWHM) for gains between 8000 and 40000 and rates of up to 400 kHz mm⁻² were reported [44].

Gas Electron Multiplier

The *Gas Electron Multiplier* (GEM) was invented by Fabio Sauli in 1996 [45], initially as a pre-amplification stage to allow other devices, as MWPCs, to operate with larger gains and / or in less critical conditions, specially at high rates. The device consists of a thin Kapton® foil of typically 50 μm thick. The foil is covered on both sides with 5 μm thick layers of copper and etched with an hexagonal pattern (with 140 μm long edges) of bi-conical holes. A simulated view of the GEM is presented in Figure 1.11. Applying a suitable potential between the upper and the lower electrodes of the structure, it is possible to create a very high electric field inside the holes. Electrons traveling from the drift region are focused inside the holes and undergo a multiplication process, under the effect of the strong field that exists there. The photon feedback effect is reduced in this structure since almost all of the excitations and ionizations happen in the lower half part of the structure and most of the photons, emitted during the avalanche development, are blocked by the structure itself.

With the developments made over the time, GEM developed into a detector by itself, no longer being just a stage of pre-amplification. Cascading several GEMs, it is possible to reach high gains (up 10^6 for triple GEM) without discharges. Energy resolutions around 20 % (FWHM), achieved at rates of up to 1 MHz mm⁻², are generally sufficient for most applications [46]. By placing a charge pick-up electrode bellow the last amplification stage it is possible to add position discrimination to a GEM detector. Using thin multi-layer boards, made of thin polymer foils with pads or strips interconnected in various patterns, it is possible to achieve FWHM 2D position resolutions of about 40 μm [47]. It is also possible to fabricate large area structures (up to 1,000 cm²) as the triple GEMs used in the Common Muon Proton Apparatus for Structure and Spectroscopy (COMPASS) [48] and in the Total Elastic and Diffractive Cross Section Measurement (TOTEM) [49] tracking detectors, both at the LHC. Recently, GEMs with different shapes, namely cylindrical [50] and spherical [51], have

been constructed.

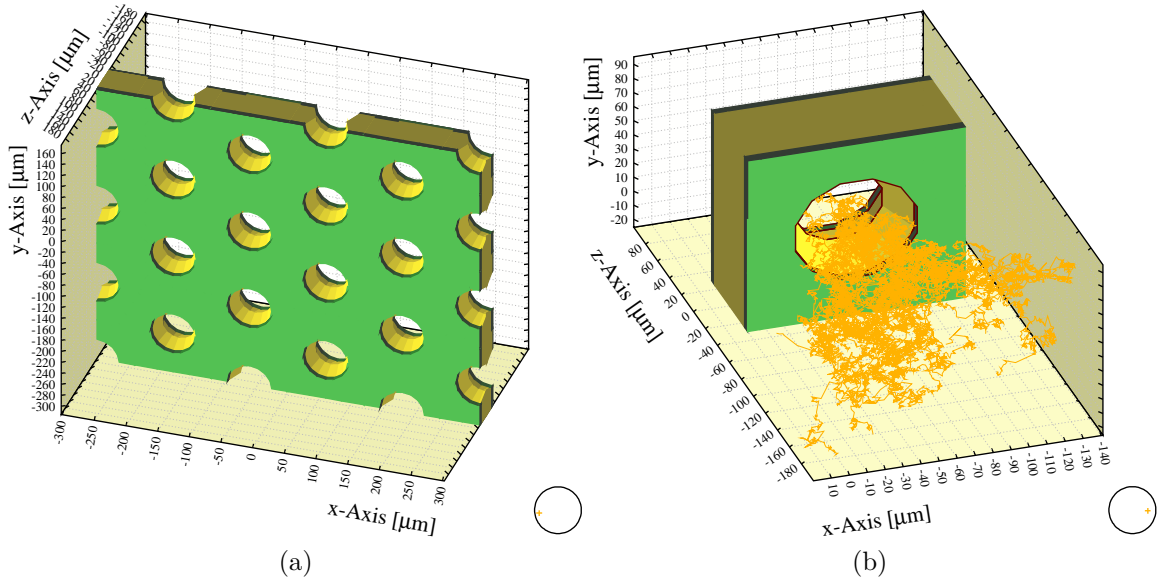


Figure 1.11: Simulated 3D views of a GEM: (a) hexagonal pattern of the holes. (b) Detail of an avalanche undergone by one primary electron. The simulation was performed using Garfield 9 considering xenon at 293 K and 1 bar as the filling-gas. The drift and induction fields were both of 0.5 kVcm^{-1} .

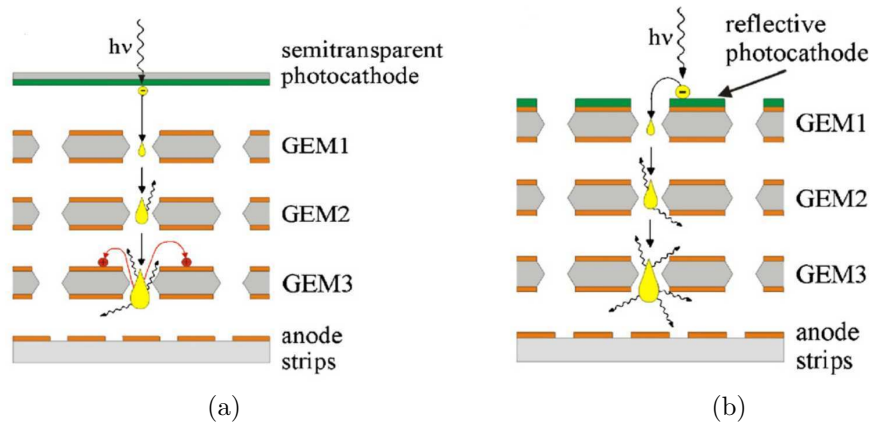


Figure 1.12: Schematics of GPMs constructed using triple GEMs with: (a) semitransparent and (b) reflective photocathodes. Images retrieved from reference [52].

In addition, the GEM mirostructure can be used to construct Gaseous Photomultipliers (GPMs), with sensitivity in the VUV range and aiming applications in Ring Imaging Cherenkov (RICH) detectors [53, 54, 55]. If a quartz window is used and a CsI layer deposited on it (that runs as semi-transparent photocathode), incident VUV photons will extract photoelectrons from the photocathode, which will undergo the

common avalanche multiplication along the GEM stages (see Figure 1.12a)). It is also possible to deposit the CsI layer directly on the top of the first GEM (in this case the photocathode is reflective). The amplification of the photoelectrons is similar to the previous case (see Figure 1.12b)).

Micro-Hole & Strip Plate

The high gains that can be achieved with GEMs, mentioned in the previous section, imply the use of cascades of structures, since a single GEM has a modest performance in terms of gain (~ 300) before electrical breakdown. In this sequence, J. F. C. A. Veloso developed the *Micro-Hole & Strip Plate* (MHSP) in 2000 [56]. It is made of a $50\ \mu\text{m}$ thick Kapton[®] foil, copper-clad on both sides. A GEM pattern is etched on one side, and a MSP pattern on the opposite side, with the holes emerging in the cathode strips. In this way, the MHSP is an hybrid structure that combines, in a single device, the features of the GEM and of the MSP. Figure 1.13 shows the arrangement of the MHSP electrodes and holes. Applying suitable potentials on each of the electrodes, a strong electric field is created inside the holes, but also near the thin anodes of the MSP side. Electrons coming from the drift region are focused inside the holes, where an initial avalanche occurs. When the electrons emerge on the MSP side they are directed toward the anode strips, where they undergo a second charge multiplication. Thus, the MHSP is a device with two charge multiplication stages and has achieved charge gains higher than those of a single GEM (above 10^4), with energy resolutions of 14 % for X-rays of 5.9 keV [57]. Due to the MHSP geometry, a substantial fraction of the ions created in the avalanches can be trapped on the cathode strips [58], reducing space-charge effects in high rate applications . In fact, it has worked at rates of $500\ \text{kHz mm}^{-2}$ with gain variations below 5 % [59]. Another advantage of this device is that it combines in one single structure the amplification and readout systems.

The good performance of the MHSP in terms of charge gain and energy resolution make it suitable for single photon counting X-Ray imaging. In order to provide 2D position discrimination, the device can be slightly modified. If the anode strips (in the MSP side) are interconnected with a resistive strip and the signals from both sides of it are collect, it is possible, by center of mass algorithms, to determine one of the coordinates. The GEM side can be segmented in *zig-zag* strips, perpendicular to the anode strips and aligned with the holes of the structure. By interconnecting these strips with a resistive line and applying the same principle, it is possible to discriminate the other coordinate. This device, with 2D spatial discrimination, has been successfully used in radiography achieving FWHM resolutions of 300 and $600\ \mu\text{m}$ in the x and y directions, respectively [60]. It has been used also in Computed Tomography (CT)

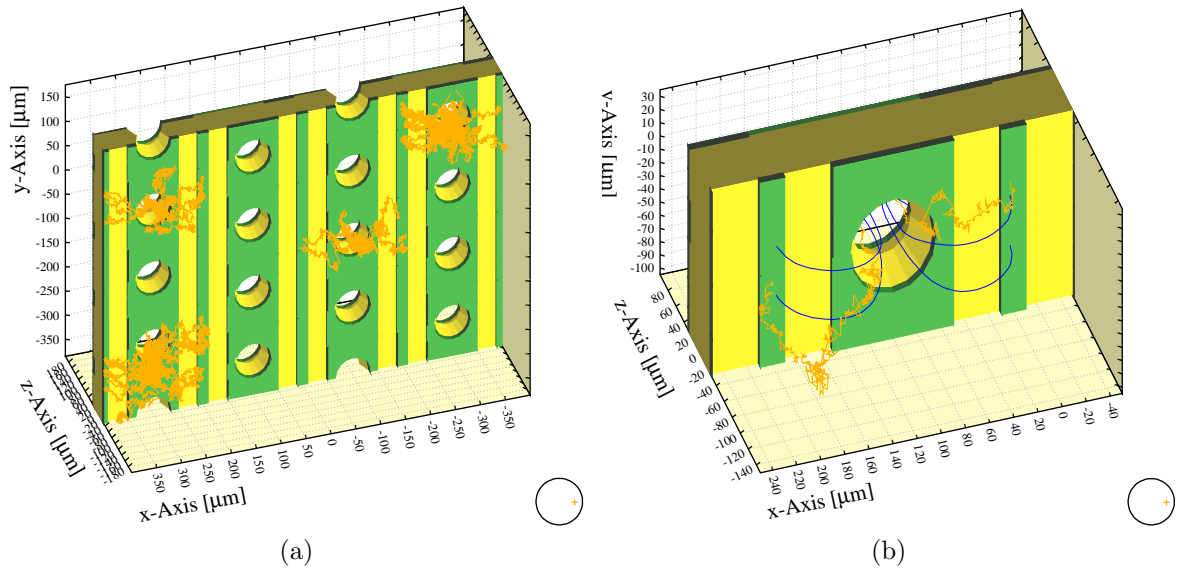


Figure 1.13: Simulated 3D views of a MHSP: (a) hole pattern following the cathode strips and avalanches initiated by some primary electrons coming from the drift region (behind the microstructure). (b) Average drift lines of electrons (in blue) together with the sinuous trajectories of two primary electrons (in orange) – the trajectories of secondary electrons are not represented. In both cases, the simulation was performed using Garfield 9 considering xenon as the filling-gas at 293 K and 1 bar. The drift and induction fields were considered as 0.1 kVcm^{-1} .

having the capability of correcting the intensity distribution of the acquired images, affected by distortions due to the X-ray transmittance difference of adjacent materials, using the energy information – *Energy Weighting Technique* [61, 62].

1.3.2 Electroluminescence amplification

As discussed in the previous Section, the charge amplification is implemented by applying electric fields that are above the ionization threshold, in order to provide electrons with an energy higher than the ionization potential of the gas and produce secondary charges. Another type of amplification – *electroluminescence amplification* – can be used if the field is such that electrons acquire, between collisions, enough energy to excite atoms of the gas but not to ionize them. In the de-excitation process of the atoms, light in the range from VUV to Vis-IR is emitted, as explained in Chapter 2. This light can be detected with suitable readout systems.

This method allows to achieve, in principle, unlimited gains, by extending the amplification region indefinitely. The number of emitted photons per primary electron and per unit path length is defined as the *electroluminescence yield*, Y . This pa-

rameter increases linearly with the electric field for fields between the excitation and the ionization thresholds – the *proportional region*. Above the latter, the behavior is usually exponential reflecting the light produced also by the secondary electrons that meanwhile are created through avalanche multiplication.

Electrons traversing an EL region produce a given average number of photons, \bar{N}_{EL} . However, each electron produces a number of photons slightly different from the others. These statistical fluctuations are introduced by the random nature of the electron drift and decrease as the electric field is increased within the proportional region range, at the same time that the fraction of energy supplied by the electric field that is spent in excitations increases up to more than 80 % in noble gases. To describe the fluctuations in EL it is used the parameter J , similar to the Fano factor F (see Section 1.1.3), that is the ratio between the variance in the number of emitted photons per primary electron, σ_{EL}^2 , and the variance if the process was described by the Poisson model, \bar{N}_{EL} :

$$J = \frac{\sigma_{\text{EL}}^2}{\bar{N}_{\text{EL}}} \quad (1.18)$$

In some documents, this parameter has also been referred as J_{CP} , in honor to the pioneering contributions of C. A. N. Conde and A. J. P. Policarpo, from University of Coimbra, to the development of EL as a technique.

The intrinsic relative variance associated with the detection of radiation using EL of a given gas is thus due to the fluctuations in the primary charge formation and to variations in the number of photons produced per primary electron:

$$\left(\frac{\sigma_Q}{Q}\right)^2 = \left(\frac{\sigma_e}{\bar{N}_e}\right)^2 + \frac{1}{\bar{N}_e} \left(\frac{\sigma_{\text{EL}}}{\bar{N}_{\text{EL}}}\right)^2 = \frac{1}{\bar{N}_e} \left(F + \frac{J}{\bar{N}_{\text{EL}}}\right) \quad (1.19)$$

For the field ranges used in proportional electroluminescence the only process competing with excitations is the elastic scattering which introduces a very slight variation in the electron energy in each collision. Thus J is usually much lower than F and f , the latter being the parameter that characterizes the fluctuations in avalanche multiplications (defined in Equation 1.12). This is the reason why EL based detectors achieve high performances in terms of energy resolution. Note that to obtain the energy resolution of an EL based detector, one needs to sum in quadrature the intrinsic relative variance defined in Equation 1.19 with the relative variances related to the photon detection, a topic discussed in Section 1.4.

1.3.2.1 Gas Scintillation Proportional Counter

The *Gas Scintillation Proportional Counter* (GSPC) is an EL based detector introduced by C. A. N. Conde and A. J. P. L. Policarpo in 1964 [63]. GSPCs usually

work with pure noble gases and make use only of the VUV light emitted during the de-excitation of atoms of the gas, since its intensity is about one order of magnitude higher than that of Vis-IR light. This device is used mainly for X-ray spectrometry, for energies up to 100 keV [64], in astronomy, medical instrumentation and High Energy Physics combining good energy resolution with large areas, high rate capability and reduced space charge effects, when compared to proportional counters. A GSPC consists of a drift region, where the incident X-ray interacts and produces the primary charge, which is directed to the electroluminescence region (sometimes also called scintillation region), where the primary electrons are accelerated, exciting atoms that consequently emit light. Over time, different GSPC shapes were considered, namely cylindrical (devices similar to proportional counters but working with lower potentials) and spherical. However the most used type of GSPC works with a nearly uniform electric field created by parallel meshes. In Figure 1.14 is shown the components and the principle of operation of a GSPC implementing a parallel field geometry.

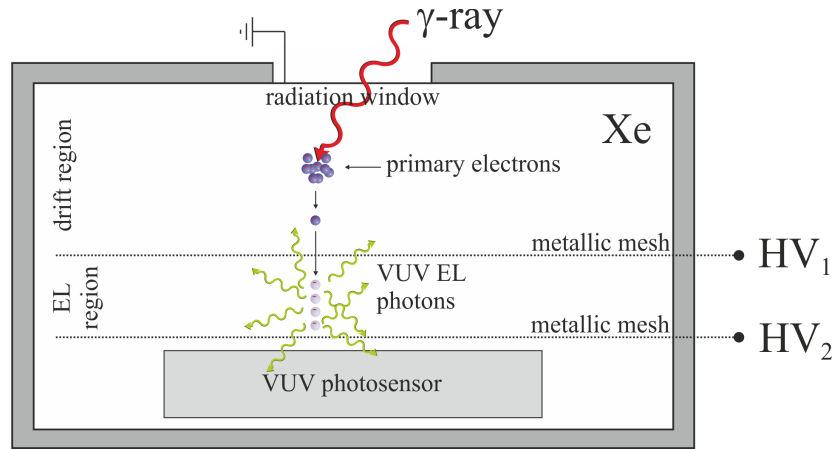


Figure 1.14: Schematics and operating principle of a GSPC. The primary electrons are produced by the incident γ -ray in the drift region and drift toward the EL region, where are accelerated and produce EL light.

The VUV photons can be detected by special VUV-sensitive Photomultiplier Tubes (PMTs) [65] or by standard tubes after a wavelength shifting to the visible range, using organic materials. Photodiodes can also be used for light readout, namely the recent Large Area Avalanche Photodiodes (LAAPDs) [66]. Since they can directly detect both VUV and X-ray photons, LAAPDs allow a quantification of the absolute number of VUV-photons produced per primary electron – the *total electroluminescence yield* – given the quantum efficiency of the device and its implicit solid angle. Recent works have measured absolute electroluminescence yields of pure argon and xenon, both in uniform and non-uniform fields, using these devices, by comparing the pulse amplitude of the full absorption of monochromatic X-rays in the gas with that of direct interaction

in the LAAPD [67, 68, 69]. Since the number of primary electrons is proportional to the energy of the incident X-ray and each primary electron produces, on average, the same number of VUV photons, the signal collected by the photon detection system is also proportional to the energy of the X-ray. FWHM energy resolutions of 8 % and 4 % have been reported for 5.9 keV and 22 keV X-rays, respectively, obtained by GSPCs working with xenon [70]. The energy resolution performances are the main figure of merit of these devices.

1.3.2.2 Scintillation Drift Chamber

The *Scintillation Drift Chamber* (SDC) was invented in 1978 [71]. Like in a TPC, the device measures one of the coordinates of the particle track points using the time that primary electrons take to arrive to the readout plane. In the case of a SDC, the detection of the electrons, instead of being through charge multiplication, is made by collection of the EL light produced in a region where the electric field is between the excitation and the ionization thresholds. A SDC working with a uniform field created by two parallel meshes and constructed with 19 PMTs has achieved resolutions of 3.6 % in energy, 3.7 mm in (x, y) and 0.6 mm in z for 59.6 keV X-rays, using high pressure pure xenon (9 bar) [72]. A modern large SDC is being developed by the NEXT collaboration, to search for the neutrino-less double beta decay ($\beta\beta^{0\nu}$) in ${}^{136}\text{Xe}$ (described in Chapter 7). The choice of a SDC is related to the very high energy resolution that can be achieved using EL, of major importance in $\beta\beta^{0\nu}$ searches.

Noble gas dual phase liquid / gas SDCs have been used for direct detection of Weakly Interacting Massive Particles (WIMPs), the leading theoretical Dark Matter candidates [1, 2, 3, 4]. These particles, in principle, interact with the nuclei in the dense liquid phase producing both primary scintillation and ionization. The electrons produced at this stage are driven to the gaseous phase where EL amplification produces a second light signal. The ratio between the two light signals (one from primary scintillation and the other from EL) allows to separate the WIMP signal from background since it is a unique signature of each elementary particle.

1.3.3 Hybrid concepts

In some applications it might be interesting to combine the light amplification with charge amplification or to use the EL light produced in avalanches, in order to obtain better performances in specific applications. In this case, we are facing a new type of detectors: the *hybrid detectors*. In this section, three devices of such type are presented: the first two use MPGDs coated with CsI as VUV photosensors to detect

the EL produced in GSPCs (instead of the traditional PMTs); in the third the EL light is used as intermediate process for de-coupling charge amplification stages in order to reduce the ion backflow, extremely important for GPMs aiming sensitivity in the visible range and TPCs working at high rate environments.

1.3.3.1 GSPC/MSGC hybrid detector

The photosensors commonly used for detecting the VUV EL light in GSPCs, the PMTs, are limited to small areas. In order to increase the detection area, usually several PMTs are arranged in a plane of detection. This type of arrangement involves an increase in the difficulty of the detector construction as well as an increased complexity and cost of the electronics needed to read and correlate electric signals. Also, sometimes it is necessary to increase the gas-filling pressure in order to increase the detection efficiency, which implies the use of thick quartz scintillation windows that absorb much of the light to be detected. To overcome these limitations, in 1996, J. F. C. A. Veloso has proposed a xenon-GSPC/MSGC hybrid detector [64]. The arrangement and the principle of operation of the detector is schematically represented in Figure 1.15.

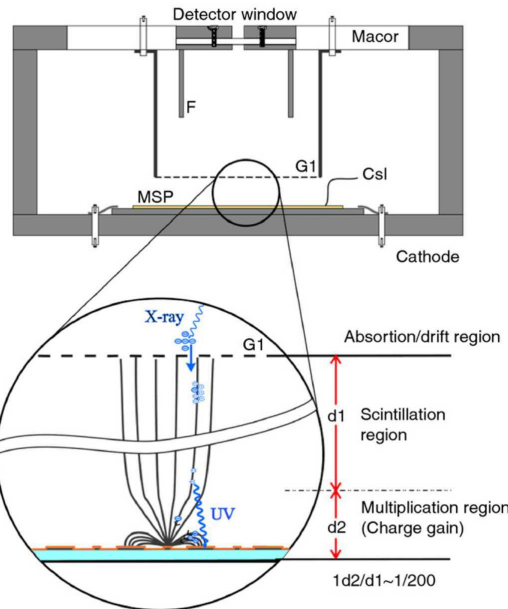


Figure 1.15: Schematic and principle of operation of the xenon-GSPC/MSGC hybrid detector proposed in reference [64].

The detector consists of a common GSPC with an absorption region where the external radiation produces primary electrons. These are driven, under the effect of a drift field that avoids recombination, toward a first grid G1. Below the grid G1 a MSP structure is placed. Both are polarized in such a way that an EL region with a

nearly uniform electric field is created in most of the volume between G1 and the MSP. In the vicinity of the MSP, it is created a confined charge multiplication region. A CsI photocathode is deposited on the top of the MSP. A fraction of the VUV photons emitted in the EL region impinges the photocathode and, with a given probability, extracts photoelectrons from it. These undergo avalanche multiplication, characteristic of a MSP, around and near the thin anode strips that collect the resulting negative charges.

This detector can be a good alternative to the use of PMTs and other photosensors when compactness, large detection areas, low cost and low power consumption are key features. It can also be useful when insensitivity to magnetic fields is needed, an application where usually PMTs are useless. Energy resolutions of 5.5 % and 3.4 % for 22 keV and 60 keV X-ray photons, respectively, were achieved with this detector using xenon at 2 bar [73], which represents only a slight deterioration relatively to the common GSPCs instrumented with PMTs.

1.3.3.2 2D-MHSP GSPC gamma camera

Gamma cameras are detectors used for nuclear medical γ -ray imaging. Solid scintillators are usually used in these applications due to their high photon detection efficiency. However they are characterized by poor energy resolution and by spatial resolutions not better than 4 mm. Thus, there is a demand for the development of alternative detectors with better performances.

Gaseous detectors represent an alternative to the solid state detectors, although their detection efficiency is in general low for high energy γ -photons. A way to increase this efficiency is to increase the gas-filling pressure. This represents, in charge multiplication based detectors, a decrease in the achievable gain since higher voltages are needed and consequently the probability of sparks increases, resulting in a degradation of the position resolution. The EL amplification is thus the natural option, although the use of PMTs or LAAPDs for the light readout would also imply a poor spatial resolution besides a high cost in the detector construction. In this context, and due to their intrinsic high spatial resolution capability and to the possibility of being used as photosensors, MPGDs play a role.

In Figure 1.16 it is represented an hybrid gamma camera constructed by making use of a MHSP with 2D spatial discrimination capability (2D-MHSP) [74]. Three metal meshes are placed above the 2D-MHSP and polarized in such a way that an absorption region, an EL region and a photoelectron drift region are created. The external γ -rays interact in the absorption region, preferentially by photoelectric absorption producing a cloud of primary electrons. These drift toward the second mesh from which a

EL electric uniform field exists. The primary electrons produce, between the second and the third meshes, VUV EL photons which are emitted isotropically. A fraction of them impinges on a CsI photocathode, deposited on the top of the 2D-MHSP, extracting photoelectrons from it, which are focused into the holes, undergoing avalanche multiplication typical of a MHSP. This detector is hybrid since the EL is used as an intermediate amplification process, happening before an avalanche multiplication which can now be made smaller. With this detector, spatial resolutions of 1.2 mm for a xenon-filling pressure of 2.9 bar were achieved using 59.6 keV γ -photons [74].

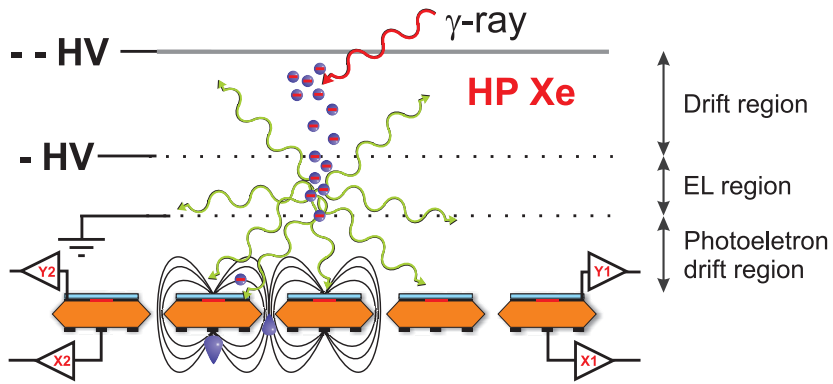


Figure 1.16: Schematic and principle of operation of a gamma camera constructed with a 2D-MHSP coated with a CsI photocathode. Image extracted from [74].

1.3.3.3 PACEM

As mentioned previously, positive ions produced in electron avalanches can cause secondary effects, limiting the performance of detectors. In e.g., TPCs working at high rate environments, ions flowing back to the drift region accumulate in the volume modifying the electric field and causing track recognition distortions. Furthermore, e.g., in GPMs, the backflow of ions toward the photocathode cause its physical and chemical ageing as well as the possible start of new undesirable secondary avalanches by removing new photoelectrons from the photocathode. This causes gain limitations and position resolution deterioration. Thus, the reduction of the *ion backflow* (IBF) is of major importance in such applications.

Recently, in 2006, J. F. C. A. Veloso has proposed the *Photon-Assisted Cascaded Electron Multiplier* (PACEM) as a concept for IBF suppression [75]. The schematics of the PACEM concept is presented in Figure 1.17. Photoelectrons produced in a reflective photocathode of a GPM or primary electrons created along a particle track interacting in the absorption / drift region of a TPC, are focused into the MHSP holes and undergo avalanche multiplication both inside the hole and near the anode strips. The VUV photons produced in the avalanche are used for signal amplification and transmission

to the next cascade element, which is coated with a thin layer of CsI in order to convert the VUV light into photoelectrons. The last undergo the normal avalanche multiplication typical of MPGDs. The ions created in the avalanches developed in the MHSP are collected by its cathodes and by a grid, placed between the MHSP and the second cascade element and under the effect of a suitable potential. In this way, and using optimal voltage configurations, only about 20 % of the ions originating in the first stage drift back through the MHSP holes. In addition, the presence of the grid ensures that, regardless of the total gain of the cascaded multiplier, only ions produced in the first stage flow back to the drift region.

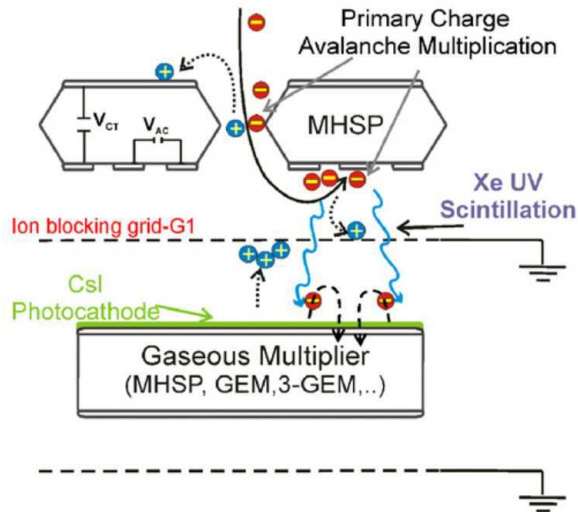


Figure 1.17: Schematic and principle of operation of the PACEM concept. Image retrieved from [76].

This concept, which consists in the *opto-coupling* between two charge multiplication systems, can be implemented in many configurations of cascaded multipliers, although the choice of the MHSP as the first stage shows advantages due to its intrinsic IBF reduction capability. The IBF is defined as being the fraction of ions reaching the drift region in the case of a TPC (or the photocathode in the case of a GPM), relative to the total number of electrons collected in the readout anode. Using a MHSP - GEM configuration working with pure xenon, IBFs of around 10^{-4} for gains of 10^4 and 10^{-5} for gains of 10^6 have been achieved [76], which are suitable values for applications in TPCs.

1.4 Energy Resolution

The relative variance of a gaseous detector pulse amplitude, $\left(\frac{\sigma_Q}{Q}\right)^2$, can be obtained by summing in quadrature the contributions of all processes happening until the signal (in charge or light according to the used method) is collected. This sum can be done because we can consider each of the processes independent from the others. Once the pulse amplitude relative variance is determined, or equivalently the relative standard deviation $\left(\frac{\sigma_Q}{Q}\right)$, it is possible to calculate the Full-Width-at-Half-Maximum (FWHM) energy resolution achieved by a given detector:

$$R_E = 2\sqrt{2 \ln 2} \left(\frac{\sigma_Q}{Q} \right) \simeq 2.35 \left(\frac{\sigma_Q}{Q} \right) \quad (1.20)$$

In the previous expression the factor $2\sqrt{2 \ln 2}$ corresponds to the relation between the FWHM and the standard deviation, σ , of a given probability distribution ($\text{FWHM} = 2\sqrt{2 \ln 2}\sigma \simeq 2.35\sigma$).

For instance, in an ionization chamber, the only contribution comes from the statistical fluctuations in the number of primary electrons created by the incident particle:

$$R_E = 2.35 \sqrt{\left(\frac{\sigma_e}{N_e} \right)^2} \quad (1.21)$$

This is the intrinsic FWHM energy resolution of a given gas, and is established by the Fano factor, the W -value and the energy deposited in the gas by the particle, E , (see Equations 1.5 and 1.6):

$$R_E = 2.35 \sqrt{\frac{W}{E} F} \quad (1.22)$$

In a proportional counter or in a gaseous detector based in charge amplification, the fluctuations in the avalanche multiplication, described by the parameter f (Equation 1.12) should be added (see Equation 1.16) [77]:

$$R_E = 2.35 \sqrt{\frac{W}{E} (F + f)} \quad (1.23)$$

As seen in Section 1.3.1, under typical conditions of operation, f is much larger than than F and thus the energy resolution of gaseous detectors using charge multiplication is dominated by the fluctuations in the single-electron multiplication.

In the case of an EL based detector, like a GSPC or a SDC, the contributions of the fluctuations due to the photon detection system should be added to the intrinsic EL pulse amplitude fluctuations in the gas (defined in Equation 1.19). In many cases,

and in those analyzed in this work, the photons are detected by a PMT and thus the fluctuations in the number of photoelectrons extracted to the PMT photocathode per incoming particle, \overline{N}_{pe} , and in the PMT's single electron pulse height, \overline{G}_q , are those to be considered:

$$R_E = 2.35 \sqrt{\left(\frac{\sigma_e}{\overline{N}_e}\right)^2 + \frac{1}{\overline{N}_e} \left(\frac{\sigma_{\text{EL}}}{\overline{N}_{\text{EL}}}\right)^2 + \left(\frac{\sigma_{\text{pe}}}{\overline{N}_{\text{pe}}}\right)^2 + \frac{1}{\overline{N}_{\text{pe}}} \left(\frac{\sigma_q}{\overline{G}_q}\right)^2} \quad (1.24)$$

The conversion of VUV photons into photoelectrons follows a Poisson distribution and thus $\sigma_{\text{pe}}^2 = \overline{N}_{\text{pe}}$. The fluctuations in the photoelectron multiplication gain within the PMT can typically be described by an exponential distribution and thus $\left(\frac{\sigma_q}{\overline{G}_q}\right)^2 = 1$ [78]. The average number of photoelectrons extracted to the PMT per incoming particle, \overline{N}_{pe} , can be obtained as:

$$\overline{N}_{\text{pe}} = k \overline{N}_e \overline{N}_{\text{EL}} \quad (1.25)$$

where k is the fraction of EL photons produced per incoming particle that gives rise to the production of a photoelectron and depends on the implicit solid angle and on the quantum efficiency of the photocathode. Taking into account the relations (1.5), (1.6), (1.18) and (1.25), Equation (1.24) can be rewritten as follows [70]:

$$R_E = 2.35 \sqrt{\frac{W}{E} \left(F + \frac{1}{\overline{N}_{\text{EL}}} \left(J + \frac{2}{k} \right) \right)} \quad (1.26)$$

Usually J is much smaller than F and, in addition, it is divided by the average number of EL photons produced per primary electron, before summing with it. Thus, the energy resolution of an EL detector is attributed only to the fluctuations in the primary charge production and in the photon detection system (in this work PMT's are considered):

$$R_E \simeq 2.35 \sqrt{\frac{W}{E} \left(F + \frac{2}{k \overline{N}_{\text{EL}}} \right)} \quad (1.27)$$

The second term in Equation (1.26) can easily be made smaller than f by using several PMTs in order to increase the geometric detection coverage or by increasing the light gain, \overline{N}_{EL} . This is the reason why EL based detectors achieve much better performance, in terms of energy resolution, than those based in avalanche charge amplification. Measuring the energy resolution of an EL detector and extrapolating this quantity to infinite light gain, it is possible to determine the Fano factor of a gas, given the W -value.

CHAPTER 2

Electroluminescence process

The process of electroluminescence in pure noble gases is related to the atomic energy structure. The drifting electrons collide with gas atoms and transfer energy to them in the form of motion, excitations or ionizations. In the last two cases the excited atoms or ions, respectively, undergo various physical processes that result ultimately in the emission of photons in the VUV to IR range.

2.1 Atomic energy structure of noble gases

The valence electrons of an atom of neon, argon, krypton or xenon in the ground state have the shell configuration np^6 . The excited states are produced by the transition of one of these electrons into more energetic orbitals (n' s, n' p, n' d, ...). The excited electron stays, in average, at a great distance from the atomic core (np^5). The spin-orbit interaction of the electrons of the atomic core is thus greater than the electrostatic interaction of them with the excited electron and the so-called jl coupling scheme should be considered [79].

A state is described by the quantum numbers (n', j, K, J) , where n' is the principal quantum number of the excited electron, j is the total angular momentum of the atomic core (the result of the spin-orbit coupling of the core), K represents the coupling of the total angular momentum of the atomic core with the orbital angular momentum of the excited electron, l , and $J = K \pm 1/2$ is the total momentum of the atom that takes into account the spin-orbit coupling of the excited electron [13].

In the Racah notation [80], an excited state is represented through the notation $n'l[K]_J$ or $n'l'[K]_J$. The prime after the l in the second option means that $j = 1/2$ ($j = 3/2$ in the first option). The first four excited levels of the gases studied in this work, e.g., are $(n + 1)s[3/2]_2^o$, $(n + 1)s[3/2]_1^o$, $(n + 1)s'[1/2]_0^o$ and $(n + 1)s'[1/2]_1^o$ in the Racah notation, where n is the principal quantum number of the last shell when the atom is in the ground state. The “ o ” in superscript stands for *odd parity* and is beyond the scope of this work.

Figures from 2.1 to 2.4 show the atomic energy level diagrams of neon, argon, krypton and xenon, respectively. The energy levels were taken from [81] and the ionization thresholds from [17]. In the diagrams are represented the stronger dipole-allowed transitions [82] taken from [83], [84], [85] and [86]. Continuous arrows (purple) correspond to Vacuum Ultraviolet (VUV) emissions, dash-dotted arrows (red) to visible and dashed arrows (brown) to Infrared (IR).

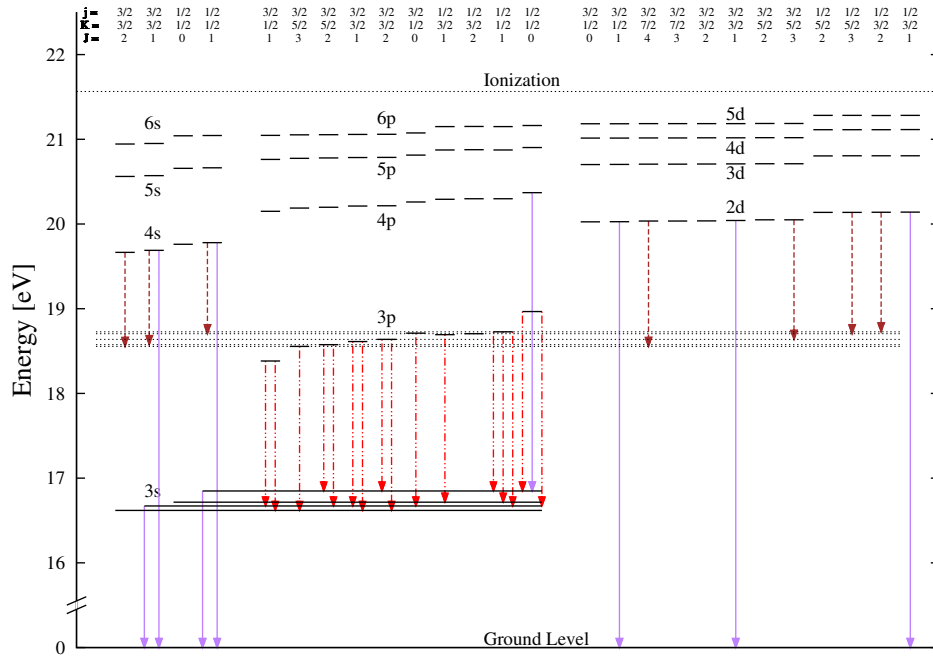


Figure 2.1: Simplified energy level diagram of neon and stronger dipole-allowed transitions. The lines of levels $3p [5/2]_3^o$, $3p [5/2]_2^o$, $3p [3/2]_2^o$, $3p' [3/2]_2^o$, and $3p' [1/2]_1^o$ were horizontally prolonged with dashed lines because some transitions from upper levels end on them.

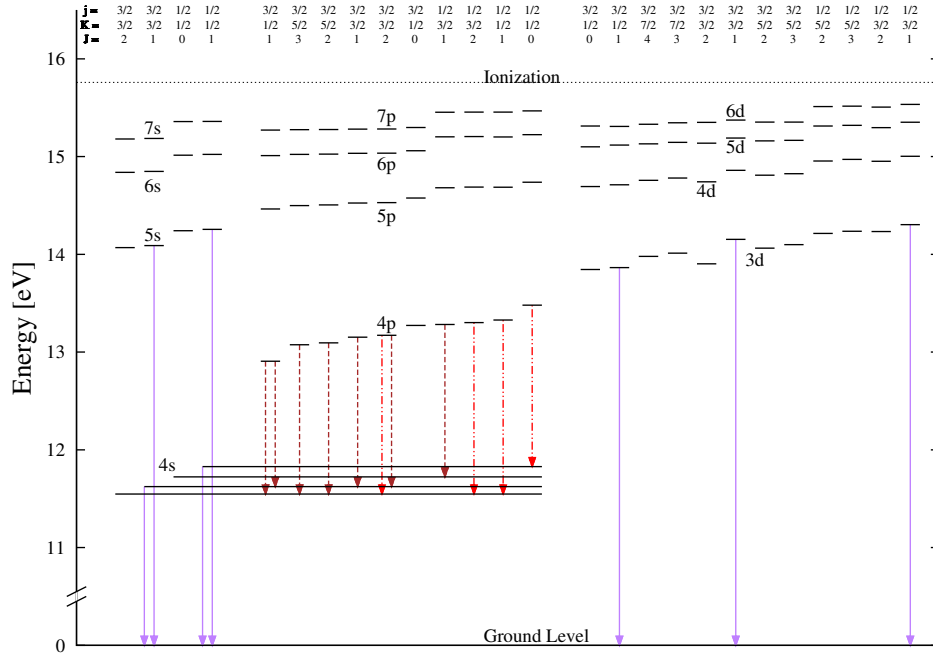


Figure 2.2: Simplified energy level diagram of argon and stronger dipole-allowed transitions.

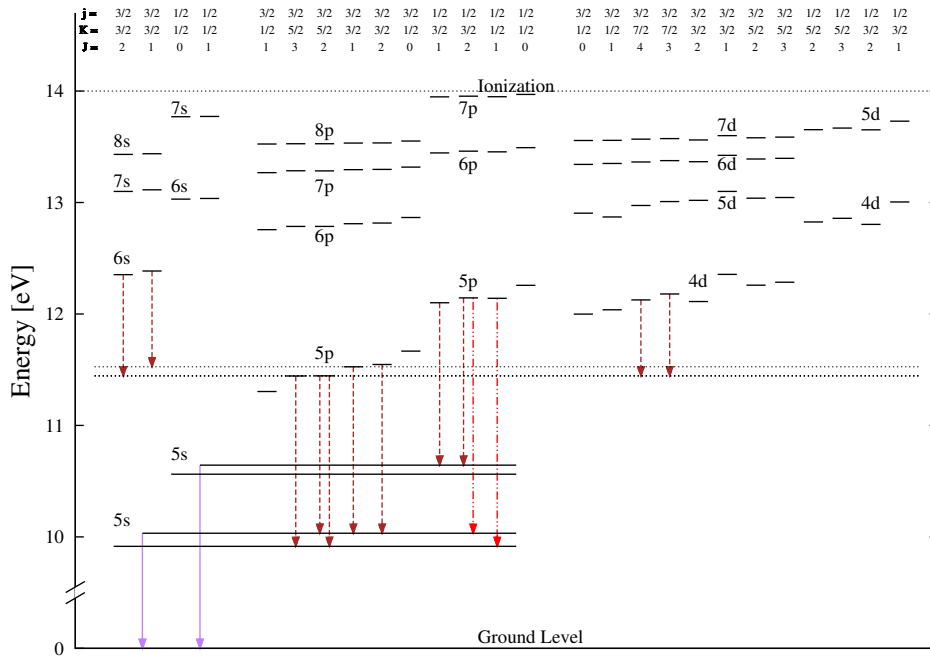


Figure 2.3: Simplified energy level diagram of krypton and stronger dipole-allowed transitions. The lines of levels $5p [5/2]_3^o$, $5p [5/2]_2^o$ and $5p [3/2]_1^o$ were horizontally prolonged with dashed lines because some transitions from upper levels end on them.

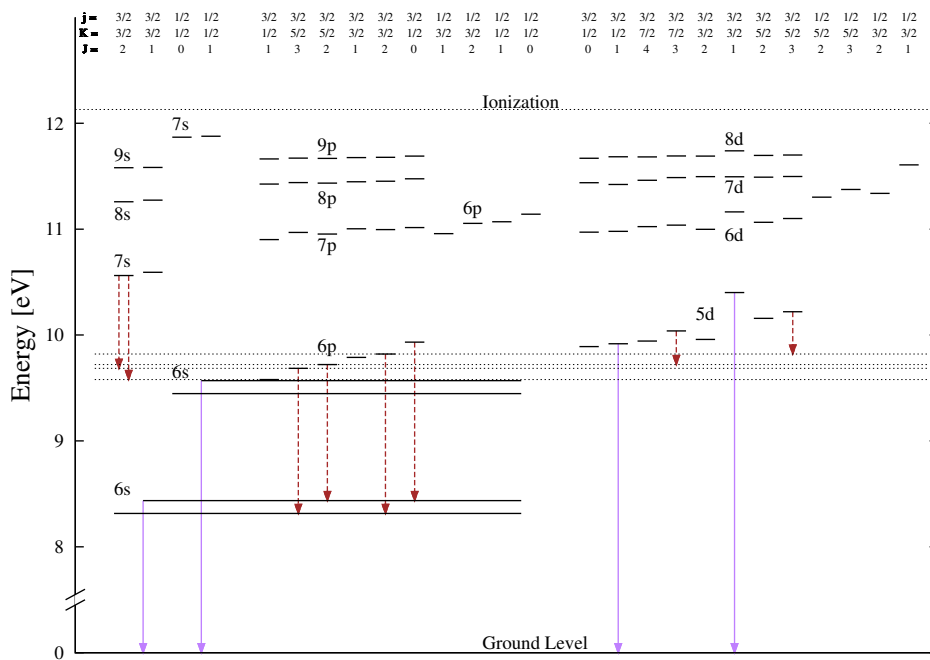


Figure 2.4: Simplified energy level diagram of xenon and stronger dipole-allowed transitions. The lines of levels $6p [1/2]_1^o$, $6p [5/2]_3^o$, $6p [5/2]_2^o$ and $6p [3/2]_2^o$ were horizontally prolonged with dashed lines because some transitions from upper levels end on them.

2.2 Electroluminescence modes

As stated in Chapter 1, in a gaseous detector, primary electrons are produced in the absorption / drift region as result of the interaction of incoming radiation with the gas. These primary electrons are driven, under the effect of a weak electric field that avoids recombination with ions, to the amplification region where a stronger electric field exists. In the case of ionization chambers, the amplification region does not exist in reality, there is only the drift field that guide the primary electrons to the collection electrodes. However, in order to easily generalize, this particular field will also be called the amplification field in the following lines.

As defined also in Chapter 1, the electroluminescence yield, Y , is the number of emitted photons per primary electron and per unit path length. Here we are interested in studying the behavior of these quantities as functions of the applied amplification electric field, $\|\vec{E}\| = E$. However, the atom density of the gas – the number of atoms per volume unit, N – varies with pressure and temperature. As N is changed, the mean free path of the electrons varies and thus the energy available for excitations, transferred to them between collisions, is different. Therefore, the dependence of Y with E is different for different pressure and temperature conditions and it is useful to normalize the relation between the yield and the field. Usually it is used the *reduced EL yield* – the number of emitted photons per primary electron and per unit of path length divided by the atom density, $(\frac{Y}{N})$ – as a function of the *reduced electric field* – the electric field intensity divided by the atom density, $(\frac{E}{N})$. The relation between these two quantities, in the EL proportional region, is thus valid for any macroscopic conditions of the gas phase. The SI unit of $(\frac{E}{N})$ is Vm^2 but usually the *Townsend* (Td) is used: $1 \text{ Td} = 10^{-21} \text{ Vm}^2$ [87]. Often, in many experimental descriptions, it is also used the reduced EL yield as a function of the reduced field in pressure units. Instead of being normalized to the atom density, Y and E are divided by the pressure of the gas, p . As a consequence, the dependence of $(\frac{Y}{p})$ with $(\frac{E}{p})$ varies with temperature, a fact that should always be taken into account when using this description.

Electroluminescence light in two different ranges can be produced using pure noble gases: VUV and Visible-IR (Vis-IR). Thus, it is convenient to define two different EL yields: $(\frac{Y}{N})_{\text{VUV}}$ and $(\frac{Y}{N})_{\text{Vis-IR}}$ for each of the ranges, respectively. Let's consider by simplicity a uniform field in the following analysis.

Between collisions, the primary electrons are accelerated and their kinetic energy is increased. For low values of $(\frac{E}{N})$, this energy is below the first excitation potential of the gas (see Figures 2.1 to 2.4) and thus electrons can collide only elastically with the gas atoms. Elastic collisions allow to transfer only kinetic energy to the atoms¹ that

¹A very small fraction of the electron kinetic energy is transferred to the atom in an elastic collision

does not lead to the emission of any kind of EL light: both $(\frac{Y}{N})_{\text{VUV}}$ and $(\frac{Y}{N})_{\text{Vis-IR}}$ are null for low values of $(\frac{E}{N})$.

From a given field value – the *VUV electroluminescence threshold*, $(\frac{E}{N})_{\text{VUV}}^{\text{thr}}$ – it becomes possible that in some collisions the electrons have kinetic energy equal or slightly higher than the excess energy of the first excited state of the atom, $(n + 1)\text{s}[3/2]_2^o$. Thus, it becomes possible that the drifting electron transfers energy to the atom exciting it. The excited atom returns to ground state emitting a VUV photon, as will be described in the Section 2.3. As $(\frac{E}{N})$ is increased, after an excitation collision, the electron can acquire again enough energy for other excitations and thus $(\frac{Y}{N})_{\text{VUV}}$ increases approximately linearly, since the available energy for excitations is directly proportional to the applied electrical potential.

The increase of the field also opens new channels of excitation – it is possible to excite the atom to new more energetic levels. At a certain point – the *Vis-IR electroluminescence threshold*, $(\frac{E}{N})_{\text{Vis-IR}}^{\text{thr}}$ – electrons can acquire enough energy to excite the atoms to shell configurations higher than $np^5(n + 1)\text{s}^1$. Atoms in these excited configurations transit, emitting a Visible or an IR photon (see Section 2.4), to one of the $np^5(n + 1)\text{s}^1$ levels which decay after to the ground state with emission of a VUV photon. Thus, each of these excited atoms leads to the emission of two photons: one in the VUV range and other in the Vis-IR range. In Figures 2.1 to 2.4, some of the stronger Vis-IR transitions are represented. As the field is increased, the available kinetic energy also increases and $(\frac{Y}{N})_{\text{Vis-IR}}$ grows linearly, although its slope is substantially lower than the one of $(\frac{Y}{N})_{\text{VUV}}$. In fact, since their energy is lower, $np^5(n + 1)\text{s}^1$ levels are more likely to be produced than the higher ones and, in addition, after a Vis-IR photon also a VUV photon is emitted.

Continuing to increase the electric field, above a certain value – the *ionization threshold*, $(\frac{E}{N})_{\text{ion}}^{\text{thr}}$ –, the electrons acquire now enough energy to ionize gas atoms. Additional secondary electrons will be then produced which, similarly to the primary electrons, undergo the same acceleration by the field and therefore also produce VUV and Vis-IR photons as well as new ionizations. In addition, the ions can also produce ultimately VUV EL photons after recombination with thermalized electrons (this process will be described in Section 2.3). As the number of secondary electrons increases exponentially with the field also $(\frac{Y}{N})_{\text{VUV}}$ and $(\frac{Y}{N})_{\text{Vis-IR}}$ increase exponentially with $(\frac{E}{N})$. In this way, EL and avalanche multiplications happen simultaneously.

In Figure 2.5 it is schematically shown the behavior of $(\frac{Y}{N})_{\text{VUV}}$ and $(\frac{Y}{N})_{\text{Vis-IR}}$ with the reduced amplification electric field. The VUV EL, the Vis-IR EL and ionization electric field thresholds are indicated in the plot.

due to the high difference of the collision partners masses.

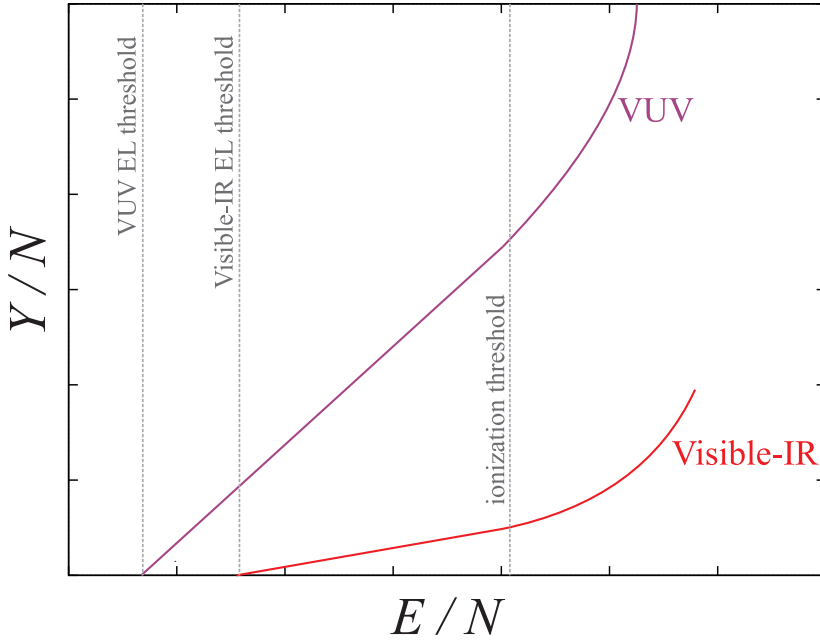


Figure 2.5: Reduced VUV EL and Vis-IR yields, $(\frac{Y}{N})_{\text{VUV}}$ and $(\frac{Y}{N})_{\text{Vis-IR}}$ respectively, as schematic functions of the reduced amplification electric field, $(\frac{E}{N})$.

2.3 VUV emission

Since their excitation potential is the lowest, the levels of the $np^5(n+1)s^1$ electronic shell configuration are the most populated through direct electron impact. These levels are also populated ultimately after the creation of excited atoms in shell configurations with energy higher than that of $np^5(n+1)s^1$ (as suggested by the Vis-IR transitions represented in Figures 2.1 - 2.4 and explained in Section 2.4). They are represented in Racah notation as $(n+1)s[3/2]_2^o$, $(n+1)s[3/2]_1^o$, $(n+1)s'[1/2]_0^o$ and $(n+1)s'[1/2]_1^o$. Two of them are metastable: $(n+1)s[3/2]_2^o$ has lifetimes of 38 s, 39 s and 43 s in argon, krypton and xenon [88, 89], respectively; and $(n+1)s'[1/2]_0^o$ has lifetimes of 128 ms in xenon [90]. The other two are resonant: $(n+1)s[3/2]_1^o$ and $(n+1)s'[1/2]_1^o$ have lifetimes of 20.5 ns and 1.7 ns in neon [91], of 8.6 ns and 2.15 ns in argon [92], of 4.6 ns and 4.4 ns in krypton [93], of 3.8 ns and 3.2 ns in xenon [94], respectively.

VUV photons emitted during atomic transitions from the resonant states are promptly re-absorbed by ground state atoms through the so-called *radiation trapping mechanism*, which implies a long effective lifetime. Indeed, as the pressure is increased above a few tens of mbar, the atomic emissions are progressively replaced by molecular emissions characterized by continua spectra, as observed in proportional scintillation [95, 96, 97]. As the pressure increases, the average time between collisions of the atoms decreases and start to be lower than the effective atomic radiative lifetimes, thus the probability of excimer formation gets large.

Excimers – electronically excited molecules, R_2^{**} – are formed through three-body collisions between an excited atom, R^* , and two atoms in the ground state, R :



Three-body collisions dominate at pressures above few tens of Torr making the excimer formation the main channel of de-population of excited atoms [98]. The rate constant of process (2.1) is $6.6 \times 10^{-33} \text{ cm}^6 \text{s}^{-1}$, $44 \times 10^{-33} \text{ cm}^6 \text{s}^{-1}$ and $25 \times 10^{-33} \text{ cm}^6 \text{s}^{-1}$, for argon, krypton and xenon [99]. This implies excimer formation times lower than 260 ns, 40 ns and 70 ns in each of the cases, respectively, at atmospheric pressure and room temperature. These values further decrease with the square of the pressure. In this work it is assumed that other processes, e. g. associative ionisation which affects highly excited states that are not frequently produced, contribute negligibly [100, 101].

The excimers involved in the VUV electroluminescence are mainly ${}^1\Sigma_u^+$ and ${}^3\Sigma_u^+$ [102, 103] with very different radiative decay rates: ${}^1\Sigma_u^+$ has radiative lifetimes of 4.2 ns and 5.5 ns in argon and xenon, respectively; and ${}^3\Sigma_u^+$ has lifetimes of 3.2 μs , 1.7 μs and 96 ns in argon, krypton and xenon, respectively [95, 104]. They are formed through process (2.1) in high vibrational states and can decay to the repulsive ground state, ${}^1\Sigma_g^+$, emitting a VUV photon:



or they can collide with ground state atoms losing vibrational energy:



In the latter case, the resultant excimer in a low vibrational state, R_2^* , emits a VUV photon with slightly lower energy:



The electronic transitions of excimers follow the Franck-Condon principle. It states that an electronic transition is so fast that the internuclear distance can be considered as fixed [105], corresponding to vertical arrows in a molecular energy diagram (as that of Figure 2.6). In this diagram, a vibrational state is represented by an horizontal line. The quantum theory shows that, in the fundamental vibrational state ($\nu = 0$) of each electronic molecular level, the atoms are most likely to be found in the equilibrium position. However, for higher vibrational states it is more probable to find the atoms near the intersection of the horizontal lines with the potential curve. A transition is favored if it occurs for an internuclear distance such that the vertical line connects

probable states of the molecule (represented as blue shadows in Figure 2.6). The potential energy of, e.g. the ${}^1\Sigma_u^+$ excimer of a noble gas, as a function of nuclei-nuclei distance, r , is depicted schematically in Figure 2.6. The potential curve of the ground state molecule, ${}^1\Sigma_g^+$, is also presented [102]. A ($\nu \neq 0$) ${}^1\Sigma_u^+$ excimer decays into the weakly bounding region of the ground state at large internuclear distance r_2 such that both vibrational wave functions overlap, giving rise to a narrow *first continuum*. A ($\nu = 0$) ${}^1\Sigma_u^+$ excimer decays into the repulsive region of the ground state, which leads to the dissociation of the atoms. The kinetic energy of the formed atoms is not quantised resulting in the broad *second continuum* [106]. The two continua, the first at higher and the second at lower frequencies, are observed experimentally for low pressures (< 100 mbar).

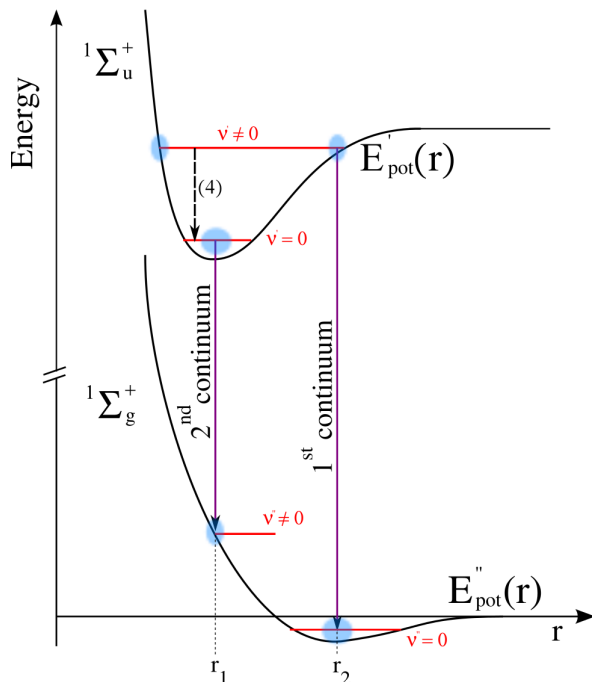


Figure 2.6: Energy diagram of the ground state ${}^1\Sigma_g^+$ and the ${}^1\Sigma_u^+$ excimers [102]. The curves are not precise. The amplitude of the shallow potential well of the ground state is exaggerated. The red lines represent vibrational states. Blue shadows show the most probable regions of finding the valence electrons, for each vibrational state.

At high pressures, typically above 400 mbar, the proportional electroluminescence spectra show only the second continuum because process (2.3) dominates over process (2.2) [95]. The second continuum is approximately Gaussian with a wavelength mean of 82.2 nm, 128 nm, 147 nm, and 173 nm and a FWHM of 3 nm, 10 nm, 12 nm and 14 nm for neon, argon, krypton and xenon, respectively [95, 96, 97, 107].

As seen, in a pure noble gas, each excited atom, in whatever state it was produced,

leads ultimately to the emission of a VUV photon. Thus, the VUV electroluminescence threshold corresponds to the minimum electric field that allows the electrons to acquire energy equal or higher than the first excitation potential. In literature, Monte Carlo calculations report values for $(\frac{E}{N})_{\text{VUV}}^{\text{thr}}$ of 0.77 Td for neon, 3.6 Td for argon, 2.72 Td for krypton and between 2.87 and 2.89 Td for xenon [108, 109, 110]. The best experimental works report thresholds of 2.35 Td for argon, 2.36 Td for krypton and 3.39 Td for xenon [67, 68, 111]. Experimentaly, curves for $(\frac{Y}{N})_{\text{VUV}}$ as a function of $(\frac{E}{N})$ have been determined only for argon and xenon, using GSPCs with uniform electric fields and LAAPDs for light readout and yield calibration [67, 68].

VUV emission from ions

In the case that the electric fields used for signal amplification are higher than the ionization threshold of the gas, ion pairs are produced, each one constituted by one secondary electron and one ion, R^+ . For noble gases at atmospheric pressure or higher, the ions form quickly (< 5 ns) molecular ions, R_2^+ , by colliding with atoms in the ground state [112]:



These molecular ions can recombine with thermalized electrons forming highly excited atoms, R^{**} , through a process called *dissociative recombination*:



Although, in principle, there are not thermalized electrons in the amplification volume since all of them are being accelerated by the electric field, this reaction can happen with electrons from the cathode, when the ion is collected. The highly excited atoms collide with other atoms of the gas forming excimers in highly energetic electronic states, R_2^{***} which, on their turn, collide with further ground atoms forming normal excited atoms (equal to those produced through direct electron impact):



The excited atoms R^* undergo the processes from (2.1) to (2.4) giving rise to VUV photons as described previously. In this way, when charge amplification is involved, VUV photons are emitted after ionizations, in addition to those from excited atom de-excitations.

2.4 Visible and Infra-Red emission

As suggested by the energy diagrams presented in Figures from 2.2 to 2.4, after the excitation of noble gas atoms through electron impact to shell configurations with energies higher than those of $np^5(n+1)s^1$, photons in the Visible and Infra-Red range are emitted. In fact, light of this nature has been observed experimentally by applying EL electric fields to electrons produced by incident radiation at atmospheric pressures. The spectra consist in atomic lines corresponding to wavelengths between 580 nm and 725 nm, 695 nm and 845 nm, 755 nm and 895 nm, 820 nm and 885 nm for neon, argon, krypton and xenon, respectively [113]. These lines are attributed to transitions from the levels in the $np^5(n+1)p^1$ shell configuration to those of $np^5(n+1)s^1$ configuration [114]. Atoms in the $np^5(n+1)p^1$ configuration can be directly created by electron impact or by cascade population from highly excited states, namely np^5nd^1 and $np^5(n+2)s^1$ [115, 116]. This population from upper levels can happen through collisions between the excited atom and a ground state atom, or through radiative transitions. In the last case the involved wavelengths ($> 1 \mu m$) are out of the spectral sensitivity range of conventional light readout devices.

Regarding the Vis-IR reduced EL yield, only recently was measured experimentally $(\frac{Y}{N})_{\text{Vis-IR}}$ as a function of $(\frac{E}{N})$ for a uniform electric field, and this only for argon [117]. In this reference a Vis-IR EL threshold of $(\frac{E}{N})_{\text{Vis-IR}}^{\text{thr}} = 6.43 \text{ Td}$ is reported.

CHAPTER 3

Simulation toolkit

Up to now, for calculating the electroluminescence yield and efficiencies, a three-dimensional Monte Carlo program of the electron drift in xenon and xenon-neon mixtures [109, 108] and an one-dimensional program for krypton and argon [110] existed. Although validated, they are not open-source nor freely accessible, unlike the toolkit described in this document. These programs were built aiming the determination of the intrinsic properties of rare gases VUV electroluminescence, like yields and efficiencies, but are limited to implementations of uniform electric fields. The toolkit presented in this document provides a versatile and comprehensive microscopic parametrization of the physics processes involved in the drift of electrons in gaseous detectors. With it, it is possible to calculate yields and efficiencies not only of VUV EL, but also of Vis-IR EL. Nearly any arbitrary geometry can be considered due to interfaces with finite elements and boundary element programs for field calculations. It uses a detailed up-to-date database of electron-atom and electron-molecule cross sections for about 60 gases, which provides the potential to simulate EL of nearly arbitrary gas mixtures.

The simulation toolkit was developed using the new C++ implementation of the microscopic technique of Garfield [118]. This is a Monte Carlo technique which tracks the electrons at the atomic level using, currently, cross sections and routines of Magboltz 8.9.5 [119].

3.1 Garfield

Garfield is a program widely used for the detailed simulation of gaseous detectors [120], developed by R. Veenhof. In order to perform these simulations, the knowledge of the electric field vector, $\vec{E} = (E_x, E_y, E_z)$, in each point of the trajectories described by the electrons and/or the ions is mandatory. Garfield has its own library for analytically calculating electric fields when the detector geometry can be decomposed in equipotential planes, wires and tubes without intersections. For the remaining geometries, the program provides interfaces with finite element programs and efforts are being done in order to interface the recent developed Nearly Exact Boundary Element Method [121].

Considering only electrostatic fields, and if the electrons produced by the incoming radiation traveled in vacuum they would have a deterministic trajectory in the detector, given their initial position and velocity. This trajectory would be such that the position as a function of the time, $\vec{r}(t)$, should obey to the following differential equation:

$$m \frac{d^2 \vec{r}(t)}{dt^2} = e \vec{E}(\vec{r}(t)) \quad (3.1)$$

where m and e are the mass and the electric charge of the particle. Garfield implements the Runge-Kutta-Fehlberg method to solve numerically this differential equation and

determines the trajectory that ions or electrons would have in vacuum. In a real gas, one ion, due to its high mass, follows this trajectory with very small thermal fluctuations. This is the method that Garfield uses to drift ions also in real gases, given their mobility as a function of the electric field for calculation of the time of drift. In the case of electrons, since they are extremely light, they change abruptly their direction of motion in collisions with the atoms and the trajectories obtained by solving Equation (3.1) do not provide a real parametrization, although they can be viewed as the paths traveled on average by the electrons (the blue paths presented in Figure 1.13b) were obtained with this method).

In order to correctly simulate the drift of electrons in real gases, Garfield has other integration method named *microscopic technique*. It is a Monte Carlo method that tracks electrons at the atomic/molecular level by using procedures and cross-sections available in Magboltz. The implementation of the technique is described in more detail in the next Section. In noble gases each collision is classified as elastic, excitation or ionization but the program can deal with other processes, typical of molecular gases, as attachment and super-elastic collisions (a process in which the electron gains energy).

3.2 Magboltz

Magboltz was developed by S. Biagi, to calculate the transport parameters of electrons drifting in gases under the influence of electric and magnetic fields [122]. For this purpose, the program contains, for 60 gases, electron cross sections for all relevant interactions with atoms and/or molecules. The cross sections used for neon, argon, krypton and xenon in version 8.9.5 of the program (the one used in this work) are plotted in Figures A.1 and A.2. In Tables A.1 – A.4 are shown in detail the considered separated groups of interactions for these gases and the corresponding spent energy. Regarding excitations (the key process for EL simulations), cross sections are available for 45, 44, 4 and 50 levels/groups of each gas, respectively. These cross sections are part of the LXcat project [123], which is an open-access website that collects ELECtron SCATtering cross sections and swarm parameters required for modeling low temperature plasmas.

Electron transport

As seen before, each electron follows a sinuous path drifting in the gas. This is the combination of the parabolic vacuum trajectories between collisions with the abrupt changes in the direction of motion during collisions. If the electron starts its drift in the position $\vec{r}_0 = (x_0, y_0, z_0)$ and with an initial velocity $\vec{v}_0 = (v_{0x}, v_{0y}, v_{0z})$, and if

the electric field is considered constant, immediately before its next collision with an atom, happening in a time interval Δt after the previous collision, the new position $\vec{r}_1 = (x_1, y_1, z_1)$ and velocity $\vec{v}_1 = (v_{1x}, v_{1y}, v_{1z})$ of the electron will be:

$$\begin{cases} x_1 = x_0 + v_{0x}\Delta t + \frac{1}{2}\frac{e}{m}E_x\Delta t^2 \\ y_1 = y_0 + v_{0y}\Delta t + \frac{1}{2}\frac{e}{m}E_y\Delta t^2 \\ z_1 = z_0 + v_{0z}\Delta t + \frac{1}{2}\frac{e}{m}E_z\Delta t^2 \end{cases} \quad (3.2)$$

and

$$\begin{cases} v_{1x} = v_{0x} + \frac{e}{m}E_x\Delta t \\ v_{1y} = v_{0y} + \frac{e}{m}E_y\Delta t \\ v_{1z} = v_{0z} + \frac{e}{m}E_z\Delta t \end{cases} \quad (3.3)$$

Determined the position and the velocity just prior to a collision, these quantities are updated accordingly to the collision type, after which they are considered as new vacuum drift initial conditions and the process repeated. But for this, the free time of flight between each pair of collisions, Δt , should be known.

For a fixed velocity of the electron, Δt follows an exponential distribution centered at the *mean free time* between collisions, τ . The probability of having a free time of flight Δt is thus:

$$P(\Delta t) = \exp\left(-\frac{\Delta t}{\tau}\right) \quad (3.4)$$

or equivalently, using the *mean collision frequency*, $\nu = 1/\tau$:

$$P(\Delta t) = \exp(-\nu\Delta t) \quad (3.5)$$

The mean collision frequency can be calculated from the gas atom density, N , and from the *total cross section*, σ :

$$\nu = N\nu\sigma \quad (3.6)$$

The total cross section is obtained summing the cross sections off all possible interactions for the considered velocity of the electron, σ_i :

$$\sigma = \sum_i \sigma_i \quad (3.7)$$

Taking into account Equation (3.5), between each pair of collisions, the free time of flight could be obtained using a random number with uniform distribution, $S \in]0, 1[$, through:

$$\Delta t = -\nu^{-1} \ln(S) \quad (3.8)$$

But, in reality, the mean collision frequency varies along the parabolic path between collisions due to the change on the electron velocity. The probability of having a free time of flight Δt is in this case:

$$P(\Delta t) = \exp \left(- \int_{t=0}^{\Delta t} \nu \left(\| \vec{v}_0 + \frac{e}{m} \vec{E} t \| \right) dt \right) \quad (3.9)$$

and Δt could be determined using a uniform distributed random number, S , and the relation $P(\Delta t) = S$. The numerical determination of Δt through this relation, with a reasonable accuracy, is extremely computationally time consuming and not suitable for practical applications. In order to overcome this limitation, the *null-collision technique* is used in Magboltz.

Null-collision technique

In the null-collision technique, introduced by H. R. Skallerud in 1968 [124], it is considered a trial collision frequency, ν' , which is greater than the actual collision frequency for all the velocity range achieved between collisions, $\nu(v)$. The use of a large collision frequency is compensated by considering a given fraction of the collisions as *null collisions* – with null momentum transfer and thus that don't affect the electron path. In this way, the trial collision frequency is the sum of the actual and the null collision frequencies:

$$\nu' = \nu(v) + \nu_{\text{null}}. \quad (3.10)$$

The probability of a null collision is thus:

$$P_{\text{null}} = \frac{\nu_{\text{null}}}{\nu'} = 1 - \frac{\nu(v)}{\nu'}. \quad (3.11)$$

The simulation procedure is as follows:

1. Given the initial velocity \vec{v}_0 and position \vec{r}_0 of one electron, ν' is chosen to be greater than $\nu(v)$ over a velocity range corresponding to at least one mean free time between collisions.
2. Using ν' , a trial free time of flight $\Delta t'$ is randomly generated according to relation (3.8), which can lead to two different cases:
 - (a) $\nu' \geq \nu(v)$ for $t \in]0, \Delta t']$:
The electron collides at the instant $t = \Delta t'$ through a real or a null collision.

The decision is made through the generation of a random number uniformly distributed $S \in]0, 1[$, according to Equation (3.11):

- i. If $S < \nu(v)/\nu'$, then a true collision happened and the free time of flight is determined. The position of the electron is updated according to Equation (3.2). The velocity vector is updated according to the collision process (elastic, ionization or excitation). This update takes into account the energy loss, ϵ_{loss} , associated with the process and the anisotropic distribution in the scattering angle. The process is repeated from step 1 with the new initial conditions and a new ν' .
In the case that the collision is an excitation, in addition, an EL simulation model is applied as will be described in Section 3.3. In the case it is an ionization, initial conditions for a new electron are generated and put on a stack for later simulation.
- ii. $S \geq \nu(v)/\nu'$, then a null collision happened. The velocity vector is updated according to Equation (3.3), a new trial collision frequency is chosen and the process is repeated from step 2 until a true collision has happen.

(b) $\nu' < \nu(v)$ for some value of $t \in]0, \Delta t']$:

A too low trial collision frequency has been chosen for some fraction of the trajectory. According to Equation (3.11) this would imply a negative probability for the null collisions. The electron is brought back to the conditions where ν' equaled the true collision frequency $\nu(v)$. This happened for a velocity v_m (determined through the relation between ν and v) and at the instant of time:

$$\Delta t = \frac{\sqrt{v_m^2 - v_{0\perp}^2} - v_{0\parallel}}{\frac{e}{m} \parallel \vec{E} \parallel}, \quad (3.12)$$

where $v_{0\perp}$ and $v_{0\parallel}$ are the perpendicular and parallel components of the velocity immediately after the previous collision, relatively to the local electric field vector, respectively.

The simulation of one electron stops when it hits a metal conductor (electrode) or an insulator. The secondary electrons that possibly were created through ionizations are then tracked, one by one, through the same methodology. In Figure 3.2 it is represented the flow-chart of the simulation performed by Magboltz. Each time S is used, it is given a new value to it. N_{ion} , N_{VUV} and $N_{\text{Vis-IR}}$ are counters to determine the number of secondary electrons, VUV and Vis-IR photons produced per primary electron, respectively.

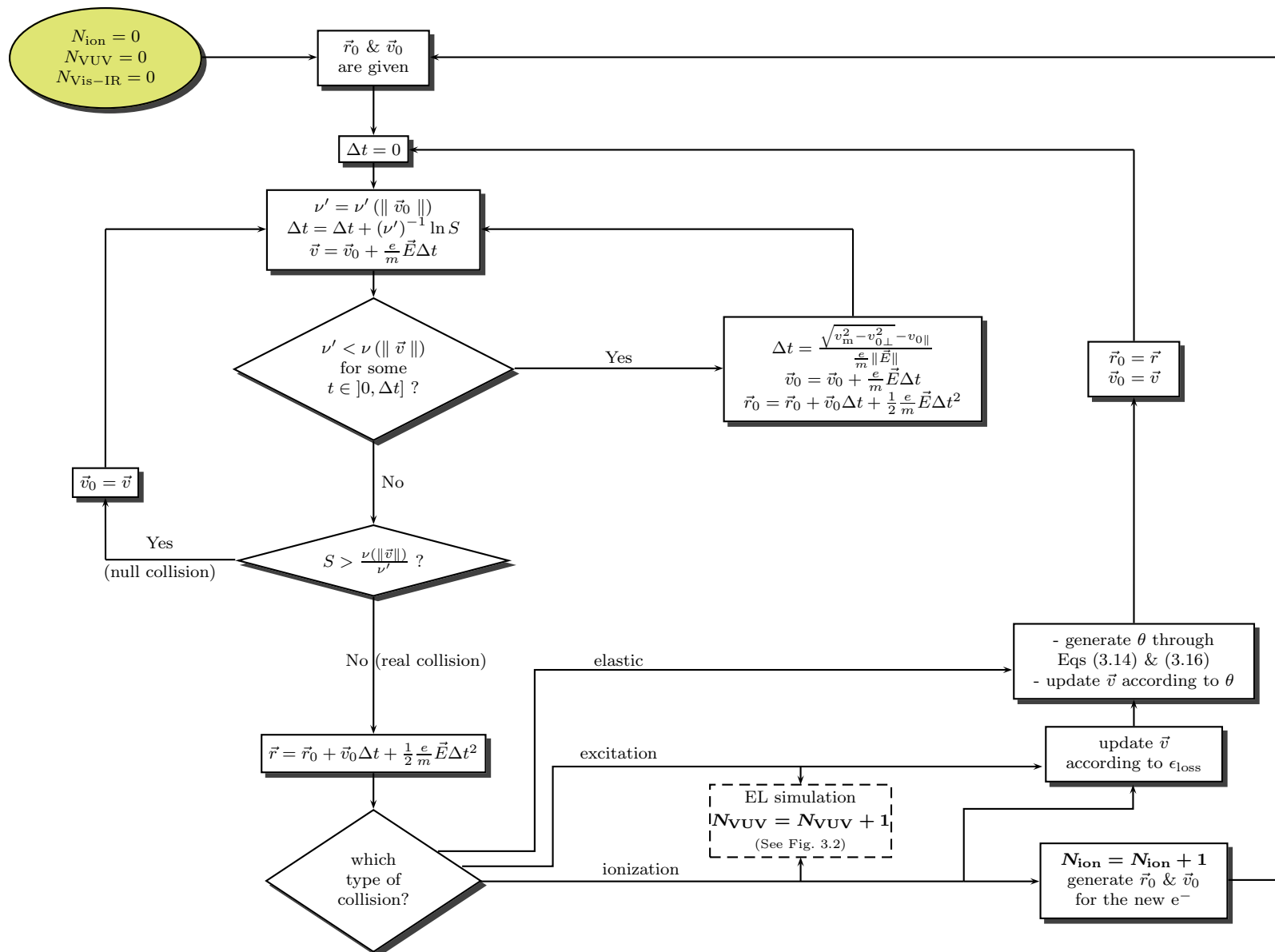


Figure 3.1: Block diagram of the Monte Carlo simulation performed in Magboltz 8.9.5. The methodologies of the null collision method and of the anisotropic scattering are included.

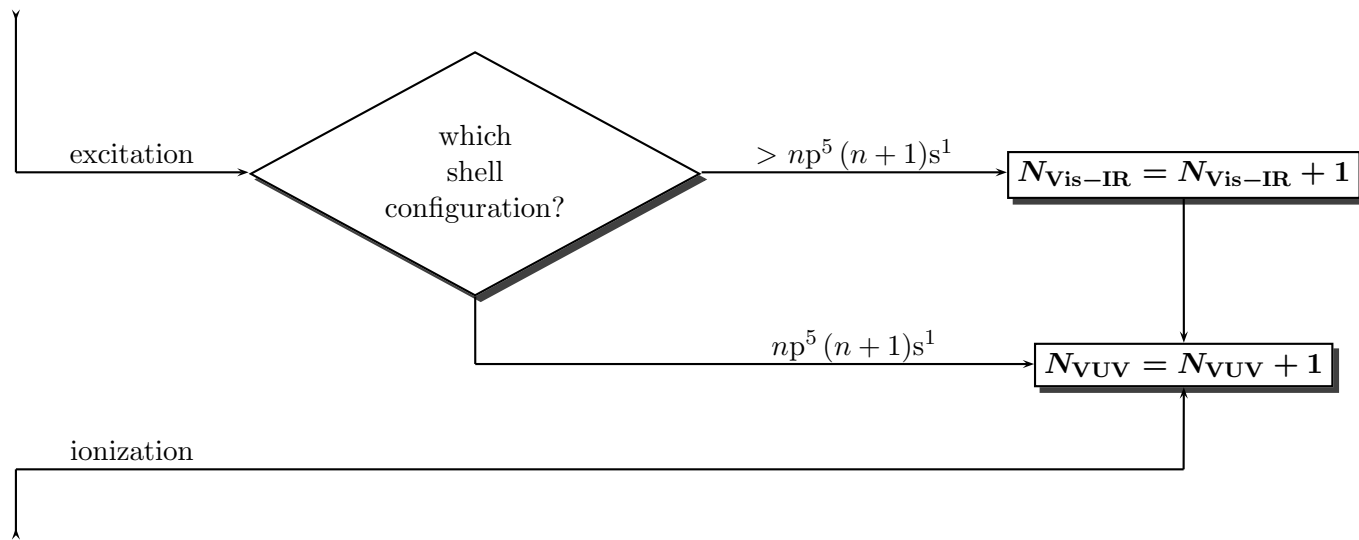


Figure 3.2: Part of the block diagram that refers to the EL simulation. Excitations and ionizations imply ultimately the emission of a VUV EL photon. In the case that the result of the excitation is an atom in a shell configuration different of $np^5(n+1)s^1$, one Vis-IR photon is also emitted.

Anisotropic scattering

In each real collision, the anisotropic angular distribution of the scattering angle is considered. In literature, it is available experimental data on the *differential scattering cross section*, $\sigma_{\text{diff}}(\theta)$, of some gases [125, 126]. This quantity is related to the probability of the electron being scattered according to a given angle, θ , and gives a direct information for Monte Carlo simulations. Moreover, the total cross section is defined as the integral of the differential cross section over all possible scattering angles:

$$\sigma = 2\pi \int_0^\pi \sigma_{\text{diff}}(\theta) \sin \theta d\theta, \quad (3.13)$$

Although the information about the differential cross section gives a direct method to implement an anisotropic scattering in Monte Carlo simulations, Magboltz implements a different formalism, in order to cover generally all gases contained on its database. This formalism is based on the fact that the scattering angle can be randomly sampled using the ratio between the *momentum transfer cross section*, σ_m , and the total cross section, which can be expressed as [127]:

$$\frac{\sigma_m(\epsilon)}{\sigma(\epsilon)} = \frac{1 - \xi}{2\xi^2} \left((1 + \xi) \ln \frac{1 + \xi}{1 - \xi} - 2\xi \right), \quad (3.14)$$

where ϵ is the kinetic energy of the electron and ξ is an energy dependent parameter. The momentum transfer cross section is a measure of the loss of forward momentum of electrons drifting through the gas and defined as [128]:

$$\sigma_m = 2\pi \int_0^\pi \sigma_{\text{diff}}(\theta) \sin \theta (1 - \cos \theta) d\theta. \quad (3.15)$$

The parameter ξ is determined, in each collision, by solving numerically Equation (3.14), given that σ_m and σ are known. After, the scattering angle is determined using a uniformly distributed random number, S , in the interval $]0, 1[$:

$$\theta = \arccos \left(1 - \frac{2S(1 - \xi)}{1 + \xi(1 - 2S)} \right). \quad (3.16)$$

In Figures A.1 and A.2 the elastic momentum transfer cross section of each gas is represented as EMT and the total elastic cross section as ELT.

3.3 C++ toolkit

The toolkit used for the simulations performed during this work consists on a library of C++ classes, which implements the microscopic technique that was already available on Garfield 9 (implemented firstly in Fortran) and described in the previous two

Sections. This collection of C++ classes, written by H. Schindler and R. Veenhof, can be interfaced with more general simulation platforms, widely used in the simulation of particle detectors as e. g. GEANT4 [129, 130]. The last is a toolkit for the simulation of detectors in high energy, nuclear and accelerator physics, medical and space science, and has some limitations leading with gaseous detectors. These are treated through parametrization of their macroscopic properties that sometimes are not enough for accurate and detailed results. In this point, the new C++ implementation of the microscopic technique of Garfield will certainly play a role.

The toolkit is interfaced with ROOT [131], a C++ framework developed at CERN for data analysis in High Energy Physics, which provides visualization of the detector geometries, electric fields, electron and ion tracks, among other capabilities. This interface with ROOT also allows the user to perform further data analysis, expanding very significantly the toolkit versatility.

For each collision, information about the collision type, the (x, y, z) position, the instant of time and the energy loss (according to Tables A.1 – A.4) is available.

Simulation of EL

Regarding the excitations, the level/group to which the atom transited is also available. A part of the work developed for this thesis consisted in the implementation of the decay processes described in Sections 2.4 and 2.3, given the detailed informations about each excited atom obtained through the toolkit, in order to assess the EL properties of pure noble gases in several detector geometries. As outlined in Figure 3.2, all excitations and ionizations imply ultimately the emission of a VUV EL photon. In the case that the result of one excitation is an atom in a shell configuration different than np^5 ($n + 1$) s^1 , a possible Vis-IR photon is also considered to be emitted.

Regarding the VUV EL, one important quantity to determine is the EL efficiency, which implies to know the energy (or equivalently the wavelength) of the emitted VUV photon. The spectra of the VUV EL at the atmospheric pressure or higher, can be considered as a Gaussian distribution with a mean of 82.2 nm, 128 nm, 147 nm, and 173 nm and a FWHM of 3 nm, 10 nm, 12 nm and 14 nm for neon, argon, krypton and xenon, respectively. The wavelength of each VUV photon is generated according to these distribution using the gaussian random number generator of the `TRandom3` class of ROOT.

Although this work has been focused in the study of EL of pure noble gases, potentially the toolkit is not limited to that. It has potential to simulate EL of several mixtures of any of the 60 gases available in the database. An interesting gas is, e.g., tetrafluoromethane (CF_4) due to its high EL yield. Recently, D. Nygren has proposed

the addition of small quantities of trimethylamine (TMA) or dimethylamine (DMA) to gaseous xenon in order to further decrease the fluctuations in the primary charge creation (described in Section 1.1.3) [132]. These molecules will potentially have a *Penning effect*, reducing the fluctuations in the creation of primary charge, at the same time that emit light in the 280 – 310 nm range. The Penning effect happens in mixtures where one of the gases has an ionization potential lower than the other. One atom of the second gas, excited through electron impact, can transfer in collisions its excess energy to one atom of the first gas ionizing it and producing additional secondary electrons. However, further studies are needed in order to confirm these properties and to determine the optimal conditions of operation such as concentrations to be used and electric fields to be applied. In this context, the C++ toolkit described and used in this work will be of major importance.

In order to simulate EL in such mixtures, a detailed radiative and collisional decay model can be constructed and implemented for each mixture. Unlike in pure noble gases, this is not an easy task for mixtures, since many decay channels exist and absolute and accurate decay rates for each of them should be first experimentally determined. Anyway, work has already been done in order to include Penning transfers in the simulations of electron drift in argon based mixtures [133].

CHAPTER 4

EL in uniform electric field

In order to understand in detail the microscopic processes related with electroluminescence in noble gases, it was considered as a first approximation the case when electrons drift in a volume where a uniform electric field is applied. This geometry, due to its simplicity, allows in an intuitive way, to evaluate the different intrinsic properties of EL.

In this chapter, the collision rates of each of the levels/groups used in Magboltz are determined as functions of the reduced electric field. This analysis gives an idea of the most produced excited states for each value of electric field and therefore, allows to assess which contribute more significantly for EL. With this information in hands, the excitation efficiency can be estimated. The distribution of the kinetic energy of electrons prior to each collision is presented for different values of the electric field. The VUV EL efficiency and the corresponding yield are also calculated for all the studied gases and compared with experimental data and some earlier Monte Carlo work available for argon and xenon. For the first time, the fluctuations in the number of emitted VUV photons per primary electron are calculated as a function of the field. Finally, the Vis-IR EL yield is estimated for pure argon and xenon, being the results obtained for argon compared with very recent experimental measurements.

4.1 Simulation details

In order to obtain the simulation results presented in the next Sections of this Chapter, the primary electrons were considered to drift in a gas volume between two infinite parallel plates that create a uniform electric field. The starting direction of each primary electron was sampled isotropically and the starting energy was distributed according to the energy distribution given by Magboltz for the considered reduced electric field, which makes that electrons were already in equilibrium with the electric field when released. More details about other conditions as the gas temperature and pressure, the number of simulated primary electrons, N_e , and the distance traveled by each of them, will be given in each following section.

4.2 Collision rates

Figure 4.1 presents the average number of collisions, undergone per primary electron, corresponding to some of the levels/groups of Magboltz, as a function of the reduced electric field. The number of simulated primary electrons used in the calculations was, at least, 3×10^4 . All electrons were left to drift over 2 cm along the direction of the electric field. The considered temperature and pressure were 293 K and 1 atm,

respectively.

The np^5 ($n + 1$) s^1 states represent $\sim 90\%$ of all excitations in the proportional EL region. This is due to their energy being the smallest of all possible excited levels, which makes them the more likely to be produced. The next higher energy states, those of np^5 ($n + 1$) p^1 shell configuration, represent $5 - 10\%$, depending on the gas and on the intensity of the field. The remaining states represent a negligible fraction off all excitations, at least in the field range of this study.

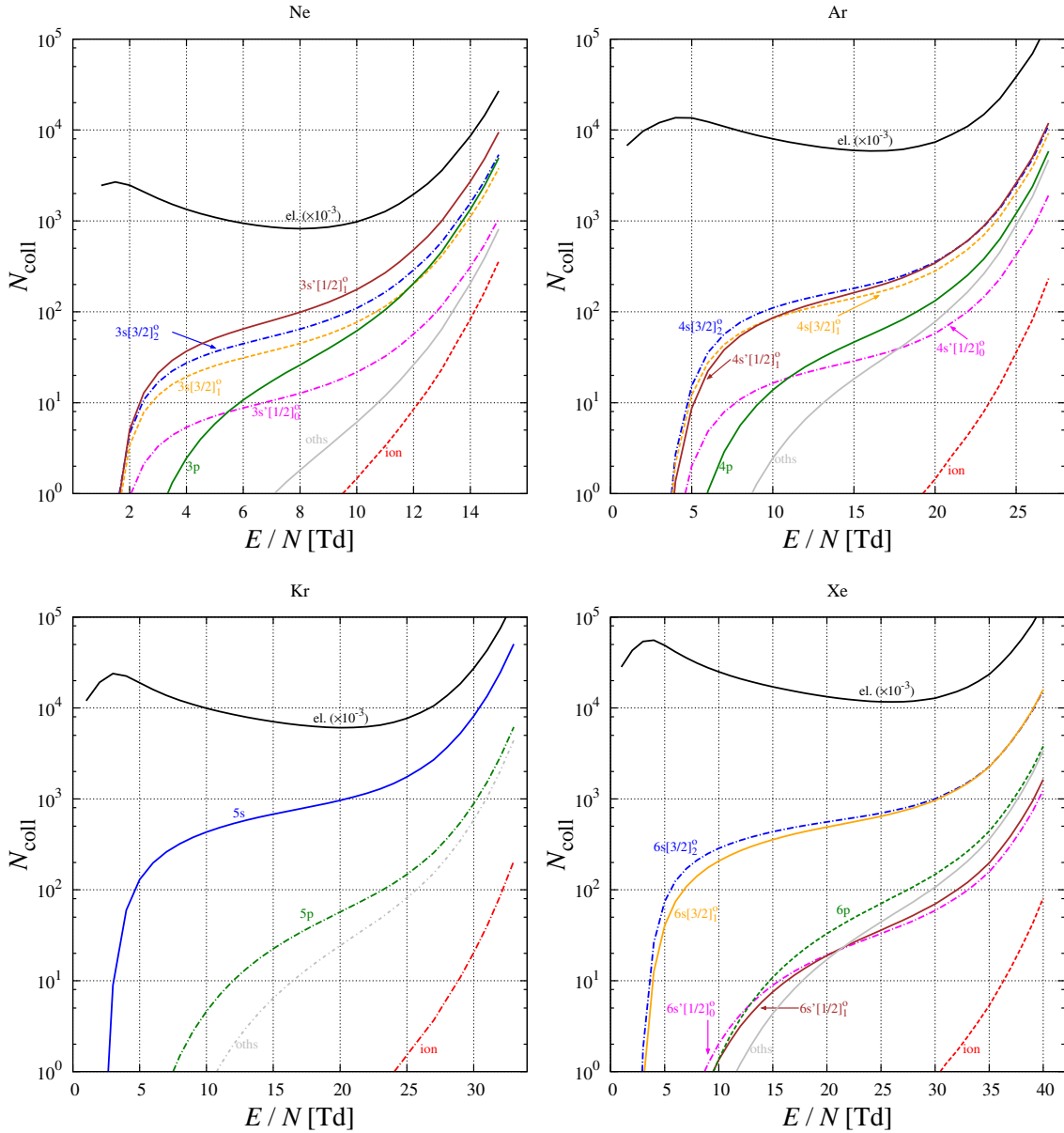


Figure 4.1: Average number of collisions (elastic, ionizations and of some excitation groups/levels) per primary electron drifting over 2 cm of gas at 293 K and 1 atm. The collisions experienced by secondary charges when ionization is possible are also included.

4.3 Energy distribution

Figure 4.2 shows the distributions of the electron kinetic energy before collisions, ϵ , for some values of the reduced electric field and for all the studied gases. As the electric field increases, between collisions, the electrons are more accelerated and can achieve higher energies. Also, for the same fluctuations in the electron mean free path (related to the stochastic nature of the electron drift), higher fields imply higher variations in the electron energy and thus, the distributions get broader. Higher energies imply an higher number of possible excitation channels, which also contributes to this effect. Figure 4.2b resumes the behavior of the maximum energy of electrons as well as their mean energy. The graphs of both figures were constructed, for each gas, considering one electron drifting until 10^9 collisions have been totaled. The collisions experienced by secondary electrons when ionization is possible were also included. The considered temperature and pressure were 293 K and 1 atm, respectively.

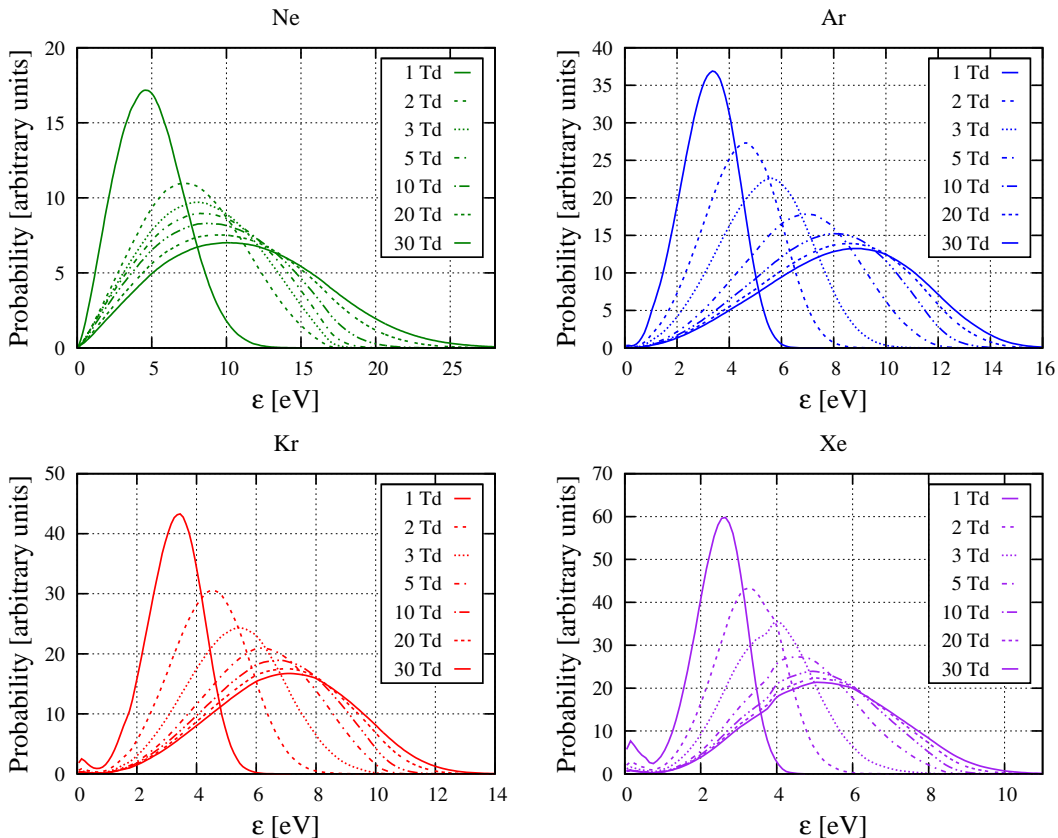


Figure 4.2: Distributions of the electron kinetic energy before each collision, for some values of $(\frac{E}{N})$ and for the gases studied in this work.

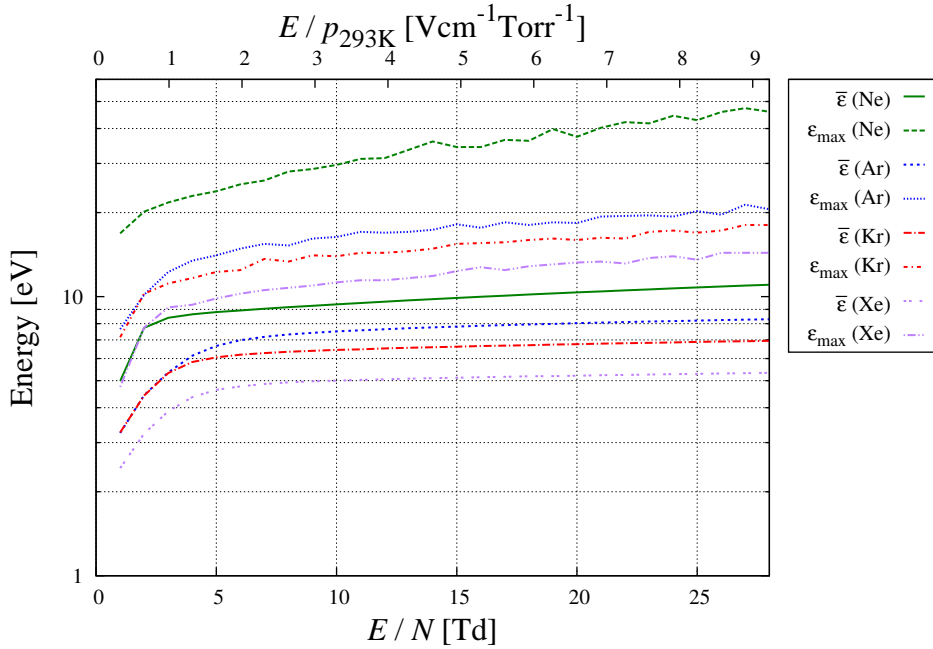


Figure 4.3: Mean and maximum kinetic energies, $\bar{\epsilon}$ and ϵ_{\max} respectively, reached by the electrons before collisions, as functions of the reduced electric field. These quantities were obtained by analysis of the electron energy distributions (some of them present in Figure 4.2).

4.4 Excitation efficiency

The excitation efficiency, Q_{exc} , is defined as the fraction of energy acquired by the N_e primary electrons drifting under effect of the electric field, E , that is spent in excitations [109]. It can be calculated through:

$$Q_{\text{exc}} = \frac{\sum_{i=1}^{i=n_{\text{exc}}} n^i \varepsilon_{\text{exc}}^i}{ezN_e E} \quad (4.1)$$

where n_{exc} is the number of excitation levels/groups available in Magboltz for the studied gas, n^i the number of excitations to the i^{th} group produced by the primary electrons, $\varepsilon_{\text{exc}}^i$ the corresponding energy loss, z the projection of the distance traveled by each primary electron into the electric field direction and e the elementary charge.

Figure 4.4 shows the excitation efficiency, for each of the studied gases, as a function of the reduced electric field. The temperature and pressure used in the simulations were 293 K and 1 atm, respectively. The number of simulated primary electrons used in the calculations was, at least, 3×10^4 for each value of the field. All electrons were left to drift over 2 cm along the direction of the electric field.

When the electric field supplies to electrons enough energy that excitation starts

to be possible, the corresponding cross sections increase abruptly and Q_{exc} begins with a fast increase. Increasing the field, a plateau is reached until the field is high enough to provide electrons with enough energy for ionizations. After that, also the additional produced secondary electrons can excite atoms and thus, Q_{exc} reaches values much higher than 100 %. This quantity, in argon, krypton and xenon, agree for high ($\frac{E}{N}$) with earlier Monte Carlo simulations [109, 110]. Below 8 Td the values in this work are ~ 10 % lower in the case of argon and xenon. The difference increases with decreasing field. Anyway, this region is not interesting for operating detectors based on electroluminescence amplification because of the large statistical fluctuations and the low EL yield (see Sections 4.5.2 and 4.5.3).

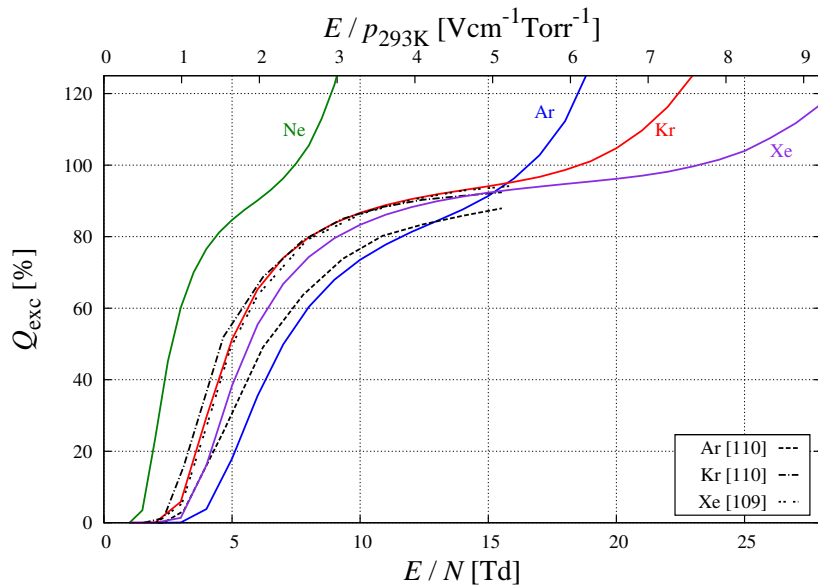


Figure 4.4: Excitation efficiency, Q_{exc} , as a function of the reduced electric field. The results obtained in this work are compared with those of earlier Monte Carlo work [109, 110].

The high values of excitation efficiency achieved before ionizations (>80 % for all gases) means that almost the energy supplied by the electric field is spent in excitations. Knowing that, as described in Chapter 2, when using a pure noble gas, all excited atoms produce ultimately a VUV photon, this means that the VUV EL yield should be high and the associated fluctuations should be low, since the exchange of energy with other processes is small. After all, it should be noted that Q_{exc} is not 100 % for any field in the proportional EL range. The remaining fraction of energy is lost in elastic collisions. In each of them, the electron loses a very small amount of energy (due to the very small ratio between its mass and the mass of the atom). This means that, between excitations, a big number of elastic collisions happen (this can be also

found in Figure 4.1). This highlights the need to ensure experimentally an extremely high purity of the gas. If even a small fraction of electronegative impurities exists in the gas, the electrons would lose energy in processes such as attachment, not reaching enough kinetic energy for excitations.

4.5 Intrinsic properties of VUV EL

In this Section, the intrinsic properties of VUV EL of pure noble gases are presented as functions of the reduced electric field. The number of primary electrons simulated and used in the calculations, for each value of $(\frac{E}{N})$, was varied between 3×10^4 and 2×10^5 in order to keep the variation in J (defined in Equation (1.18)) below 2 % in the last quarter of iterations (see Figure 4.9 for examples of the variation of J with the number of simulated primary electrons.). All primary electrons were left to drift over 2 cm along the direction of the electric field. It was considered a temperature of 293 K and a pressure of 1 atm.

4.5.1 VUV EL efficiency

The VUV electroluminescence efficiency, Q_{VUV} , is defined as the ratio between the energy emitted in the form of VUV photons and the energy acquired by the electrons during the drift:

$$Q_{\text{VUV}} = \frac{\sum_{i=1}^{i=n_{\text{exc}}} \sum_{j=1}^{j=n^i} \varepsilon_{\text{EL}}^{i,j}}{ezN_e E} \quad (4.2)$$

where $\varepsilon_{\text{EL}}^{i,j}$ is the energy of the VUV de-excitation photon of the j^{th} excited atom in the i^{th} group through excimer decay, generated randomly according to the characteristics of the second continuum.

Figure 4.5 shows the obtained Q_{VUV} as a function of the reduced electric field. The behavior of this quantity is similar to that of the excitation efficiency, already analyzed in Section 4.4. One difference is that Q_{VUV} is always lower than the excitation efficiency, due to the loss of vibration energy from excimers before they emit a VUV photon, and to Vis-IR radiative transitions from levels of shell configurations with energy higher than $np^5(n+1)s^1$ – the Vis-IR EL. In the case that these levels are de-populated through collisional transitions, the lost energy also contributes to the difference between Q_{VUV} and Q_{exc} . The ratio between Q_{VUV} and Q_{exc} represents the fraction of energy transferred to atoms as excitations that is emitted in the form of

VUV photons and is represented in Figure 4.6. With the increase of the field, electrons achieve higher energies, exciting atoms to higher states and losing more energy per excitation. However, the energy of each VUV photon is more or less the same (according to the distribution of the second continuum) and thus, the ratio slightly decreases. This means that, for higher fields, more energy is lost as Vis-IR transitions or collisions involving highly excited atoms, leading ultimately to the population of the np^5 ($n + 1$) s^1 states.

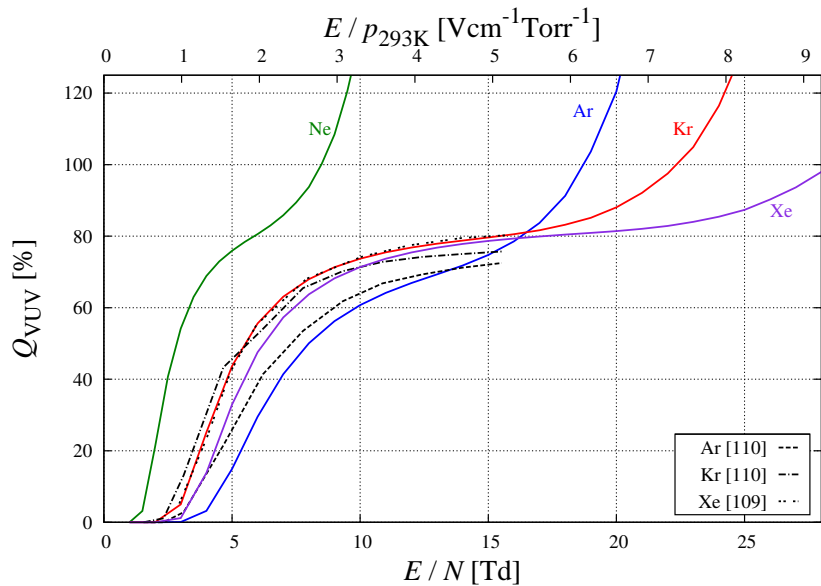


Figure 4.5: VUV electroluminescence efficiency, Q_{VUV} , as a function of the reduced electric field. The results obtained in this work are compared with those of earlier Monte Carlo work [109, 110].

4.5.2 VUV EL yield

The reduced electroluminescence yield, previously defined in Section 2.2, is a very important quantity to be evaluated since, with it, one has information about the number of EL photons that can be produced in a detector implementing a uniform field geometry, for a given value of the field. This quantity can also be used to estimate, through extrapolation, the number of photons produced in other geometries.

Figure 4.7 shows the reduced VUV EL yield, $(\frac{Y}{N})_{VUV}$, obtained in this work, as a function of the reduced electric field. Results of earlier Monte Carlo simulations for xenon [109] and measurements for argon and xenon [68, 67] are also presented. The linear trends of all curves presented in the Figure are systematized in Table 4.1. The overall agreement consolidates the assumption that the channels of de-population of excited atoms produces ultimately VUV photons through excimer decay. If other

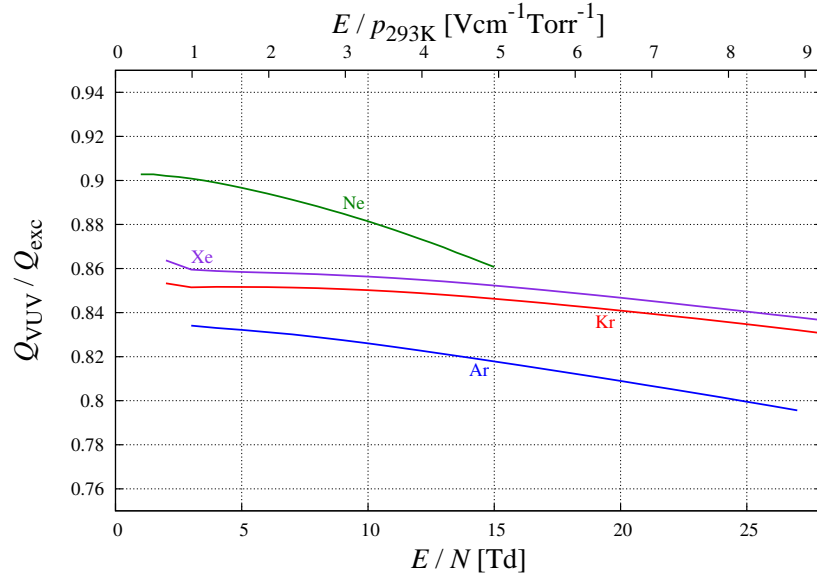


Figure 4.6: Fraction of energy transferred to atoms as excitations that is emitted in the form of VUV photons, as a function of the reduced electric field.

processes contribute they should also lead to the emission of VUV photons. The exception in the agreement is argon below 8 Td which is under investigation. The good agreement between the simulated values and measurements available for argon and xenon also consists of a validation of the toolkit.

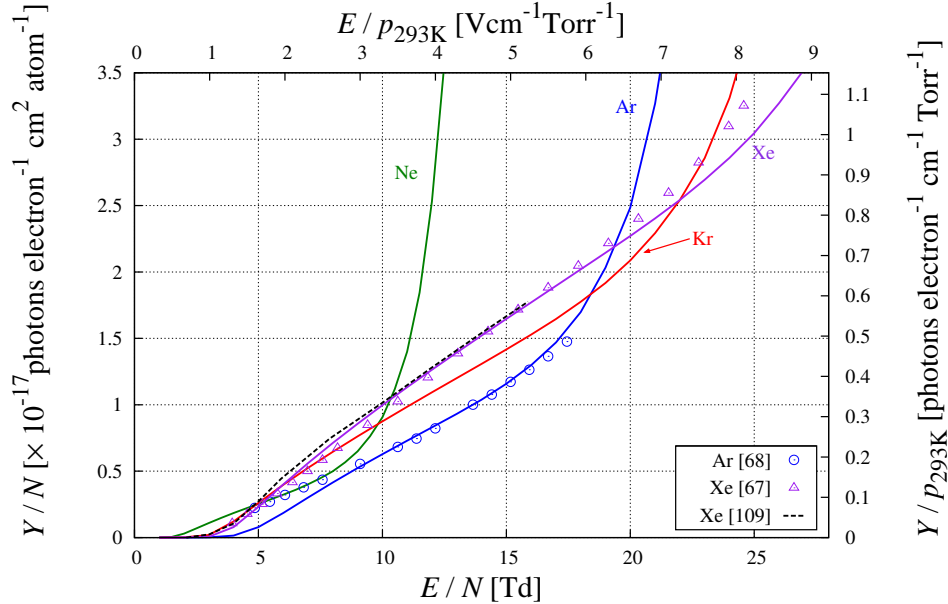


Figure 4.7: Reduced VUV EL yield, as a function of the reduced electric field, compared with earlier Monte Carlo simulation data for xenon [109] and measurements for argon and xenon [68, 67].

Work	Linear trend
	Ne
This work	$(\frac{Y}{N})_{\text{VUV}} = (0.0727 \pm 0.0006) (\frac{E}{N}) - (0.110 \pm 0.003)$
	Ar
This work	$(\frac{Y}{N})_{\text{VUV}} = (0.105 \pm 0.001) (\frac{E}{N}) - (0.43 \pm 0.01)$
Measurement [68]	$(\frac{Y}{N})_{\text{VUV}} = 0.081 (\frac{E}{N}) - 0.190$
	Kr
This work	$(\frac{Y}{N})_{\text{VUV}} = (0.116 \pm 0.001) (\frac{E}{N}) - (0.30 \pm 0.01)$
	Xe
This work	$(\frac{Y}{N})_{\text{VUV}} = (0.134 \pm 0.001) (\frac{E}{N}) - (0.39 \pm 0.02)$
Monte Carlo [109]	$(\frac{Y}{N})_{\text{VUV}} = (0.1389 (\frac{E}{N}) - 0.4020) \pm 0.0328$
Measurement [67]	$(\frac{Y}{N})_{\text{VUV}} = 0.140 (\frac{E}{N}) - 0.474$

Table 4.1: Linear trends of the reduced VUV EL yield dependence with the reduced electric field of the data plotted in Figure 4.7. $(\frac{E}{N})$ is given in Td ($1\text{Td} = 10^{-17} \text{ V cm}^2 \text{ atom}^{-1}$) and $(\frac{Y}{N})_{\text{VUV}}$ is given in units of $10^{-17} \text{ photons electron}^{-1} \text{ cm}^2 \text{ atom}^{-1}$.

The reduced VUV EL yield increases approximately linearly with $(\frac{E}{N})$ at low fields, even when some ionization is produced (see Fig. 4.8). Above ~ 7 Td, ~ 15 Td, ~ 18 Td and ~ 22 Td respectively for neon, argon, krypton and xenon, secondary electrons, exciting and producing additional EL, change the linear behavior of $(\frac{Y}{N})_{\text{VUV}}$. These thresholds are in good agreement with those calculated for neon and xenon in reference [134]. For lower values of $(\frac{E}{N})$, the probability of ionization is too low for changes in the linear behavior of the yield to be detected.

The slopes increase from the lighter to the heavier gas and reflect the decrease in the minimum energy required to produce one excitation. The ground atoms of each gas have one more filled electronic shell than the previous. The additional shell shields the attraction of the valence electrons by the nuclei, thus decreasing the excitation

potential.

Xenon is the gas that gives the highest VUV EL gains in the linear region, followed by krypton, argon and neon. Extrapolating the yield, the VUV EL threshold, $(\frac{E}{N})_{VUV}^{thr}$, was determined to be 1.51 ± 0.04 Td, 4.1 ± 0.1 Td, 2.6 ± 0.1 Td and 2.9 ± 0.1 Td for neon, argon, krypton and xenon, respectively, in good agreement with earlier Monte Carlo calculations [110, 134].

Neon, although it has the highest minimum excitation energy, has the lowest VUV EL threshold. This is due to neon having the smallest elastic cross section of all gases studied. Thus, the energy needed for excitations is achieved for lower fields than in the case of the other gases (see Figure 4.3).

The first Townsend coefficient, α , measures the amount of ionizations produced per unit length path of the electrons. The values obtained dividing the number of ionizations per primary electron by the drift distance, are shown in Figure 4.8.

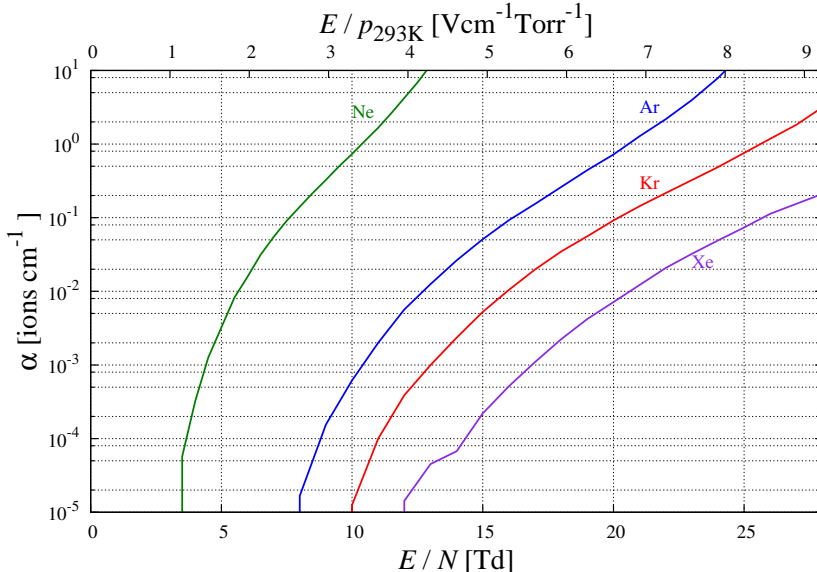


Figure 4.8: Calculated First Townsend coefficient, α , as a function of reduced electric field for all studied gases at 293 K and 1 atm.

4.5.3 Fluctuations

The fluctuations in the number of produced EL photons are an important parameter to be evaluated since, together with the fluctuations associated with the primary charge production, it gives information about the intrinsic energy resolution [70]. This intrinsic resolution corresponds to the better performance that can be achieved by using a given gas, regardless of the photodetection system. The contribution of the VUV EL fluctuations are usually neglected since they are small when compared to the primary

charge fluctuations. But, the simulations performed in this work allow to calculate them and to confirm if indeed they can be neglected.

The fluctuations associated with VUV EL are described by J_{VUV} , defined more generally for any type of EL in Equation (1.18):

$$J_{\text{VUV}} = \frac{\sigma_{\text{VUV}}^2}{\bar{N}_{\text{VUV}}} \quad (4.3)$$

where σ_{VUV}^2 is the variance in the number of VUV photons emitted per primary electron, N_{VUV} . The calculation of this parameter requires a minimum number of simulated primary electrons in order to reach the suitable statistics. The last depends on the used electric field. As an example, in Figure 4.9 it is shown, for xenon, the convergence of J_{VUV} with the number of simulated primary electrons used for the calculations. For fields where excitations happen but not ionizations, the convergence of J_{VUV} is fast (see Figure 4.9a)). For higher fields, the convergence is much slower due to excitations produced also by secondary electrons. In the plot of Figure 4.9b) are visible the abrupt changes in the value of J_{VUV} , for low statistics, when the additional primary electron causes an avalanche.

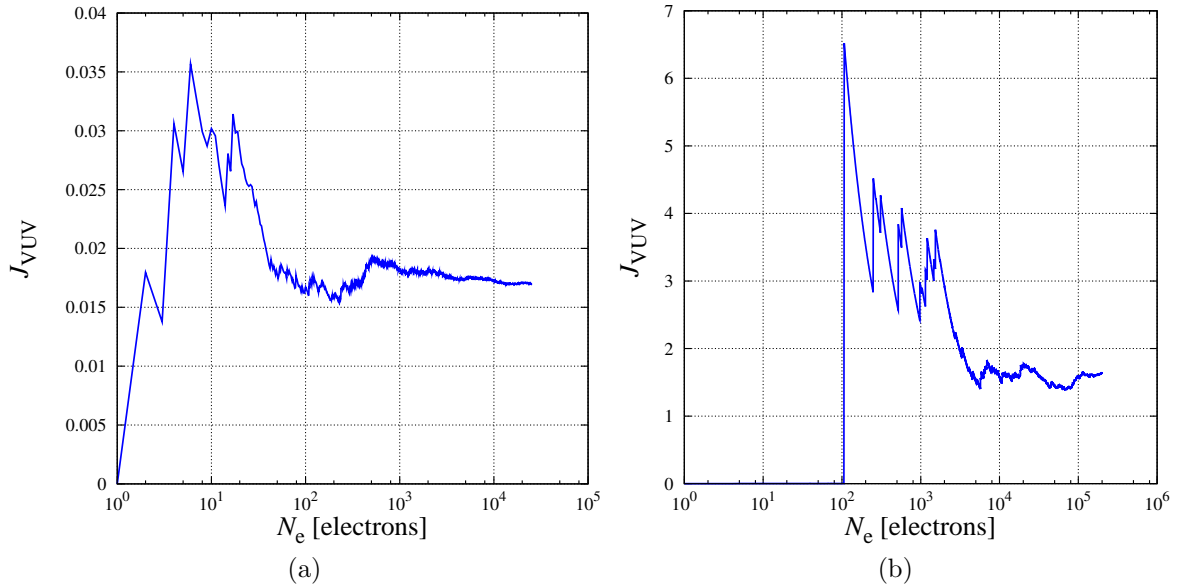


Figure 4.9: Convergence of J_{VUV} with the number of simulated primary electrons for (a) $(\frac{E}{N}) = 10 \text{ Td}$ – bellow the ionization onset; (b) $(\frac{E}{N}) = 18 \text{ Td}$ – above the ionization onset, obtained simulating electrons drifting over 2 cm of xenon at 293 k and 1 atm.

Figure 4.10 shows the value for which J_{VUV} converged, as a function of the reduced electric field. Xenon is the gas that exhibits the lowest statistical fluctuations, followed by krypton, argon and neon. For electric fields above the VUV EL threshold, as the field increases, J_{VUV} decreases until the onset for ionization collisions is reached. At

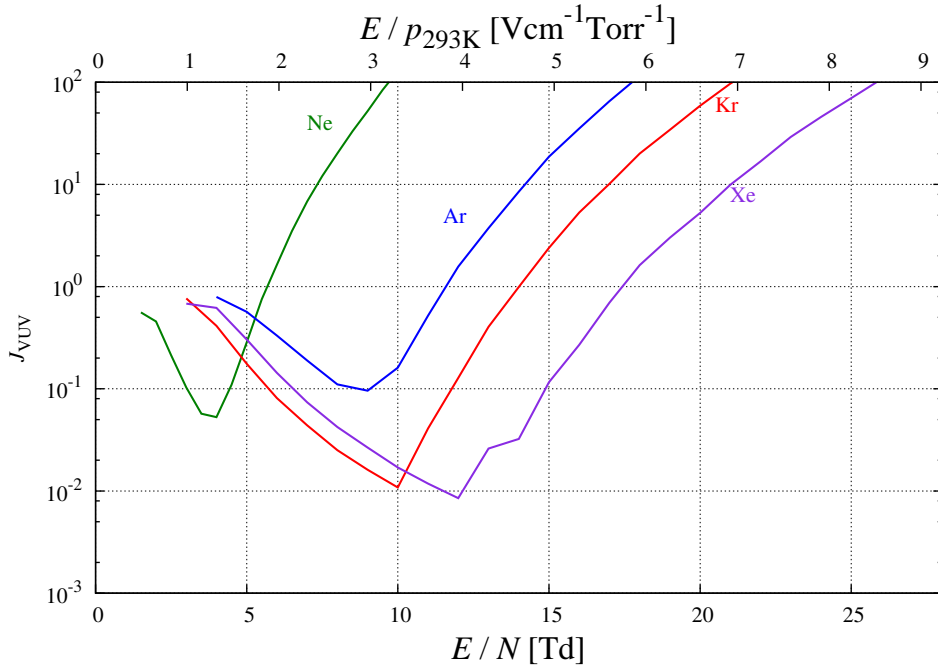


Figure 4.10: Fluctuations in VUV EL, described by J_{VUV} , as a function of the reduced electric field, for 2 cm of drift in each gas (at 293 K and 1 atm).

this point, J_{VUV} begins to increase because the higher fluctuations in the secondary charge gain start to dominate.

It is possible, through analysis of Figure 4.10, to confirm that the statistical fluctuations associated to proportional VUV EL are much lower than those in both charge avalanche multiplication and primary electron cloud formation (typical values of F are between 0.17 and 0.23, and of f between 0.2 and 0.6, as mentioned in Section 1.3.1), reinforcing the benefits of using EL as amplifying method of the charge signal created by particles in gaseous detectors.

4.6 Vis-IR EL yield

As mentioned in Section 2.4, light in the Vis-IR range has been experimentally observed together with VUV EL. This light is attributed to radiative electronic transitions from levels in the $np^5(n+1)p^1$ shell to those of the $np^5(n+1)s^1$ configuration. Atoms in the $np^5(n+1)p^1$ configuration can be directly created through electron impact or simultaneously by cascade population from highly excited states as np^5nd^1 or $np^5(n+2)s^1$. However, the model that represents the overall set of transitions between these levels is not well established, being difficult to determine what and which fraction of transitions give rise to Vis-IR photons. Thus, in a first attempt to simulate

and reproduce the measurements recently published by A. Buzulutskov et al [117], in this work two approaches were considered: the first assumes that only np^5 ($n + 1$) p^1 levels give rise to Vis-IR photons; and the second assumes that any level in a shell configuration different of np^5 ($n + 1$) s^1 produces ultimately a Vis-IR photon (the second also includes the levels considered in the first). In principle, the actual curve of the reduced Vis-EL yield, as a function of the field, should be between the curves given by these two approaches.

In order to compare the results obtained through simulations with those obtained experimentally, the same macroscopic conditions of the gas were considered: a temperature of 163 K and a pressure of 0.60 atm. The simulation of exactly the same conditions is important for electric fields for which ionization is possible, since different conditions imply different absolute quantities of secondary charges (that also produce EL). The curves of $(\frac{Y}{N})_{\text{Vis-IR}}$ as function of $(\frac{E}{N})$ have slight different shapes for these field ranges, according to the absolute number of produced secondary electrons. The simulations were performed for argon and also for xenon, the gases most interesting from the standpoint of possible applications. It was considered an EL gap of 2 mm, being the starting vertical position (perpendicular to the infinite planes that create the field) uniformly sampled along the gap. The number of simulated primary electrons used in the calculations was 3×10^4 , for each value of $(\frac{E}{N})$.

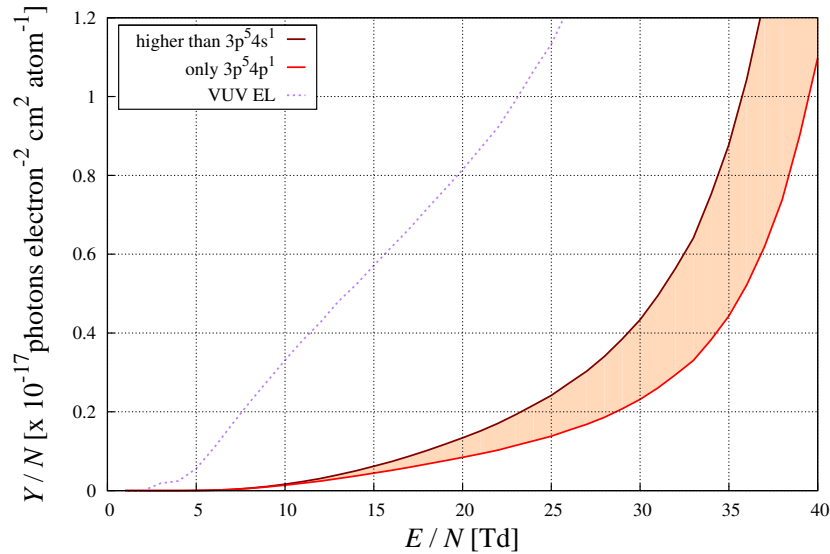


Figure 4.11: Reduced Vis-IR EL yield for argon, as a function of the reduced electric field, for the two considered simulation approaches. The results were obtained considering a temperature of 163 K, a pressure of 0.60 atm and a EL gap of 2 mm width. The VUV yield is also included.

In Figure 4.11 it is shown the reduced Vis-IR yield for argon, as a function of the re-

duced electric field, for the two considered approaches. In this case, in order to perform the same analysis considered in reference [117], it is used the average electron drift path (1 mm) instead of the width of the EL gap. As a reference, the VUV yield, obtained under the same simulation conditions, is also presented. Whatever the approach, a Vis-IR EL threshold of ~ 6 Td was obtained, in agreement with the measured value of 6.5 Td reported in reference [117]. In order to compare the results with those of reference [117], the reduced yield was normalized, dividing the reduced Vis-IR yield by the total number of charges collected in the anode electrode, per primary electron. The result is shown in Figure 4.12, together with the measured data. Indeed, the measured reduced yield is, within errors, between the two considered approaches, which make of them a starting point for the accurate simulation of Vis-IR EL in gaseous detectors. The reduced yield normalized to the produced secondary charge decreases after ~ 35 Td because the secondary electrons produce EL between their point of creation and the anode, a path which length is lower than that traveled by the primary electrons. This effect is higher for higher fields because a larger number of secondary electrons are produced more close to the anode, producing a small amount of EL photons.

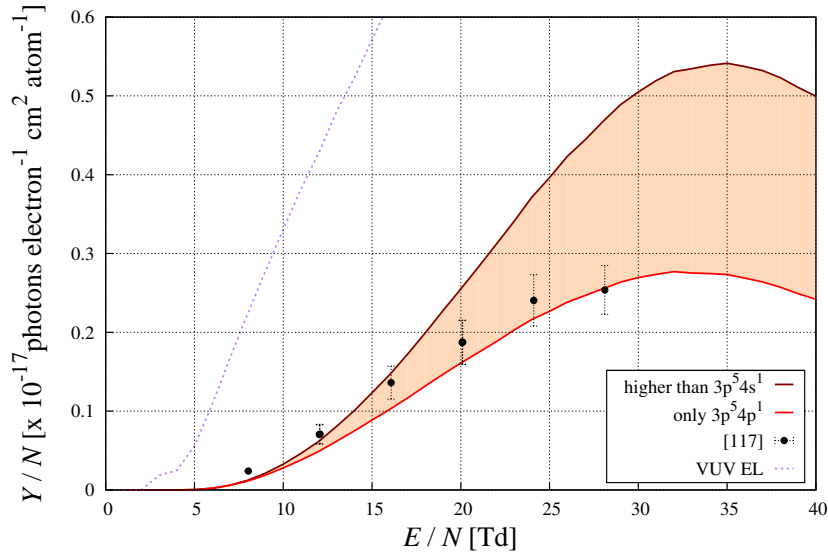


Figure 4.12: Reduced Vis-IR EL yield for argon, normalized to the total charge collected in the anode, as a function of the reduced electric field, for the two considered simulation approaches. The results were obtained considering a temperature of 163 K, a pressure of 0.60 atm and a EL gap of 2 mm width. The VUV yield is also included.

In Figure 4.13 is shown the simulated reduced Vis-IR EL yield for xenon, obtained in the same way as for argon. Xenon is an interesting gas in terms of possible applications but for which there is not measurements to compare. A Vis-IR EL threshold of ~ 11

T_d is obtained.

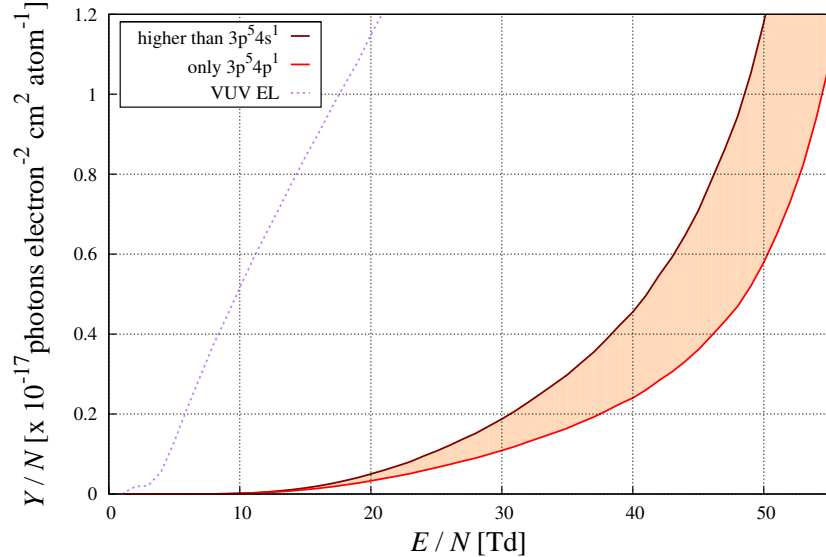


Figure 4.13: Reduced Vis-IR EL yield for xenon, as a function of the reduced electric field, for the two considered simulation approaches. The results were obtained considering a temperature of 163 K, a pressure of 0.60 atm and a EL gap of 2 mm width. The VUV yield is also included.

In both gases (argon and xenon) although one order of magnitude lower than the VUV yield, the obtained Vis-IR EL yield shows that the light produced in this range can be an interesting option to explore. It could allow to use cheaper and less complex readout systems as standard PMTs for the Vis-IR range. These have an higher detection efficiency than those used for VUV light and don't need to be covered with wavelength shifters or to use quartz windows; advantages that could overcome the low magnitude of the yield when compared to VUV light.

The use of signal amplification through Vis-IR EL can be specially interesting for detectors operating in avalanche regimes as PCs, MWPCs or MPGDs. At high fields, typical of these regimes, the fraction of produced excited levels through electron impact which give rise to the production of Vis-IR photons approaches the fraction of those giving rise only to VUV photons (a tendency which can be observed in Figure 4.1). This is a consequence of the increase in the mean kinetic energy of the electrons with the increase of the applied electric field, which makes increasingly likely levels with higher energies to be produced.

In order to be possible a more accurate simulation of the Vis-IR secondary light emission in these themes, a detailed model of decay among the several states that populate the $np^5(n+1)p^1$ configuration, and also of the decay of the last to the $np^5(n+1)s^1$, should be constructed and implemented. With it, the band shown in

Figures 4.11 - 4.13, which width represents the uncertainty in the current simulations, would become thinner. This work is already scheduled in collaboration with R. Veenhof (the creator of Garfield), S. Biagi (the creator of Magboltz) and A. Buzulutskov (who measured experimentally the yield for argon).

4.7 Discussion

With the C++ toolkit developed with basis in Garfield and Magboltz 8.9.5 it is possible to obtain extensive information about the excitations happening due to electron impact in pure noble gases. In this Chapter, the toolkit was applied considering a uniform electric field, a geometry that, due to its simplicity, allows to assess important intrinsic properties of EL which lead to a better understanding of this process.

Properties related with the drift of electrons process itself were evaluated and presented, as the collision rates of each level/group and the kinetic energy distribution. It was confirmed that the four states which are part of the $np^5(n+1)s^1$ electronic shell configuration are the most frequently produced, in accordance with reference [95].

Assuming that every excited atom leads ultimately to the emission of one VUV photon it was possible to calculate the VUV electroluminescence efficiency. It is, under optimal conditions, higher than 70 % for all gases meaning that a big fraction of the energy supplied to the electrons is converted into VUV light.

As a consequence of the efficient conversion of electron kinetic energy into VUV photons, pure noble gases present high values of VUV EL yield. This quantity was calculated as a function of the applied electric field and a very good overall agreement with earlier Monte Carlo simulations [109] and measurements [68, 67] was obtained for argon and xenon. This agreement worked as a validation for the toolkit indicating that it can be applied to other geometries.

The statistical fluctuations associated to VUV EL were also calculated as functions of the electric field. It was found that, after the VUV EL threshold, they decrease as the field increases until the ionization onset, for which the fluctuations in the secondary charge production start to dominate. It was also confirmed that the statistical fluctuations associated to proportional VUV EL are lower than those in both charge avalanche multiplication and primary electron cloud formation. To the best of the author knowledge, up to now, there were not consistent values for J_{VUV} published in literature, being thus the first time that these parameters are presented for the studied gases.

A first attempt was also made in order to simulate the electroluminescence in the Vis-IR range in argon and xenon. Two approaches were considered: one considering

that only $np^5(n+1)p^1$ levels give rise to Vis-IR photons; and the other considering that any level in a shell configuration different of $np^5(n+1)s^1$ produce ultimately a Vis-IR photon. It was found that the measured curve of the reduced Vis-IR yield as a function of the field, reported in reference [117], is between the curves given by the considered two approaches. This states a starting point for the accurate simulation of Vis-IR light emitted by noble gases. Although, further work is needed in order to improve the model of decays between the different levels / configurations higher than $np^5(n+1)s^1$. The use of Vis-IR EL can be specially interesting for detectors operating in avalanche regimes in which the fraction of produced excited levels through electron impact giving rise to the production of Vis-IR photons is high.

CHAPTER 5

VUV EL in a cylindrical geometry

The construction of the common used uniform electric field gaps for EL production in SDCs (introduced in Section 1.3.2.2) is difficult due to mechanical constraints. Once electrical potentials are applied, electrostatic forces are generated and the electrodes (usually metallic meshes) are deformed. In order to ensure that a high fraction of the volume between the meshes is under the influence of an electric field, as uniform as possible, the EL gaps tend to be wide. At high pressures, the use of wide gaps implies high voltages in order to achieve the optimal operational fields. To overcome these problems, in reference [135] D. Nygren has proposed an alternative field geometry for EL production in SDCs, based in the MWPC and consisting of a plane of parallel wires. Such detector was proposed to operate with electric fields below the ionization threshold of the gas, which implies the use of much lower voltages than in a parallel geometry but in principle still producing enough EL photons. Each of the wires would run as an individual cylindrical GSPC (see Section 1.3.2.1).

The C++ simulation toolkit, presented in Chapter 3 and validated as described in Chapter 4, was used to estimate the properties of VUV EL produced in such proposed geometry. As an initial approximation, it was simulated the EL produced in a cylindrical GSPC, filled with pure xenon, which allows fast simulations and extrapolation for a plane of wires.

5.1 Simulation details

The simulated setup consists of a cylindrical volume delimited by a metallic tube with a diameter of $d_t = 6.0$ cm and a length of 2.0 m, working as cathode. Inside the tube, a wire is aligned with the axis of the tube (which coincides with the zz' axis). The diameter of the wire, d_w , was varied between 0.1 mm and 1.0 mm. The origin of the position frame is at halfway between the ends of the wire. The tube is grounded and a voltage V is applied to the anode in such a way that electrons drift towards the anode. The schematics of the simulated geometry is presented in Figure 5.1.

In such geometry, the intensity of the electric field increases from the cathode to the anode, according to Equation (1.17). Thus, the starting point of each primary electron, $(0, y_s, 0)$, was calculated as a function of the pressure p , the wire and tube diameters, and the applied voltage, so that the electron starts 1 mm outwards the EL region. This region consists of the coaxial volume between the surface of the wire and the cylindrical surface for which the VUV EL threshold of xenon, $(\frac{E}{N})_{VUV}^{thr} \sim 3$ Td (see Section 4.5.2), is attained. It was used xenon at a temperature of 293 K and pressures of 1 and 10 bar. The starting energy of electrons was sampled randomly according to the energy distribution given by Magboltz 8.9.5 for $(\frac{E}{N})_{VUV}^{thr}$ and the starting direction

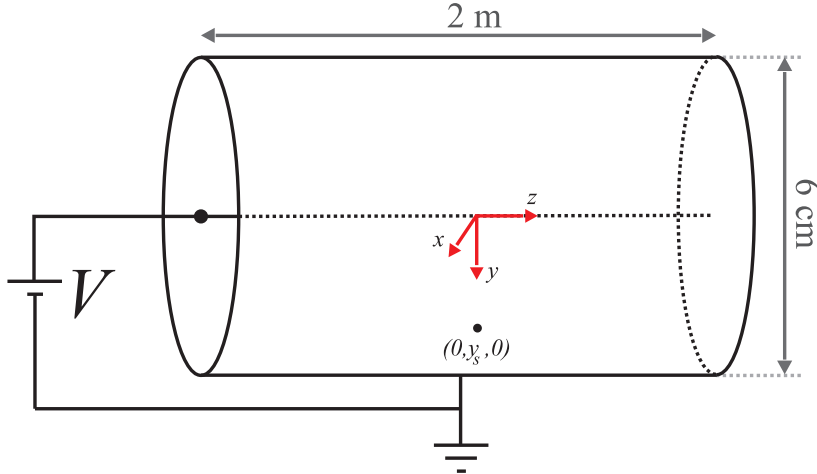


Figure 5.1: Schematics of the simulated cylindrical geometry. The wire diameter is 6.0 cm and its length is 2.0 m. The starting point of each primary electron, $(0, y_s, 0)$, was calculated so that the electron starts 1 mm outwards the EL region.

of each primary electron was sampled isotropically.

5.2 EL Yield

The number of VUV photons produced per primary electron – the total electroluminescence yield, \bar{N}_{VUV} – as a function of the potential applied between the anode and the cathode is shown in Figure 5.2a) and Figure 5.2b) for xenon at 1 and 10 bar, respectively. Curves for the different wire diameters are shown. The points where the smaller fluctuations in the VUV EL are achieved, before the fluctuations associated with ionizations start to dominate, are also indicated (see also Figure 5.3).

The maximum intensity of the electric field is reached always in the vicinity of the anode wire surface. According to Equation (1.17), this intensity is given by:

$$E_{\max} = \frac{V}{\frac{d_w}{2} \ln \left(\frac{d_t}{d_w} \right)} \quad (5.1)$$

For a given voltage, the value of E_{\max} decreases with the increasing wire diameter, d_w . The electrons are therefore less accelerated, reaching less kinetic energy and producing less excitations. Thus, the VUV yield achieved for a given voltage and pressure decreases with the increase of wire diameter.

The VUV yield that can be reached before the worsening of the fluctuations due to ionizations increases as d_w increases. In order to understand this behavior, let's consider an initial situation where the value of the field near the anode is equal to

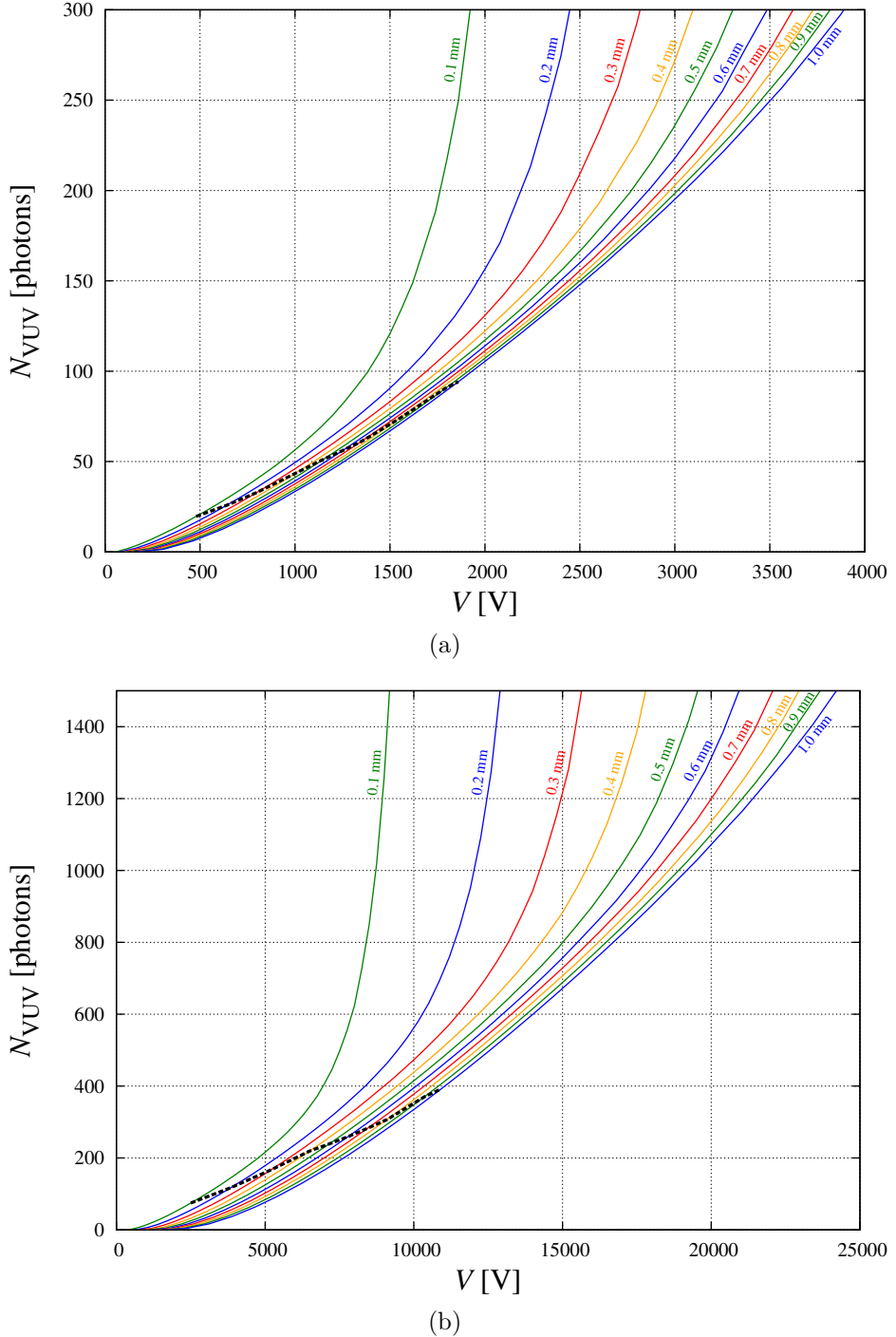


Figure 5.2: Average number of VUV photons produced per primary electron, \bar{N}_{VUV} , as a function of the applied potential, V , for different wire diameters (indicated in the labels near each curve). The tube diameter is $d_t = 60$ mm in all the cases. The black dashed lines connect points where, for each wire diameter, the minimum J_{VUV} is achieved (see Figures 5.3a) and 5.3b)). The xenon temperature is 293 K in both cases and the pressure is 1 bar in Figure 5.2a) and 10 bar in the case of Figure 5.2b).

the ionization onset. Keeping the same voltage, if the wire diameter is increased, E_{\max} decreases. However, the field corresponding to the ionization onset can be again achieved near the surface of the anode, by increasing the applied potential. The increase in the potential means that each primary electron produces excitations over a longer distance, since the field threshold for excitations, $E_{\text{exc}}^{\text{thr}}$, is reached for a farther distance from the center of the wire:

$$r_{\text{exc}}^{\text{thr}} = \frac{V}{\ln\left(\frac{d_t}{d_w}\right) E_{\text{exc}}^{\text{thr}}} \quad (5.2)$$

Thus, the total number of excitations produced for the lowest fluctuations increases with d_w , although higher voltages need to be applied.

Comparing the curves obtained for different pressures, it appears that the achievable yield with low associated fluctuations increases with pressure. The electrons produce excitations over the same path but in a gas with higher densities thus, the total probability of excitations increases. However, higher voltages need to be used in order to create the same reduced electric fields, $\left(\frac{E}{p}\right)$.

5.3 Fluctuations

In Figures 5.3a) and 5.3b) it is shown the simulated values of J_{VUV} , which describes the fluctuations in the VUV EL, for the considered cylindrical geometry at 1 and 10 bar, respectively. The fluctuations are presented as functions of the applied voltage and for different values of the wire diameter. Similarly to what happens in the case of a uniform electric field (see Section 4.5.3), as the voltage increases, J_{VUV} decreases until fluctuations due to the production of secondary charges start to dominate. Values smaller than the Fano factor, although not so low as in a uniform geometry, are achieved for optimal voltages that increase with the wire diameter.

The lowest fluctuations that can be achieved depend slightly on the wire diameter getting worse as the diameter increases, as can be seen from the black dashed line shown in both plots. This line connects points where, for each wire diameter, the minimum value of J_{VUV} was achieved. This behavior, in a first analysis, seems to contradict the increase of the VUV total yield (achievable without fluctuations associated to ionizations) with increasing values of the wire diameter, as explained in the previous Section. This effect needs further clarification and efforts are currently being done in order to find the correct explanation.

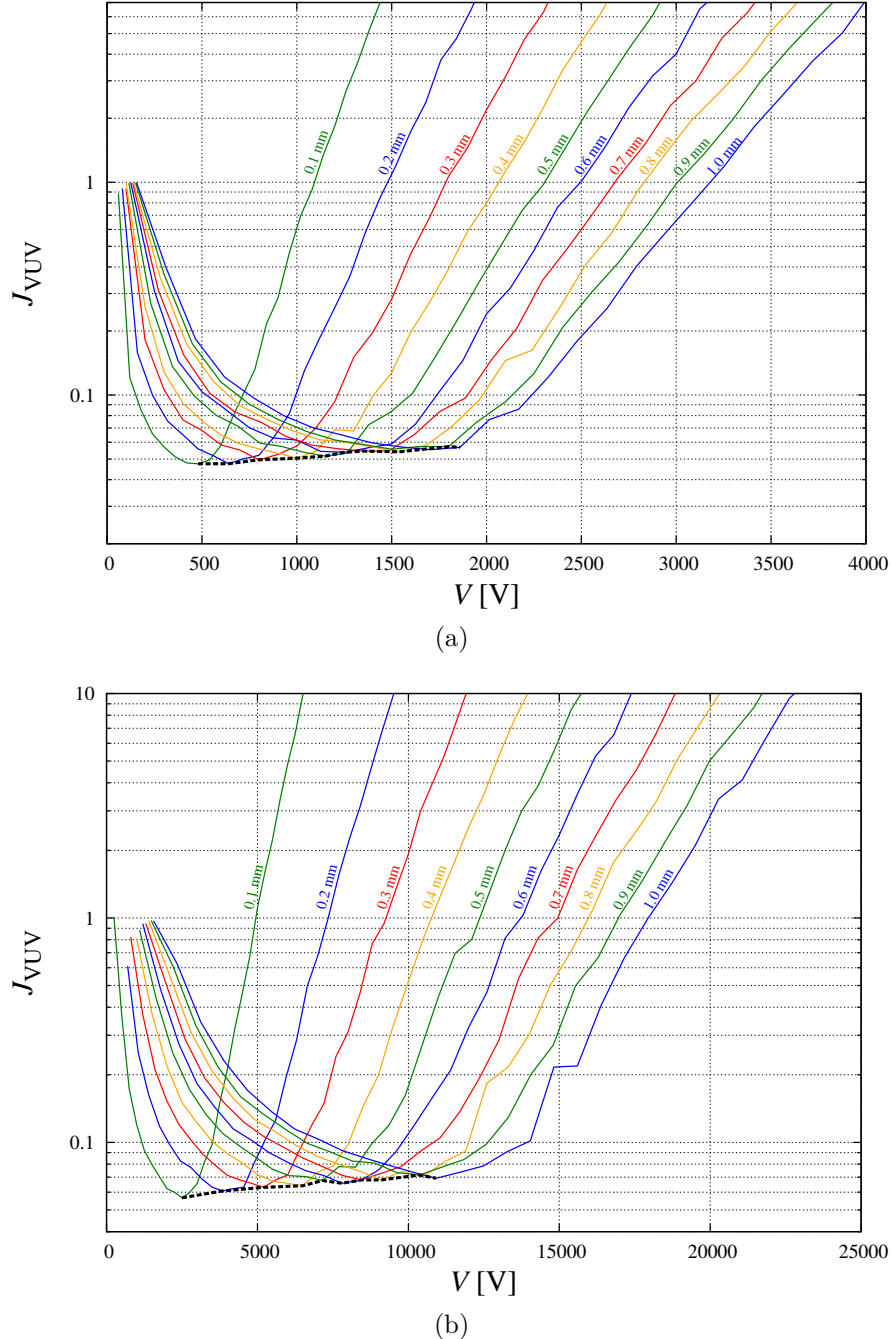


Figure 5.3: Fluctuations associated with VUV EL produced in a cylindrical geometry, described by the parameter J_{VUV} , as a function of the applied potential, V . Curves for different wire diameters (indicated in the labels near each curve) are shown. The tube diameter is $d_t = 60$ mm in all the cases. The black dashed lines connect points where, for each wire diameter, the minimum value of J_{VUV} is achieved. The xenon temperature is 293 K in both cases and the pressure is 1 bar in the case of Figure 5.3a) and 10 bar in the case of Figure 5.3b).

5.4 Spatial distribution of excitations

Figures 5.4 and 5.5 show the distribution of the planar position, (x, y) , where excitations occurred, for xenon at 1 bar and 10 bar, respectively. Results for some of the simulated wire diameters are presented. The wire is represented, in each plot, by a gray circle and the region within which 95 % of the excitations happened is surrounded by a black circumference. The distributions are shown, for each wire diameter, considering the voltage for which the minimum value of J_{VUV} was achieved (see Figures 5.3a) and 5.3b) for 1 bar and 10 bar, respectively).

All the distributions show that the excitations, and thus also the emission of VUV photons, occur in a very confined region in the vicinity of the wire, predominantly on the side of the wire where the primary electrons came from. Considering the same pressure, as the wire diameter decreases, its dimensions approach progressively the free path of electrons and thus, the distribution surrounds a higher fraction of the wire perimeter.

By comparing the distributions obtained for the same wire diameter but for the different pressures, it is possible to conclude that the projection into the transversal direction (xx' axis) is thinner for higher pressures. As the pressure increases, the number of collisions per unit of electron path length also increases due to the higher atomic density. A higher number of collisions means that the electron loses more energy for the same traveled distance and has a higher tendency to follow the electric field lines, i. e., the transversal diffusion is lower.

5.5 Discussion

The C++ simulation toolkit, presented in Chapter 3, was used to estimate the total yield and associated fluctuations of VUV EL produced in a simple cylindrical geometry, consisting of a cylindrical wire inside and aligned with the longitudinal axis of a metallic tube.

It was found that the VUV EL yield that can be reached before the worsening of the fluctuations due to avalanche multiplication is higher for wider wires and higher gas pressures. The lowest achievable EL fluctuations worsen with the increase of the wire diameter.

The spatial distributions of the excitations were also evaluated, suggesting that the emission of VUV EL photons is confined to the vicinity of each wire and happen predominantly on the side of the wire where the primary electrons came from.

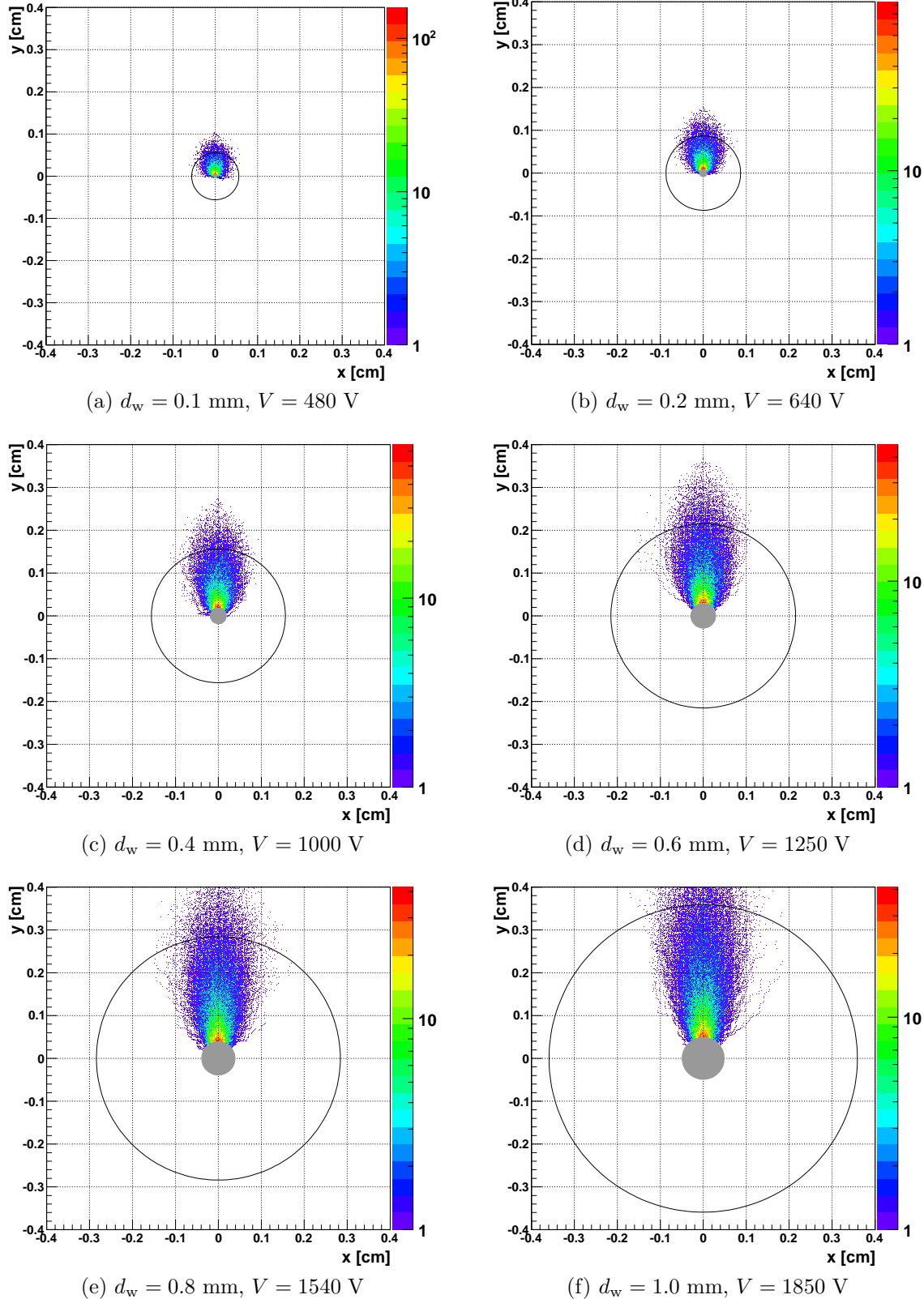


Figure 5.4: Spatial 2D distribution of excitations produced by 1,000 primary electrons, for different wire diameters (illustrated with a gray circle). The voltage that minimizes J_{VUV} is considered (see Figure 5.3a)). The tube diameter is 60 mm in all the cases. Xenon at 293 K and 1 bar is used. Black circumferences surround the region within which 95 % of the excitations happen.

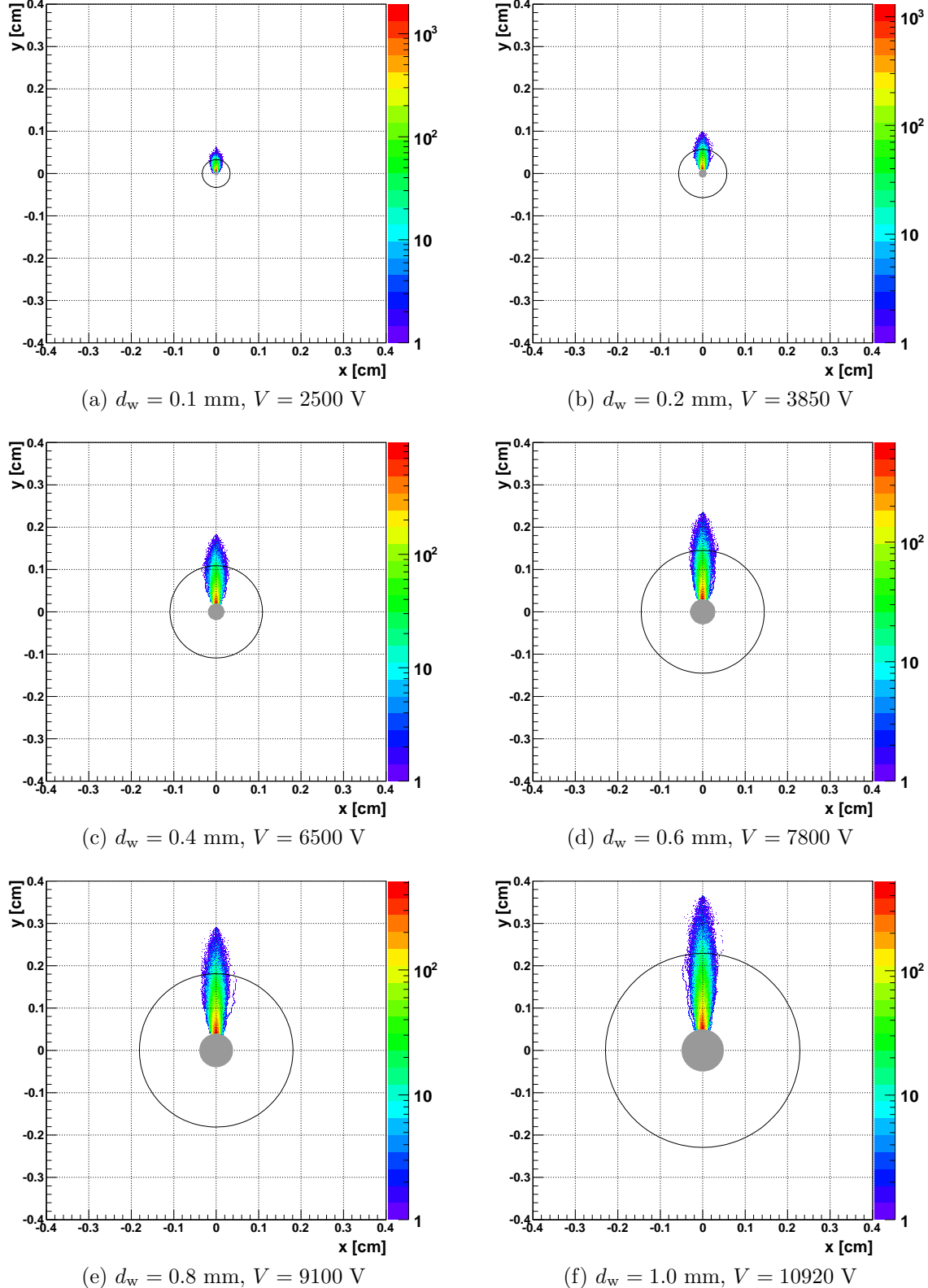


Figure 5.5: Spatial 2D distribution of excitations produced by 1,000 primary electrons, for different wire diameters (illustrated with gray circles). The voltage that minimizes J_{VUV} is considered (see Figure 5.3b)). The tube diameter is 60 mm in all the cases. Xenon at 293 K and 10 bar is used. Black circumferences surround the region within which 95 % of the excitations happen.

CHAPTER 6

VUV EL in MPGDs

In the Section 1.3.3.3 of this document, it was presented the PACEM as a device with IBF suppression capabilities. This device is appropriate for GPMs with sensitivity in the visible spectral range since ions, flowing back to the photocathode, cause its aging and can induce undesirable secondary photoelectron emissions. The PACEM is also suitable for TPC readouts, avoiding space charge distortions of the drift electric field. The principle of operation is the opto-coupling between two charge multipliers (MPGDs), achieved by taking advantage of the VUV EL produced during the avalanche development in the first amplification stage. The concept can be implemented in many configurations making use of different microstructures.

Cryogenic noble gas dual-phase liquid/gas detectors have been or are being developed for direct detection of WIMPS (Dark Matter candidates) [1, 2, 3, 4]. These particles are expected to interact with the nuclei of the liquid phase of such detectors producing both primary scintillation and primary ionization. The resulting electrons are extracted to the gaseous phase and their signal is amplified. The ratio between the primary ionization and the primary scintillation signals is a unique signature of each type of particle that can be used to separate the rare WIMP events from the background. The simplicity, low cost, radiation hardness and the possibility of constructing large areas, make MPGDs good candidates for the amplification of the primary ionization signal [136, 137]. However, in these experiments, it is of major importance to have the highest possible gain in order to efficiently discriminate the Dark Matter events. The use of the charge signal produced in MPGDs is thus not suitable for such applications since the charge gain of these devices, working at cryogenic temperatures is low. Thus, the use of the VUV EL signal produced during the avalanches undergone by primary electrons in these microstructures appears as a good alternative. It represents also a good alternative to the commonly used parallel gaps for EL production since high light gains can be achieved by using much lower voltages.

In order to assess the feasibility of the use of VUV EL produced in MPGDs for the applications mentioned in the previous lines, it is of major interest to determine its properties, specially its total EL yield. In this Chapter the light responses of the GEM and MHSP are simulated and studied in detail using the C++ toolkit. The obtained EL yields are compared with recent measurements published in reference [138].

6.1 Electric field maps

Electric fields present in microstructures like GEM and MHSP can not be determined analytically due to their complex shape and the presence of insulators. Thus, in order to perform the simulations, field maps were constructed using Ansys12® [139], which

calculates the electric potential in the nodes of a mesh, by using the Finite Element Method (FEM) [140]. The electric field vector in any point can then be calculated through interpolation. The *3-D 10-Node Tetrahedral Electrostatic Solid* finite element was used since it is suitable for modeling irregular meshes that need to adapt to curved edges. This finite element consists of a tetrahedron with curved edges and 10 nodes (4 in each of the vertices and 6 in the middle of each edge). The use of 10 nodes allows a second order polynomial interpolation for the electric potential as a function of each of the cartesian coordinates. Polynomials are not solutions of the Maxwell equations and, although the electric potential is constrained to be continuous in the border of elements, the electric field (being the gradient of the potential) is discontinuous having a linear dependence on x , y and z inside each element [141]. This represents the main limitation of the FEM method that usually gives poor precision in field calculations. However, at the time that the simulations were performed, the C++ toolkit didn't have interface to any other field calculation method, as e.g the recently developed *nearly exact Boundary Element Method* that uses Green's functions, that are solutions of the Maxwell equations [121].

Since the hole and electrode patterns of the GEM and MHSP are periodic, unitary cells were constructed being the longitudinal axis of the holes parallel to the zz' axis. Mirror symmetries applied in the xx' and yy' directions were used, creating maps of ideal microstructures with infinite areas. These unitary cells will be presented later when describing the simulation details for each of the simulated microstructures.

6.2 GEM

6.2.1 Simulation details

A standard GEM was considered, consisting of a $50\ \mu\text{m}$ thickness Kapton[®] foil covered with $5\ \mu\text{m}$ thickness copper layers on both sides and perforated with bi-conical holes of 50 and $70\ \mu\text{m}$ diameter at the inner and outer apertures respectively, arranged in a regular hexagonal layout with an edge of $140\ \mu\text{m}$. The considered unitary cell is represented in Figure 6.1b).

In reference [138], the primary charge was generated using a collimated $22.1\ \text{keV}$ X-ray beam and the VUV EL photons were measured by a LAAPD placed below the GEM. The drift and induction fields were 0.5 and $-0.1\ \text{kVcm}^{-1}$ respectively (the experimental setup is depicted in Figure 6.1a)). The unusual reversed induction field was used experimentally so that no charge readout below the GEM was needed and that the LAAPD could replace it. This experimental field setup was implemented in the field map calculations performed in the simulations.

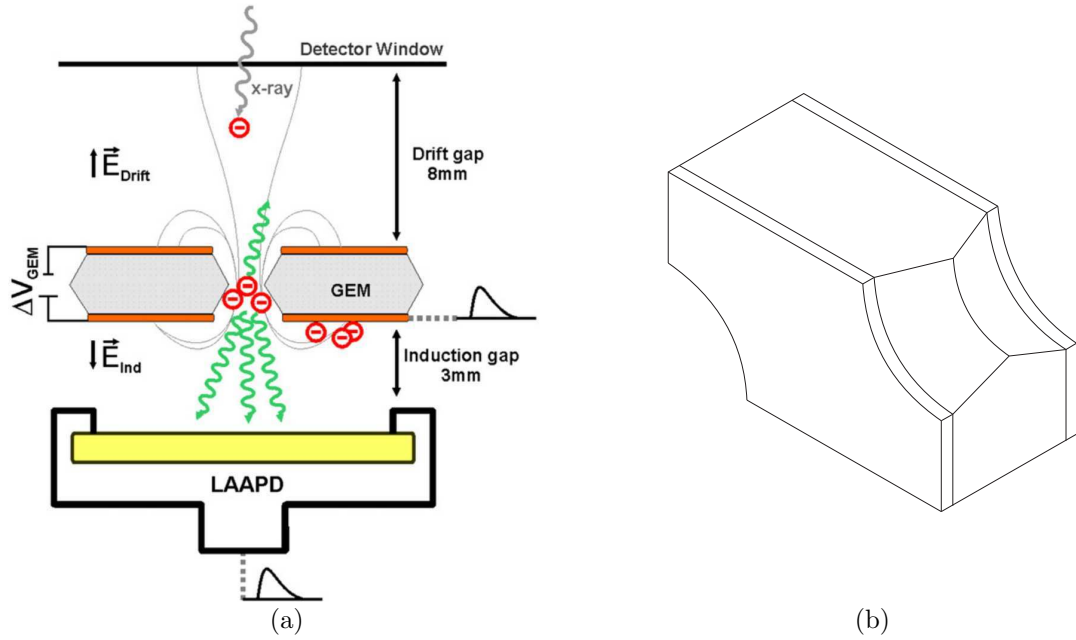


Figure 6.1: a) Experimental setup used in the GEM EL yield measurements of reference [138] and simulated in this work. b) Unitary cell used in the field map calculations performed with Ansys12®.

The primary electrons were released isotropically $250 \mu\text{m}$ above the GEM (measured in the zz' direction), in a region where the equipotential surfaces are completely flat and the electric field is uniform. The (x, y) coordinates of the starting point were sampled randomly according to an uniform distribution along the area equivalent to the unitary cell. Each electron started with a kinetic energy sampled randomly according to the energy distribution given by Magboltz for the drift field. A set of 500 primary electrons was simulated in order to obtain an error in the yield bellow 10 %. Pure xenon at 300 K and pressures of 1.0, 1.5 and 2.5 bar was used.

6.2.2 VUV EL yield

The calculated total VUV EL yield is shown in Figure 6.2 as a function of the potential applied between the top and the bottom electrodes of the GEM, V_{GEM} . Results for the different simulated pressures are compared with those of the measurements reported in reference [138]. For a given pressure, the simulated yield has the typical exponential dependence with V_{GEM} . As the pressure increases, the voltages needed to obtain the same yield increase. This results from the decrease of the mean free path of electrons with the increase of pressure due to the higher atomic density. Electrons travel a shorter distance between collisions and are less accelerated, achieving lower kinetic energies, an effect that can be compensated by the increase of the applied voltage. The maximum

value of this voltage is limited experimentally due to discharges that can happen since the distances between electrodes are very small.

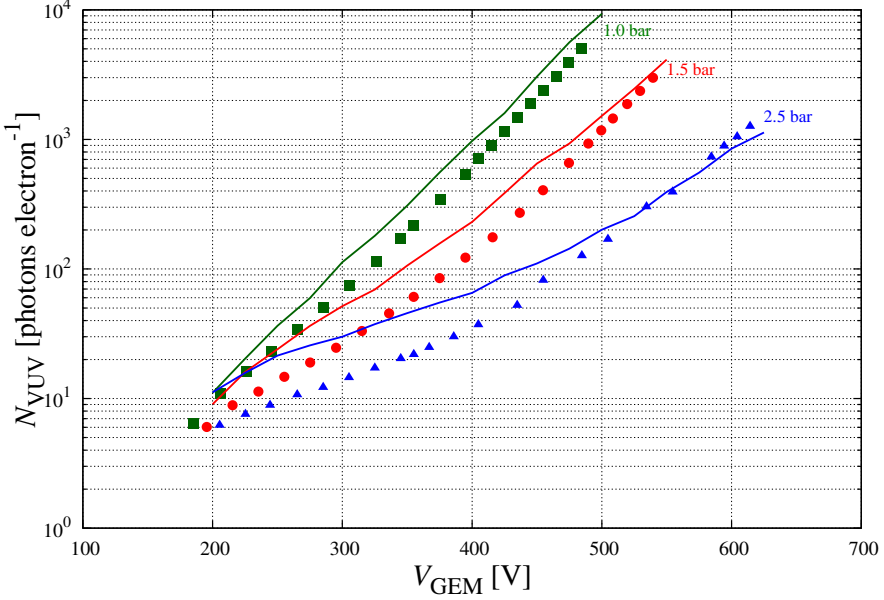


Figure 6.2: Average number of VUV photons produced per primary electron, \bar{N}_{VUV} , as a function of the potential applied between the top and the bottom electrodes of the GEM, V_{GEM} , shown for different pressures of xenon at 300 K. The simulated results (lines) are compared with the total VUV EL yield measured in [138] (filled symbols).

Specially for high voltages, the simulated VUV EL yield approaches the experimental results (which have an associated uncertainty of the order of 20 %). However, some differences between the data are present.

Micro-pattern structures are difficult to construct and, although devices with good performances can be obtained with careful methodology, it is not guaranteed that the shape of the insulator and electrode parts are exactly as projected. Namely, the shaping of the bi-conical holes and of the sharp electrode's edges are the most challenging tasks. Thus, the differences between the simulated and measured yields can be associated with imperfections introduced during the construction of the GEM relative to the projected shape, specially for high gains (higher voltages).

During a charge avalanche developed in a MPGD that includes an insulator, electrons and ions can end their track on the insulator surface and accumulate. The accumulated charges can distort the electric field and thus, change the VUV EL yield. This is the so-called *charging-up* effect that can play some role and was not considered in the simulations. Currently, efforts are being done in order to assess the contribution of it in the calculations, by constructing field maps iteratively and taking into account the deposited charge between iterations.

The uncertainties associated with the FEM method can also have some contribution to the disagreement due to the discontinuous nature of the generated electric field, as described in Section 6.1.

6.2.3 Spatial distribution of excitations

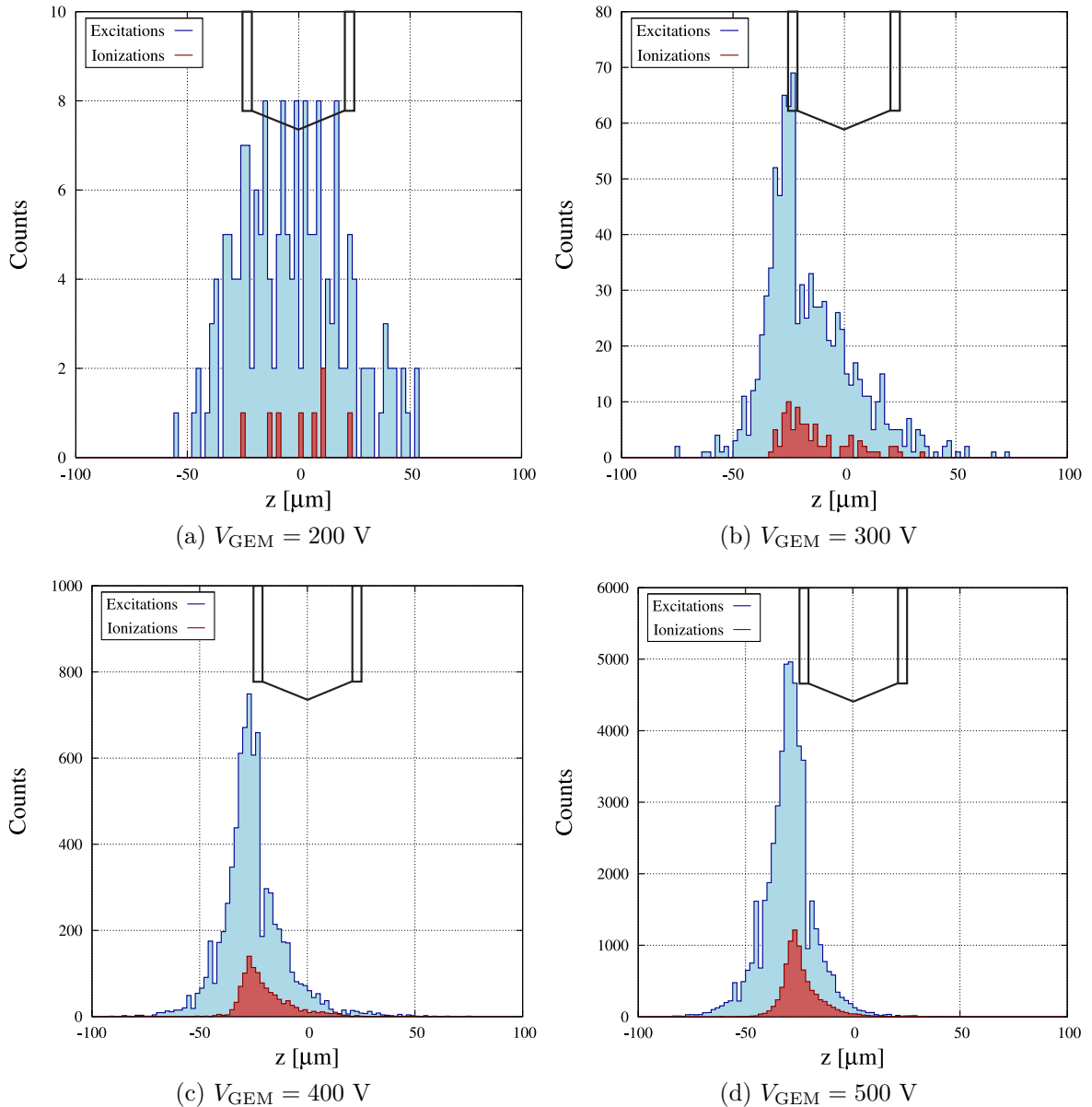


Figure 6.3: Distribution of the z coordinate of the points where excitations and ionizations occurred, shown for some voltages applied along the GEM's holes. For each case, a set of 10 primary electrons was simulated for xenon at 1.0 bar and 300 K. The edges of the microstructure are proportionally represented at each plot. The electrons enter the GEM hole for positive values of z and drift toward negative values.

In Figure 6.2 it is possible to observe that the disagreement between the simulated and the experimental VUV yield is higher for lower voltages. In the experimental setup [138], it is not possible to record all the VUV photons. The LAAPD has a subtended solid angle that need to be considered in the calibrations.

The plots of Figure 6.3 show the distribution of the z coordinate of the points where excitations occurred, for some applied potentials and for xenon at 1.0 bar and 300 K. In the same plots, it is included the z distribution of the ionization points.

For low voltages, the number of produced secondary charges is low (this can also be observed in Figure 6.4) and the microstructure works almost only in EL mode. The regions where more atoms are excited reflect the volumes where higher electric fields exist. The fraction of excitations and thus, of VUV photons emitted in the upper half part of the holes is roughly the same as that in the lower half part. As the applied voltage increases, the size of the avalanche increases and, due to its cascade nature, a high fraction of secondary electrons is created in its last stage (below the bottom electrode). These secondary charges also excite atoms and thus induce the emission of VUV photons. The fraction of photons emitted in the upper half part of the holes is now much lower than that of photons originated in the lower half part.

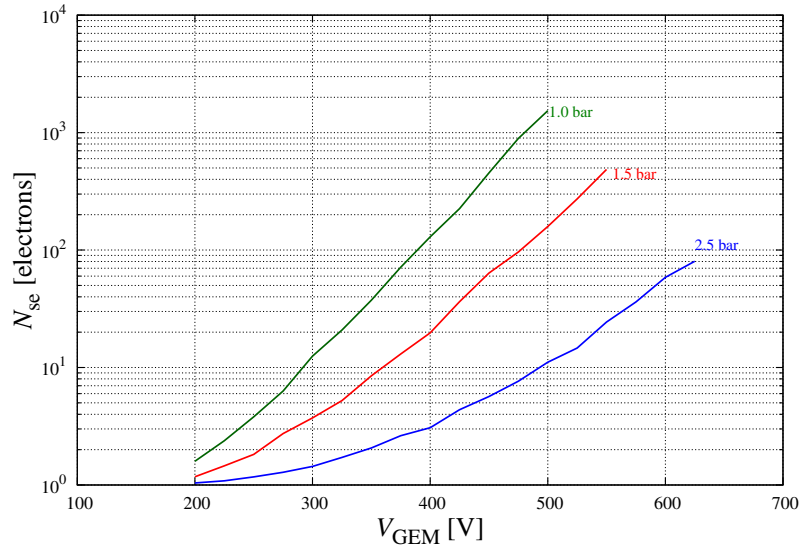


Figure 6.4: Average number of secondary electrons produced per primary electron (including the latter), \bar{N}_{se} , as a function of the potential applied between the top and the bottom electrodes of the GEM, V_{GEM} , shown for different pressures of xenon at 300 K.

The previous analysis allows the conclusion that the solid angle subtended by the LAAPD is dependent on the VUV EL yield. The experimental calibration was made considering the same subtended solid angle for all the conditions, giving more importance to photons produced in the lower half part of the holes, which is appropriated

only for high VUV EL yields. Thus, for lower voltages, the measured total yield is underestimated since the GEM itself blocks a big fraction of photons from the upper half part.

6.2.4 Number of VUV photons vs number of electrons

The distributions presented in Figure 6.3 show that, in a GEM, the number of excitations produced in the avalanches is much higher than the number of ionizations. The ratio between these two numbers is shown, as a function of the voltage applied to the GEM and for the different simulated xenon pressures, in Figure 6.5.

For the same value of V_{GEM} , as higher pressures are considered, the maximum energy acquired by electrons between collisions decreases, since their free path is lower. Since the energy threshold for ionizations is higher than for excitations, the latter are more likely for higher pressures. Considering the same pressure and starting with low voltages ($V = 200$ V), the ratio initially grows since the electric field is increasing and the maximum kinetic energy reached by the electrons is enough for excitations but hardly enough for ionizations. For a certain voltage, at some of the collisions, electrons can achieve an energy slightly higher than the ionization threshold. At these energies, the ionization cross section is higher than that for excitations, as shown in Figure A.2b), and thus the ratio starts to drop.

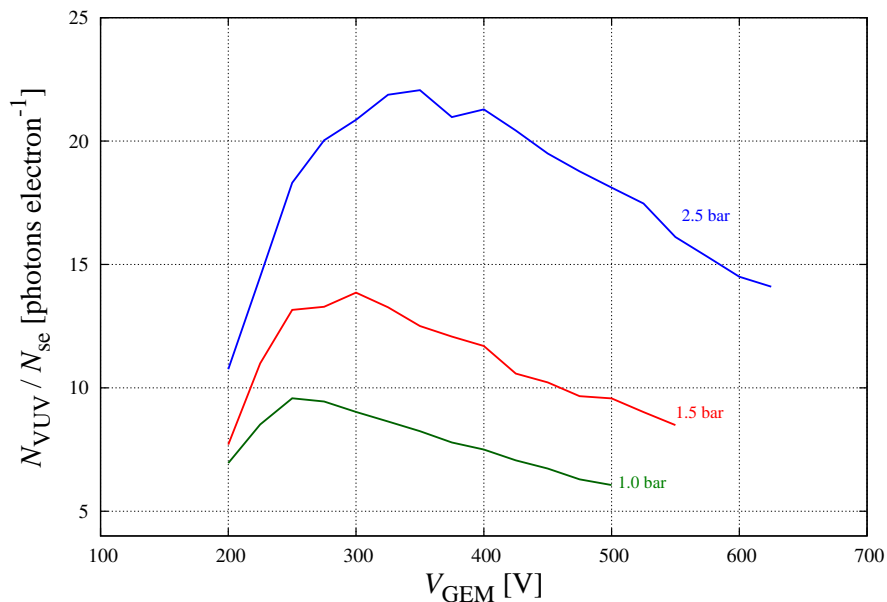


Figure 6.5: Ratio between the number of excitations and the number of ionizations produced during avalanches developed in a GEM, shown as a function of the voltage applied between the top and the bottom electrodes, V_{GEM} , and for different pressures of xenon at 300 K.

6.3 MHSP

6.3.1 Simulation details

A standard MHSP was considered, consisting of a $50\ \mu\text{m}$ thickness Kapton[®] foil covered with $5\ \mu\text{m}$ thickness copper layers on both sides and perforated with bi-conical holes of 50 and $70\ \mu\text{m}$ diameter at the inner and outer apertures respectively, arranged in an hexagonal pattern. The hole-pitch was $200\ \mu\text{m}$ along the xx' direction (perpendicular to the strips) and $140\ \mu\text{m}$ along the yy' direction (parallel to the strips). The width of the cathodes and anodes was 100 and $20\ \mu\text{m}$ respectively. The considered unitary cell is represented in Figure 6.6b).

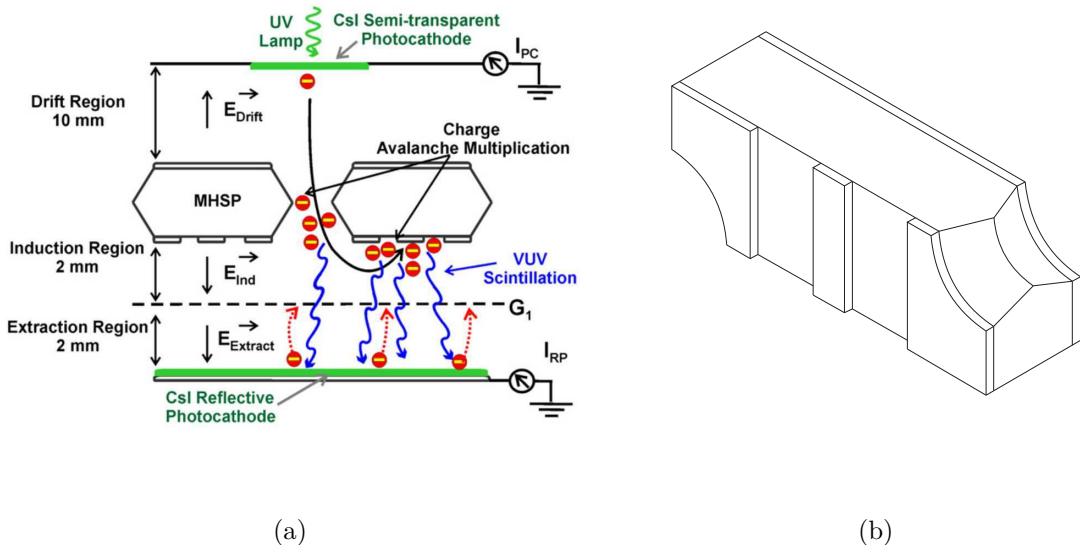


Figure 6.6: a) Experimental setup used in the MHSP EL yield measurements reported in [138] and simulated in this work. b) Unitary cell used in the field map calculations performed with Ansys12[®].

In reference [138], the primary charge was extracted from a semi-transparent CsI photocathode by photons emitted from a UV lamp. The VUV EL photons produced in the avalanches impinged on a reflective CsI photocathode extracting photoelectrons from it that were collected by a metal mesh. The amplitude of the current induced in the mesh by the photoelectrons is proportional to the number of VUV photons emitted during the avalanche. The drift and induction fields were 0.1 and $-0.1\ \text{kVcm}^{-1}$ respectively (the experimental setup is depicted in Figure 6.6a)). This field setup was implemented in the field map calculations.

The primary electrons were released isotropically $250\ \mu\text{m}$ above the MHSP (mea-

sured in the zz' direction), in a region where the equipotential surfaces are completely flat and the electric field is uniform. The (x, y) coordinates of the starting point were sampled randomly according to an uniform distribution along the area equivalent to the unitary cell. Each electron started with a kinetic energy sampled randomly according to the energy distribution given by Magboltz for the drift field. A set of 500 primary electrons was simulated in order to obtain an error in the yield bellow 10 %. Pure xenon at 1.0 bar and 300 K was used.

6.3.2 VUV EL yield

The calculated total VUV EL yield is shown in Figure 6.7 as a function of the total voltage, V_{total} . The latter is the sum of the potential applied between the cathode and the top electrodes, V_{CT} , with the potential applied between the anode and the cathode, V_{AC} . The results are compared with the measurements reported in reference [138]. The experimental and simulated yields obtained for the case of GEM are also included in the plot. The two exponential regimes typical of the MHSP are clearly visible: the first corresponds to the increase on V_{CT} while $V_{\text{AC}} = 0$ V, and the second to an increasing V_{AC} while the value of V_{CT} is kept constant.

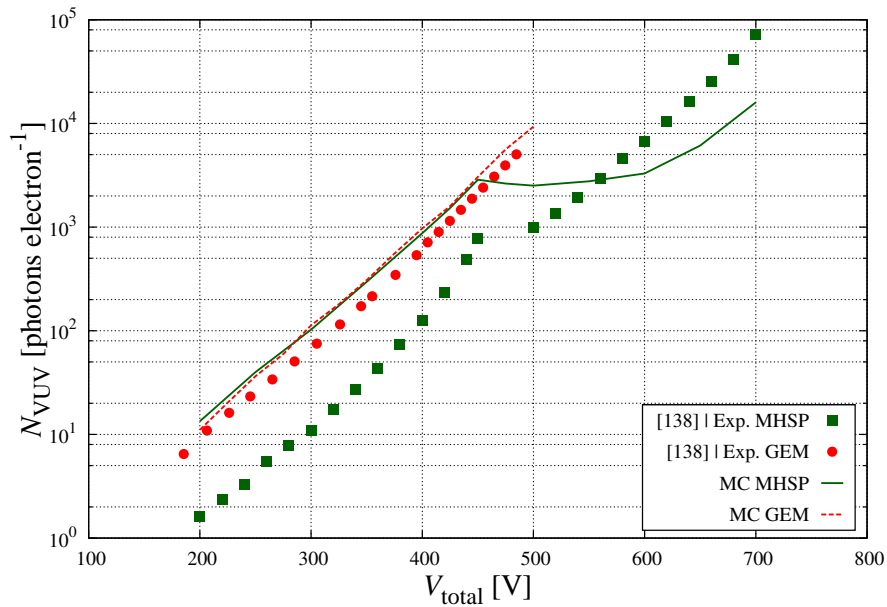


Figure 6.7: Average number of VUV photons produced per primary electron in a MHSP, \bar{N}_{VUV} , as a function of the total applied voltage ($V_{\text{total}} = V_{\text{CT}} + V_{\text{AC}}$). The results are shown for xenon at 1.0 bar and 300 K. Those obtained through the simulation (green line) are compared with the total VUV EL yield reported in [138] (filled squares). The results of simulations and measurements for the case of GEM are also included in the plot.

The absolute value of the VUV EL yield is very different from the one measured

in [138]. However, it is close to the experimental and simulated yields of the GEM (with holes of the same geometry and dimensions), for the points where $V_{AC} = 0$ V (the initial exponential regime). For both the GEM and the MHSP setups, the induction fields have the same orientation and, for $V_{AC} = 0$ V, the higher fields exist inside or in the vicinity of the holes, in both cases. Thus, in this regime, the MHSP yield should indeed be similar to that of the GEM.

In the experimental setup reported in [138], for the case of the MHSP, the gas purification was achieved by diffusion, unlike as in the case of the GEM, for which it was achieved by convection. The xenon purity was thus affected, being possible that the measurement underestimated the VUV EL yield of the MHSP.

As mentioned in the previous section, the building of micro-pattern structures is difficult and the elements of the final devices can have slightly different dimensions than those that were projected. Beyond the possible imperfections introduced in the shape of the holes, the MHSP can present additional imperfections in the anode strips, where a charge multiplication stage occurs and a big fraction of the VUV photons are emitted, as can be observed in Figure 6.8. This can be also a source of the observed disagreement with the experimental data.

The charging-up effect (which was not considered in the simulations) can also play some role. In the case of the MHSP, beyond the hole's surface, the electrons can accumulate in the exposed kapton surface between the cathode and the anode strips.

6.3.3 Spatial distribution of excitations

In Figure 6.8, it is shown the distribution of the (x, z) coordinates of the points where excitations occurred, for $V_{CT} = 450$ V and $V_{AC} = 250$ V (the maximum voltages considered in the simulations). The two regions with higher intensity reflect the two charge multiplication stages, one in the exit of the hole and the other in the vicinity of the anode strips.

6.4 Discussion

In this Chapter the total VUV EL yield of the micro-pattern structures GEM and MHSP working in xenon was estimated. Since, in these cases, the electric field can not be obtained through analytical solutions, the program Ansys12[®], based in the Finite Element Method and interfaced with the C++ toolkit, was used to produce the field maps needed for the tracking of electrons and avalanches.

The simulation toolkit was able to approximately reproduce the experimental measurements performed for the case of the GEM. Some disagreement between the data can

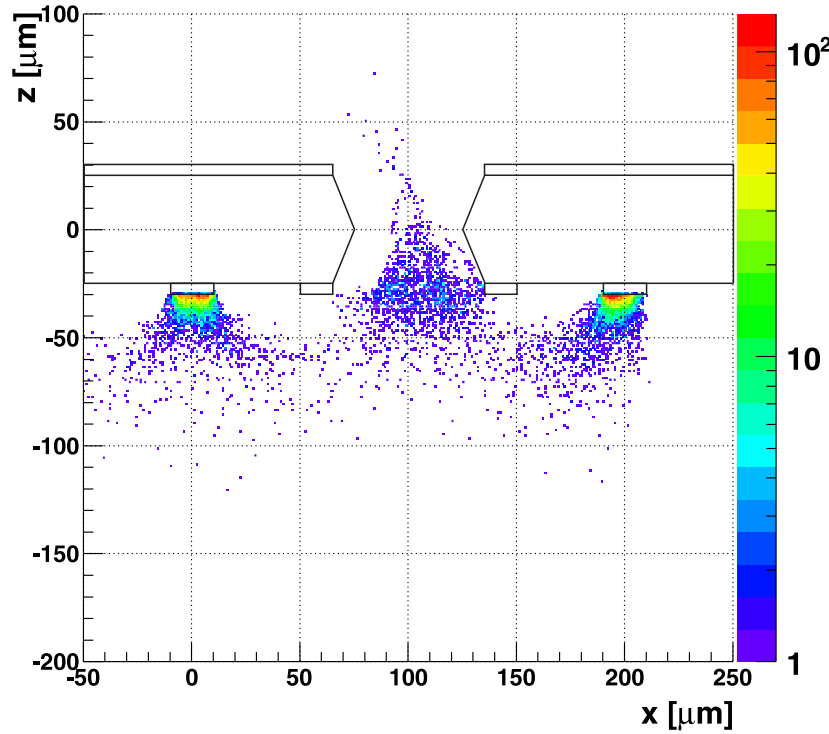


Figure 6.8: Distribution of the (x, z) coordinates of the points where excitations occurred, shown for $V_{CT} = 450$ V and $V_{AC} = 250$ V. The distribution refers to 2 primary electrons undergoing multiplication in a MHSP working with xenon at 1.0 bar and 300 K. The edges of the microstructure are proportionally represented at the same plot.

be attributed to imperfections introduced during the construction of the microstructure, that can have a strong effect in the yield. It was also found that the solid angle subtended by a VUV photodetection device, placed below the GEM, is dependent on the total light gain, since the distribution of the vertical coordinate of the points from where VUV photons are emitted gets more asymmetric as the VUV yield increases. The ratio between the number of VUV photons and the number of produced secondary charges is higher for higher pressures and decreases as the voltage applied along the holes is increased and one enters in the avalanche regimes.

The results obtained for the case of the MHSP are not consistent with measurements, although the typical two exponential regimes are present in the obtained curve. However, the comparison between the experimental yields for GEM and MHSP, when the voltage between the anode and the cathode of the latter is null, are unexpectedly very different. In these conditions, the MHSP can be viewed as working in GEM mode and, since the geometry of the holes is the same in both structures, the VUV EL yields should be similar. The disagreement suggest possible imperfections in the MHSP used in the measurements. It can also be due to the possible experimental underestimation

of the yield, since a gas purification method that does not ensure an extremely low level of impurities was used. This structure has additional possible sources of imperfections due to its more complex shape, relative to the GEM.

CHAPTER 7

NEXT - Neutrino Experiment with a Xenon TPC

7.1 NEXT & $\beta\beta^{0\nu}$ decay searches

During the last decade, different experiments have shown that neutrinos have mass and mix [5]. This opens the possibility for the Majorana nature of these particles. If the neutrino is a Majorana particle then it is its own antiparticle and the neutrino-less double beta decay ($\beta\beta^{0\nu}$), a Standard Model forbidden process, is possible in some isotopes, including ^{136}Xe [6]. Beyond giving an experimental proof of the Majorana nature of neutrinos, the measurement of the half-time of the $\beta\beta^{0\nu}$ decay would allow the determination of the absolute scale of neutrino masses, a demanding and essential task.

The Neutrino Experiment with a Xenon TPC (NEXT) will search for the $\beta\beta^{0\nu}$ decay in ^{136}Xe using a 100 kg, high-pressure gaseous xenon, electrominescent Time Projection Chamber (HPXe TPC). The detector can be considered as a Scintillation Drift Chamber (SDC) according to the description presented in Section 1.3.2.2. The project is approved for operation in the Canfranc Underground Laboratory (LSC), Spain. The TPC will have separated readout systems for calorimetry and tracking to facilitate both measurements (see Figure 7.1).

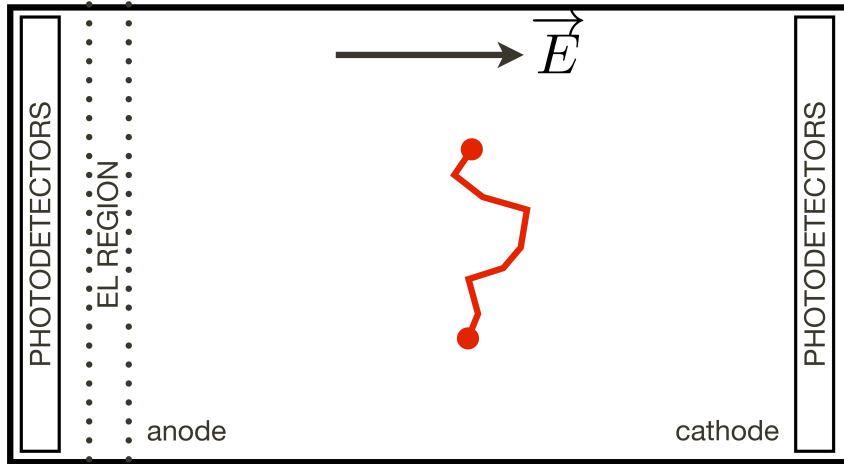


Figure 7.1: Schematic representation of the Neutrino Experiment with a Xenon TPC detector and of the topological signature “spaghetti with two meat balls” of the two electrons emitted by the $\beta\beta^{0\nu}$ decay.

The two electrons emitted by the $\beta\beta^{0\nu}$ decay transfer their energy to the medium through ionizations and excitations of the gas atoms. Due to the dependence of the stopping power of fast electrons on their energy, explained in Section 1.1.2, the topological signature of this decay is similar to a “spaghetti with two meat balls”. The

excitation energy results in the prompt emission of VUV light – primary scintillation. The ionization tracks (positive ions and free electrons) left behind by the two fast electrons are prevented from recombination by a suitable drift electric field. Negative charge carriers – primary electrons – drift toward the TPC anode, entering a region with a more intense electric field created by two parallel meshes separated by a gap of 5 mm width (EL region in Figure 7.1). There, they are accelerated exciting atoms of xenon, which de-excite emitting EL VUV photons, as described in Section 2.3. Therefore, in such an electroluminescent TPC, both the scintillation and ionization processes ultimately produce VUV photons, to be detected by an array of PMTs, located behind the cathode. The detection of the primary scintillation light constitutes the start-of-event, t_0 , whereas the detection of VUV EL by the PMTs provides an energy measurement. Electroluminescent light is used also for tracking, as it is detected by a second array of photosensors (MPPCs in this case) located behind and close to the EL region [10].

The tracking function will allow to highly suppress background events, by recognizing the topological signature of the $\beta\beta^{0\nu}$ decay. In addition, also the energy discrimination will be used for the decay identification. In this context, an outstanding energy resolution (below 1 %) will be needed in order to distinguish the $\beta\beta^{0\nu}$ peak at $Q_{\beta\beta} = 2.458$ MeV [142] from its natural neighbor background peaks, mainly the γ -ray of 2.447 MeV emitted by ^{214}Po after the beta decay of ^{214}Bi (in 1.57 % of the cases). The de-excitation γ -ray of 2.614 MeV emitted by ^{208}Pb after the beta decay of ^{208}Tl is also a source of undesirable events.

In this Chapter, the C++ toolkit is applied to the conditions expected to be used in NEXT in order to determine the best parameters of operation, specially in terms of the applied electric fields. With the calculated VUV yield and the corresponding fluctuations in hands, the energy resolution in the region of interest of the experiment is predicted for two different scenarios in terms of photon detection efficiency: one more optimistic than the other.

7.2 Simulation details

Each primary electron is allowed to drift a distance of $d = 5$ mm under the influence of a uniform electric field. The effect of the field distortion near the meshes is not considered since it has no significant effect [68]. It is assumed that the gas is at a pressure of $p = 10$ bar and at a temperature of 293 K. A set of $N_e = 4 \times 10^4$ primary electrons is simulated for each value of the voltage applied between the parallel planes, V . The starting direction of each primary electron is generated isotropically. The starting energy is generated according to the energy distribution given by Magboltz

for the actual reduced electric field (in pressure units), $\left(\frac{E}{p}\right) = \frac{V}{dp}$ (see Figure 4.2). According to Section 2.3, it is assumed that every excited atom gives rise to the isotropic emission of a VUV photon.

7.3 VUV EL yield

The reduced electroluminescence yield in pressure units, $\left(\frac{Y}{p}\right)$, as a function of the reduced electric field is shown in Figure 7.2. Like the results obtained in Section 4.5, the behaviour of $\left(\frac{Y}{p}\right)$ with $\left(\frac{E}{p}\right)$ is approximately linear even if some ionization occurs. This happens for $\alpha < 0.1 \text{ ions cm}^{-1}$, being α the first Townsend coefficient (see Figure 7.3).

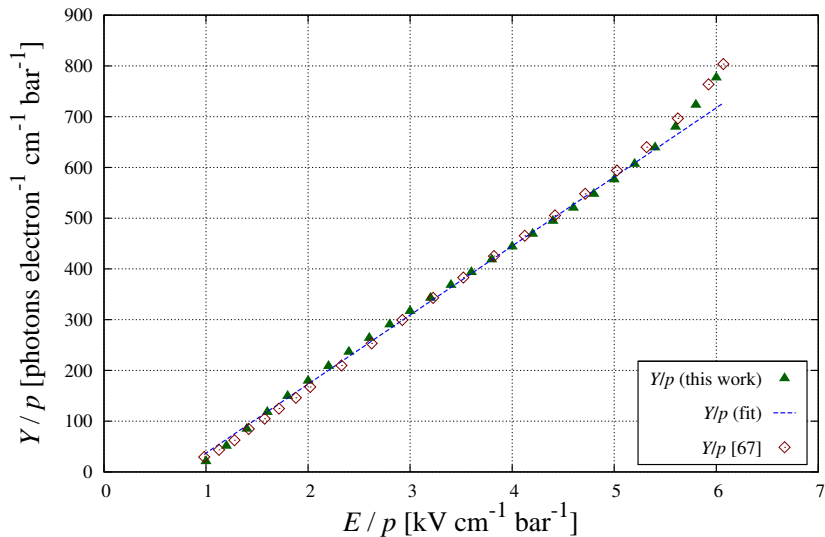


Figure 7.2: Reduced VUV EL yield as a function of the reduced electric field (presented in pressure units). The linear trend of the proportional EL region is represented. Experimental measurements [67] are also shown.

7.4 Fluctuations and energy resolution

As seen in Section 1.4, the FWHM energy resolution of NEXT, an EL based detector using PMTs, is given by:

$$R_E = 2.35 \sqrt{\frac{W}{Q_{\beta\beta}} \left(F + \frac{J}{\bar{N}_{EL}} + \frac{2}{k\bar{N}_{EL}} \right)} \quad (7.1)$$

Using the data obtained through the simulation, the energy resolution which can be achieved by the NEXT detector was estimated. It was assumed that all the energy

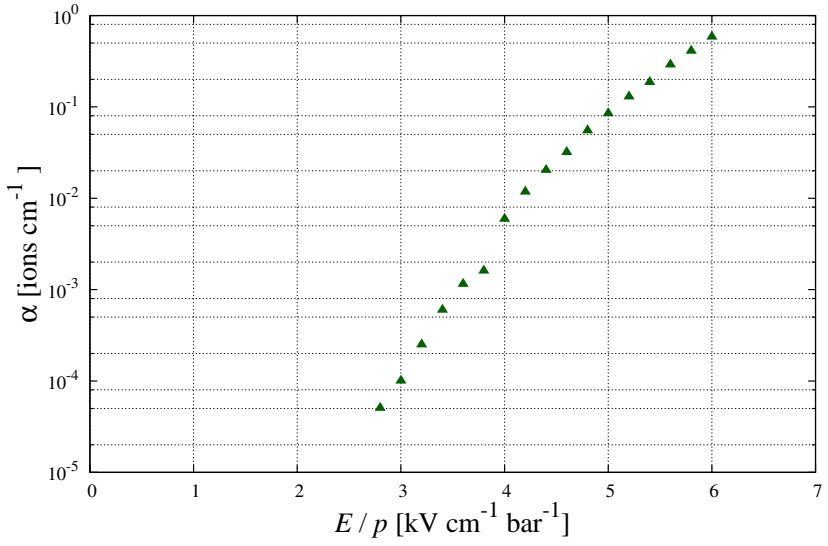


Figure 7.3: Simulated first Townsend coefficient, α , as a function of the reduced electric field.

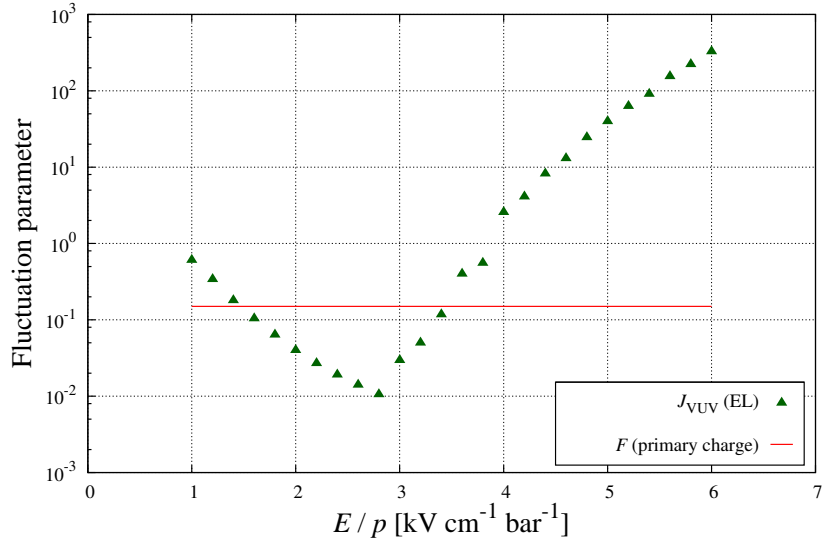


Figure 7.4: Fluctuations in the number of emitted EL photons as a function of the reduced electric field, as described by the parameter J_{VUV} . It is also shown the Fano factor for high pressure xenon.

of the two $\beta\beta^{0\nu}$ decay electrons, $Q_{\beta\beta} = 2.458$ MeV, is deposited in the gas medium, with an average energy lost per ion pair formed of $W = 21.9$ eV [32, 135]. Taking into account the intensity of the electric fields planned to be used, in the drift and in the EL regions, it was assumed that all the primary electrons arrive to the EL region and cross the first mesh without either any recombination or attachment to electronegative contaminants in the drift region. The Fano factor was considered as $F = 0.15$ [135]. In the literature, the reported values are between 0.13 and 0.17 for

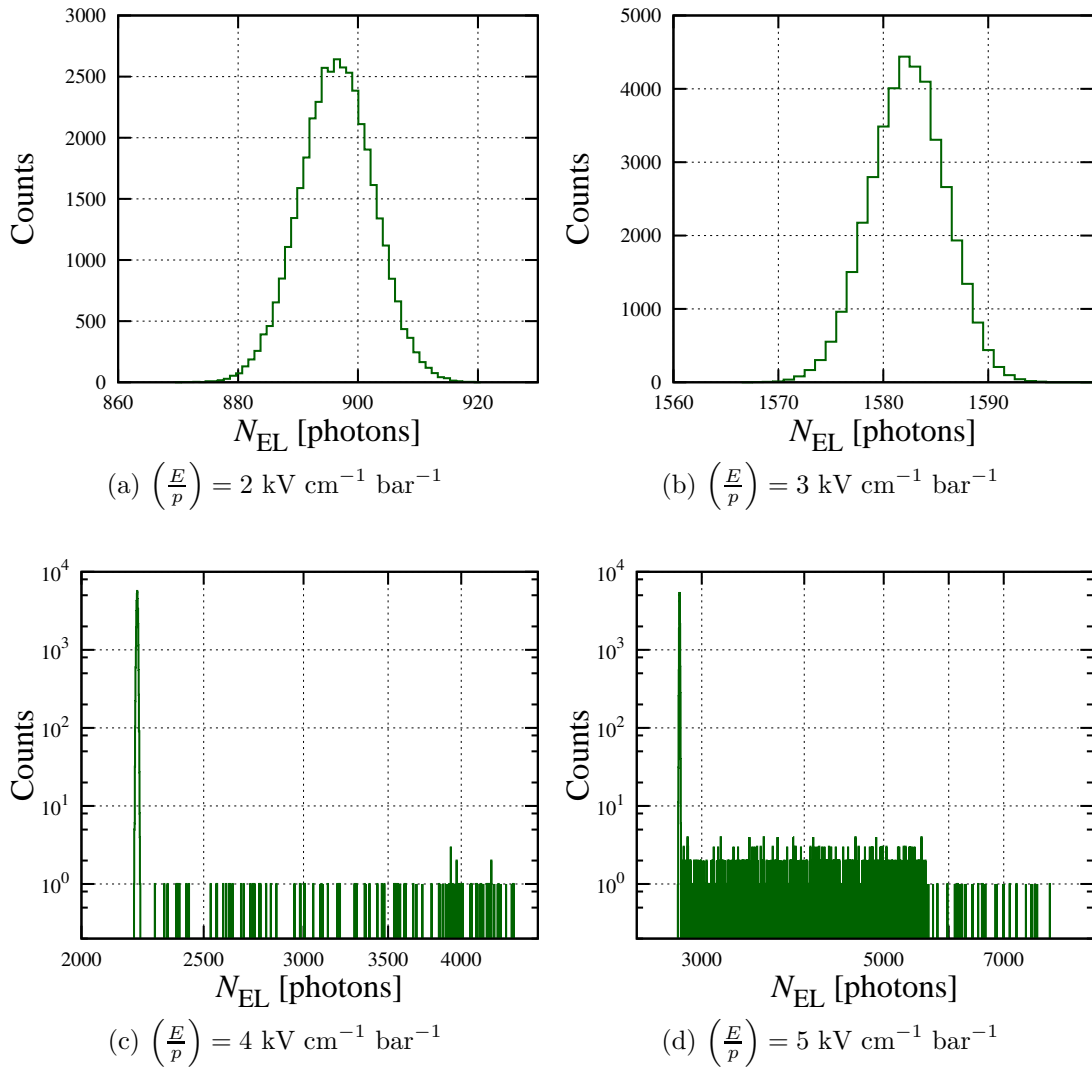


Figure 7.5: Distribution in the number of emitted EL photons per primary electron, N_{EL} , during the drift along $d = 5 \text{ mm}$ of xenon at 10 bar and 293 K, for different values of the reduced electric field.

pure xenon [24, 25, 26, 27, 32] which were used to estimate the overall energy resolution error bars presented in Figure 7.6 and Figure 7.7.

Figure 7.4 shows the VUV EL fluctuations as described by J_{VUV} as a function of the reduced electric field. As the electric field increases, the fluctuations decrease until secondary electrons begin to be produced and the avalanche fluctuations start to dominate. The parameter J_{VUV} is smaller than the Fano factor, in optimal conditions, namely for reduced electric fields between 1.5 and 3.5 $\text{kV cm}^{-1} \text{ bar}^{-1}$. In order to better understand the effect of avalanche fluctuations in VUV EL, Figure 7.5 shows the distributions of the number of VUV photons emitted per primary electron, N_{EL} , for four different values of the reduced electric field. The effect of secondary charges is clearly visible, since a long tail in the distribution appears for higher values of the

electric field (Figures 7.5c) and 7.5d)).

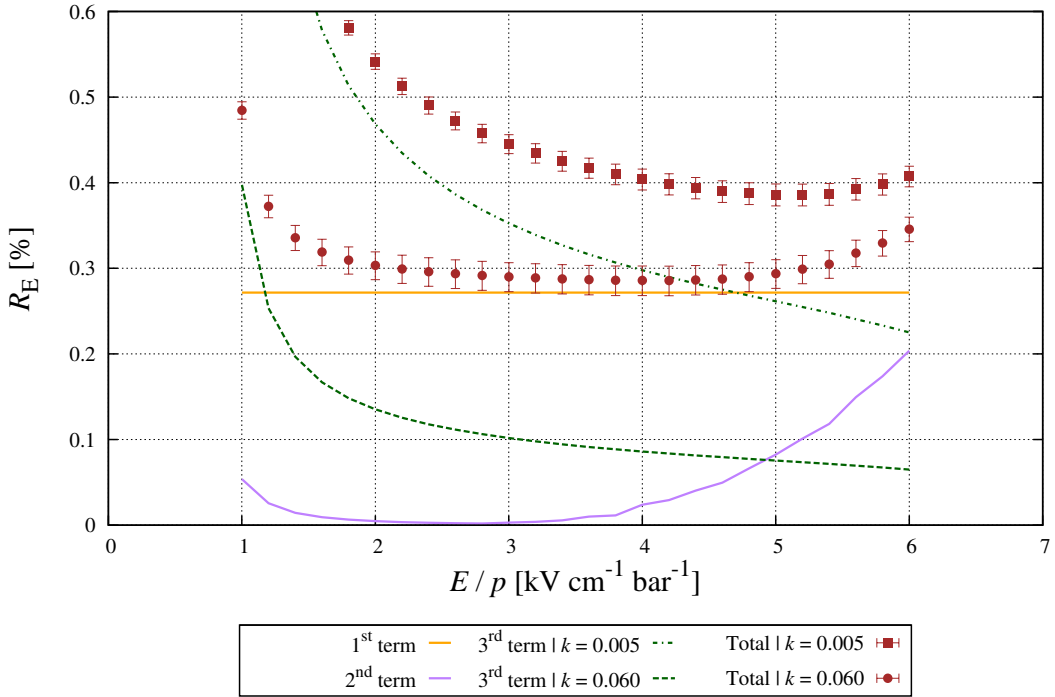


Figure 7.6: FWHM energy resolution, R_E , as a function of the reduced electric field for two different scenarios: an optimistic (circles, $k = 0.06$) and a conservative (squares, $k = 0.005$). The values of R_E if only each of the three terms of Equation (7.1) would contribute are also shown.

The FWHM energy resolution obtained using the simulated yield and fluctuations in Equation (7.1), R_E , is shown in Figure 7.6 as a function of the reduced electric field, for two different scenarios in terms of VUV photodetection efficiency: an optimistic ($k = 0.06$ [135]) and a conservative ($k = 0.005$ [10]). The parameter k is the fraction of VUV photons produced per $\beta\beta^{0\nu}$ decay that are converted into photoelectrons in the PMT photocathode. This fraction depends on the implicit solid angle associated with the array of PMTs and on the quantum efficiency of the photocathode. The contributions of each of the three terms of Equation (7.1) are also shown in Figure 7.6. The optimal energy resolution, below 0.4 % for both the considered scenarios, is achieved for electric fields that are higher than the one marking the beginning of ionization, shown in Figure 7.4 as the reduced field value minimizing the value of J_{VUV} . The reason is that the still small additional fluctuations introduced by the production of secondary charge are compensated by the increase in the number of photons produced per primary electron due to the increase of the EL yield. As expected, the reduced electric field value which gives the best energy resolution increases as k decreases, and the best value of R_E is worst for lower values of k . For the conditions considered here, the best energy

resolution is obtained for $\left(\frac{E}{p}\right)$ between ~ 3.5 and $\sim 5.0 \text{ kVcm}^{-1}\text{bar}^{-1}$.

MWPC as an alternative VUV EL amplification stage

Taking a reference value for the optimal reduced electric field of $4.0 \text{ kVcm}^{-1}\text{bar}^{-1}$, a voltage of 20,000 V needs to be applied along the parallel gap ($d = 5 \text{ mm}$). This implies the use of special and expensive power supplies and very careful design and construction of the electrodes in order to avoid mechanical deformations by the created strong electrostatic forces.

As seen in Chapter 5, D. Nygren has proposed the MWPC geometry as an alternative for EL production in SDCs [135], as in the case of NEXT. Also in Chapter 5, a simulation of the VUV EL produced in a simple cylindrical geometry was performed, being determined the total yield and associated fluctuations. In a MWPC, the volume in the vicinity of each wire is well described by the cylindrical shape of the electric field considered in the simulations (see Equation 1.17). As the production of EL is highly localized (see Figure 5.5), the EL response of a MWPC can be easily extrapolated from the results obtained for the simple cylindrical geometry.

Using the VUV EL total yield and the fluctuations estimated in Chapter 5 for xenon at 10 bar and 293 K (see Figures 5.2b) and 5.3b) respectively), the FWHM energy resolution achievable with a MWPC working in EL mode was determined through Equation (7.1), similarly to what was done for the uniform electric field. The same values of F , W and $Q_{\beta\beta}$ were used, as well as the same two scenarios in terms of VUV photodetection ($k = 0.06$ – optimistic – and $k = 0.005$ – conservative). Figure 7.7 shows the FWHM energy resolution, calculated for some of the wire diameters used in the simulations and as a function of the applied voltage.

Similarly to what was observed for the parallel gap, the optimal energy resolution, for each wire diameter, is achieved for a voltage which is higher than the one marking the worsening of the EL VUV fluctuations (seen in Figure 5.3b) as the electric potential minimizing the value of J_{VUV}). As the wire diameter increases, the optimal energy resolution improves as a consequence of the increase of the total VUV yield achievable for the same VUV fluctuations (see Section 5.2).

Taking the example of $d_w = 0.2 \text{ mm}$, it is possible to achieve energy resolutions of $\sim 0.34 \%$ in the case of the optimistic scenario and of $\sim 0.59 \%$ if the conservative scenario is considered. These energy resolutions imply the use voltages of the order of 10,000 V, about half of what is needed in the case of the parallel gap of NEXT, for which resolutions of $\sim 0.29 \%$ and $\sim 0.39 \%$ are achieved for $k = 0.060$ and $k = 0.005$, respectively (as presented in Figure 7.6). Thus, the use of a plane of wires as the VUV EL amplification stage in a detector such as NEXT can, in principle, allow to use

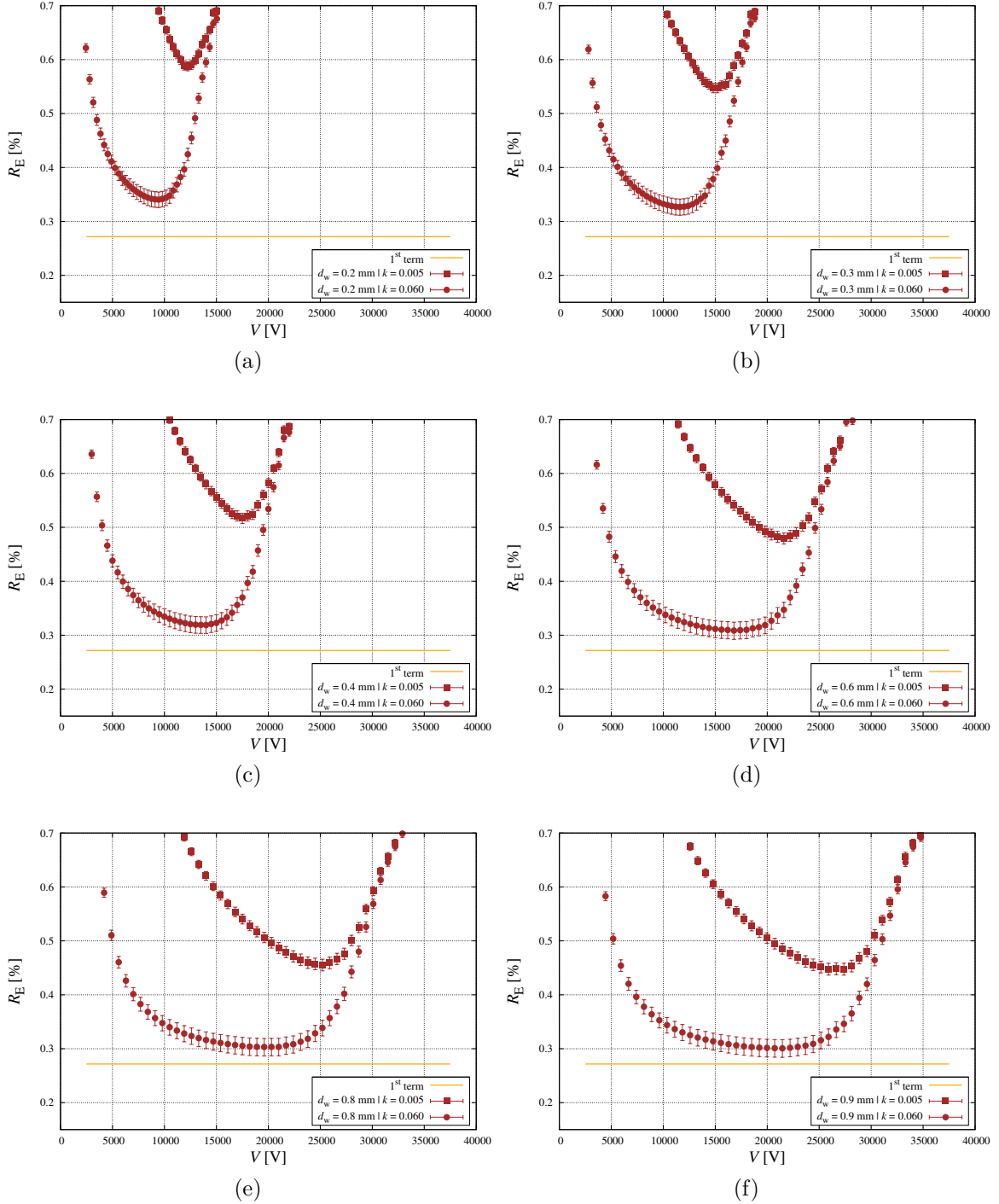


Figure 7.7: FWHM energy resolution of a MWPC working in VUV EL mode, as a function of the applied potential, for different wire diameters and for two different VUV photodetection schemes: $k = 0.06$ (circles) and $k = 0.005$ (squares). The value of R_E if only the fluctuations in the primary charge creation would contribute (1^{st} term of Eq. (7.1)) is shown. The tube diameter is 60 mm in all the cases. The results are for xenon at 10 bar and 293 K.

significantly lower voltages without a big compromise in terms of energy resolution.

It should be noted that the use of a MWPC geometry for VUV EL production in NEXT would imply modifications on its tracking function. As suggested by Figure 5.5, the EL VUV photons are emitted isotropically in a confined region of each wire vicinity. The majority of the photons are emitted from the side of the wire plane where the electrons came from. For the measuring of the energy resolution this is not a problem since the array of PMTs is placed in that side, being the fraction of photons arriving to the array similar to the case of the parallel gap. However, the array of MPPCs, which consist in the tracking system of the detector, is in the opposite side. Thus, the wires block a big fraction of the VUV photons, producing a shadow effect.

7.5 Discussion

In this Chapter, the simulation results for the VUV EL produced in the NEXT $\beta\beta^{0\nu}$ experiment were shown. The VUV yield and the corresponding fluctuations produced in such a setup, corresponding to a EL region given by a 5 mm uniform electric field gap of xenon at 293 K temperature and 10 bar pressure, were determined. A FWHM energy resolution of 0.4% or better at the Q value of the $\beta\beta^{0\nu}$ reaction, $Q_{\beta\beta} = 2.458$ MeV, can in principle be obtained, even considering conservative assumptions regarding the VUV photodetection efficiency.

The simulations indicate that the 1% FWHM energy resolution goal of the NEXT experiment can in principle be met and even be improved upon, as far as fluctuations in the primary ionization charge, in the EL, and in the VUV photodetection processes were considered. This energy resolution goal is one of the main figures of merit for the NEXT experiment [10].

The FWHM energy resolution achievable by using a plane of wires as the VUV EL amplification stage, instead of the parallel gap of 5 mm width, was also calculated. It was found that, in principle, such geometry would allow to operate the detector using lower voltages with a slightly worse energy resolution (still below the 1 % goal of NEXT).

CHAPTER 8

Conclusions & future work

8.1 Conclusions

The C++ version of the microscopic technique of Garfield, allows to gather information on the excited atoms produced during the drift of electrons through gaseous detectors. Such simulations rely on detailed cross sections for elastic collisions, excitations and ionizations as modelled by Magboltz 8.9.5. In this thesis, this information was used to implement an atomic and molecular decay model and a simulation toolkit for the EL properties of gaseous detectors. The studied gases were pure noble gases, namely neon, argon, krypton and xenon, but the toolkit has potential to simulate EL in other gases including mixtures with molecular substances. By considering that every excited atom leads to the emission of a VUV photon and that atoms in an higher state than those of the first excited shell configuration $np^5(n+1)s^1$ can emit a Vis-IR photon before the emission of the VUV light, it is possible to simulate both VUV and Vis-IR electroluminescence and evaluate its intrinsic properties as well as the responses of realistic detector geometry setups.

Intrinsic EL properties of noble gases - uniform electric field

In order to assess the intrinsic properties of EL, electrons drifting in pure neon, argon, krypton and xenon, under influence of uniform electric fields were considered. Collision rates of each level/group and the kinetic energy distribution of the electrons were determined. It was confirmed that the atomic states that most contribute to VUV EL are those of the $np^5(n+1)s^1$ electronic shell configuration.

The estimation of the VUV EL efficiency, which is higher than 70 % for all gases under optimal conditions, confirmed that a big fraction of the energy supplied to the electrons by the electric field is converted into VUV light. As a direct consequence, there is a high VUV EL yield, which was calculated as a function of the applied electric field. A very good overall agreement with earlier Monte Carlo simulations and measurements was obtained for argon and xenon, validating the toolkit and the used atomic and excimer decay model.

The statistical fluctuations associated with VUV EL were also calculated as functions of the electric field. It was found that they decrease as the field increases until the ionization onset, for which the fluctuations in the secondary charge production start to dominate. It was confirmed that these VUV EL fluctuations are lower than those in both charge avalanche multiplication and primary electron cloud formation. To the best of the author knowledge, up to now, there are not consistent values for J_{VUV} published in literature, being thus the first time that these parameters are presented for the studied gases.

Two approaches were considered for simulating the Vis-IR EL in argon and xenon:

one considering that only $np^5(n+1)p^1$ levels give rise to Vis-IR photons; and the other considering that any level in a shell configuration different of $np^5(n+1)s^1$ produces ultimately a Vis-IR photon. The recently measured absolute reduced Vis-IR yield was found to be between the curves given by the considered two approaches, which indicates the high potential of the toolkit to simulate accurately also the Vis-IR EL in the considered gases.

Cylindrical geometry – Xenon

The total yield and associated fluctuations of VUV EL produced in a simple cylindrical geometry were estimated for xenon using the simulation toolkit.

It was found that the VUV EL yield that can be reached before the worsening of the fluctuations due to avalanche multiplication is higher for wider wires and higher gas pressures, and that the better EL fluctuations, achievable for a given wire diameter, worsen with the increase of the latter.

The spatial distributions of the excitations suggest that the emission of VUV EL photons is confined to the vicinity of each wire and happen predominantly on the side of the wire where the primary electrons came from.

VUV EL in MPGDs – Xenon

The total yield of VUV EL produced in the microstructures GEM and MHSP working in xenon was estimated.

The simulations were able to approximately reproduce experimental data for the case of the GEM. Some of the disagreement can be attributed to imperfections introduced during the construction of the microstructure. It was found that the solid angle subtended by a VUV photodetection device, placed below the GEM, is dependent on the total light gain. The ratio between the number of VUV photons and the number of produced secondary charges is higher for higher pressures and, for avalanche regimes, decreases as the voltage applied along the holes is increased.

The results obtained for the case of the MHSP are not consistent with measurements. The disagreement between experimental yields reported for GEM and MHSP suggests the occurrence of some imperfections in the MHSP used for the measurements. The poor gas purification method used during the measurements with which the simulation results were compared can also explain the disagreement.

NEXT - Neutrino Experiment with a Xenon TPC

The toolkit was used to estimate the properties of the NEXT-EL detector and to determine the best voltages to be used. The VUV EL yield and the corresponding fluctuations produced in such a setup, corresponding to a EL region given by a 5 mm

uniform electric field gap of xenon at a temperature of 293 K and a pressure of 10 bar were assessed. In principle, a FWHM energy resolution of 0.4% or better at the Q value of the $\beta\beta^{0\nu}$ reaction, $Q_{\beta\beta} = 2.458$ MeV, can be obtained, even considering conservative assumptions regarding the VUV photodetection efficiency. This indicates that the 1% FWHM energy resolution goal of the NEXT experiment can in principle be met and even be improved upon, as far as fluctuations in the primary ionization charge, in the EL production, and in the VUV photodetection processes are considered in the analysis.

The FWHM energy resolution achievable by using a plane of wires as the VUV EL amplification stage was also estimated. It was found that such geometry can be a good alternative, allowing the operation with lower voltages and reaching energy resolutions still below the 1 % goal of NEXT.

8.2 Future work

The simulations performed during this work led to a deeper understanding of the involved processes and of the properties of electroluminescence produced by electron impact in pure noble gases. On the other hand they triggered new studies that will certainly contribute for the improvement of the simulation tools and for the developing of EL based new technologies. The latter will certainly have applications in the building of outstanding particle detectors that will contribute for the breaking of Science's frontiers, regarding our knowledge of elementary particles.

Some of these studies are already underway and others will be done in the DRIM group, University of Aveiro, or in collaboration with other national and international groups:

- In the Chapter 4, the simulation toolkit and the cross sections that Magboltz 8.9.5 uses for the different electron impact processes were validated by comparing the simulated reduced VUV EL yield of argon and xenon with those measured in references [67, 68]. The yield will also be measured for the case of krypton in order to validate also the cross sections used for this gas. This is being prepared in collaboration with the *Grupo de Instrumentação Atómica e Nuclear* (GIAN), from Coimbra, Portugal. In parallel, S. Biagi, from the University of Liverpool, UK, is updating the cross sections of krypton in order to describe excitations in more detail, using a number of split groups of the same order of those used for neon, argon and xenon (45, 44 and 50 respectively), instead of the actual 4 groups.

- Also in Chapter 4, two approaches were considered for the atomic decay between excited atoms. The comparison of the results for the Vis-IR EL reduced yield obtained through these approaches and the available measurements for argon [117] allowed to conclude that the actual Vis-EL yield can be simulated using a model between these two approaches. However, the correct ratios of the different branch decays from each excited state higher than $np^5(n+1)s^1$ (some of them available in literature) should be implemented for further improvement of the simulations. This task is underway, in collaboration with S. Biagi and R. Veenhof, under the CERN RD51 collaboration.
- In the Chapter 6, the toolkit was able to approximately simulate the total VUV EL yield of the microstructures GEM and MHSP, although some disagreement with measurements [138] is still present. Some imperfections introduced during the construction of the microstructures can be a source of the observed differences between the results. In order to confirm this, the experimental yield should be compared with new simulation results obtained considering the correct geometry of the devices, that could be obtained using simple imaging techniques.

The charging-up is, at this moment, being studied through simulations that construct iteratively the field maps taking into account the charge deposited in the surface of the Kapton® between iterations. This work is being developed within the CERN RD51 collaboration.

The C++ toolkit is currently being interfaced with the *nearly exact Boundary Element Method* [121] that calculates the electric potential and field using Green's functions, which are solutions of the Maxwell equations, unlike the polynomials used in the FEM method. The simulations of the GEM and MSHP will be repeated using this method, in collaboration with the Saha Institute of Nuclear Physics, Kolkata, India.

- Mixtures of noble gases with molecular scintillating gases are also of great interest in particle detector applications. Tetrafluoromethane (CF_4) is one of the most interesting gases due to its high EL yield. Since these are Penning mixtures, a detailed radiative and collisional decay model needs to be constructed and implemented, in order to endow the toolkit with the capability of simulating EL produced in these gases.
- Recently, it was proposed the addition of small quantities of trimethylamine (TMA) or dimethylamine (DMA) to xenon in order to further decrease the fluctuations in the primary charge creation. These fluctuations are the main drawback

for the energy resolution and thus, it is of major interest to reduce them. TMA and DMA have potentially a *Penning effect* with xenon, reducing the primary charge fluctuations. At the same time they emit light in the 280 – 310 nm range when excited. Further experimental and simulation studies will be performed in order to confirm these properties and to determine the optimal conditions of operation for such mixtures. This work is to be done in collaboration with D. Nygren, from the Lawrence Berkeley National Laboratory, Berkeley, California, USA.

APPENDIX A

Cross sections used by Magboltz

8.9.5

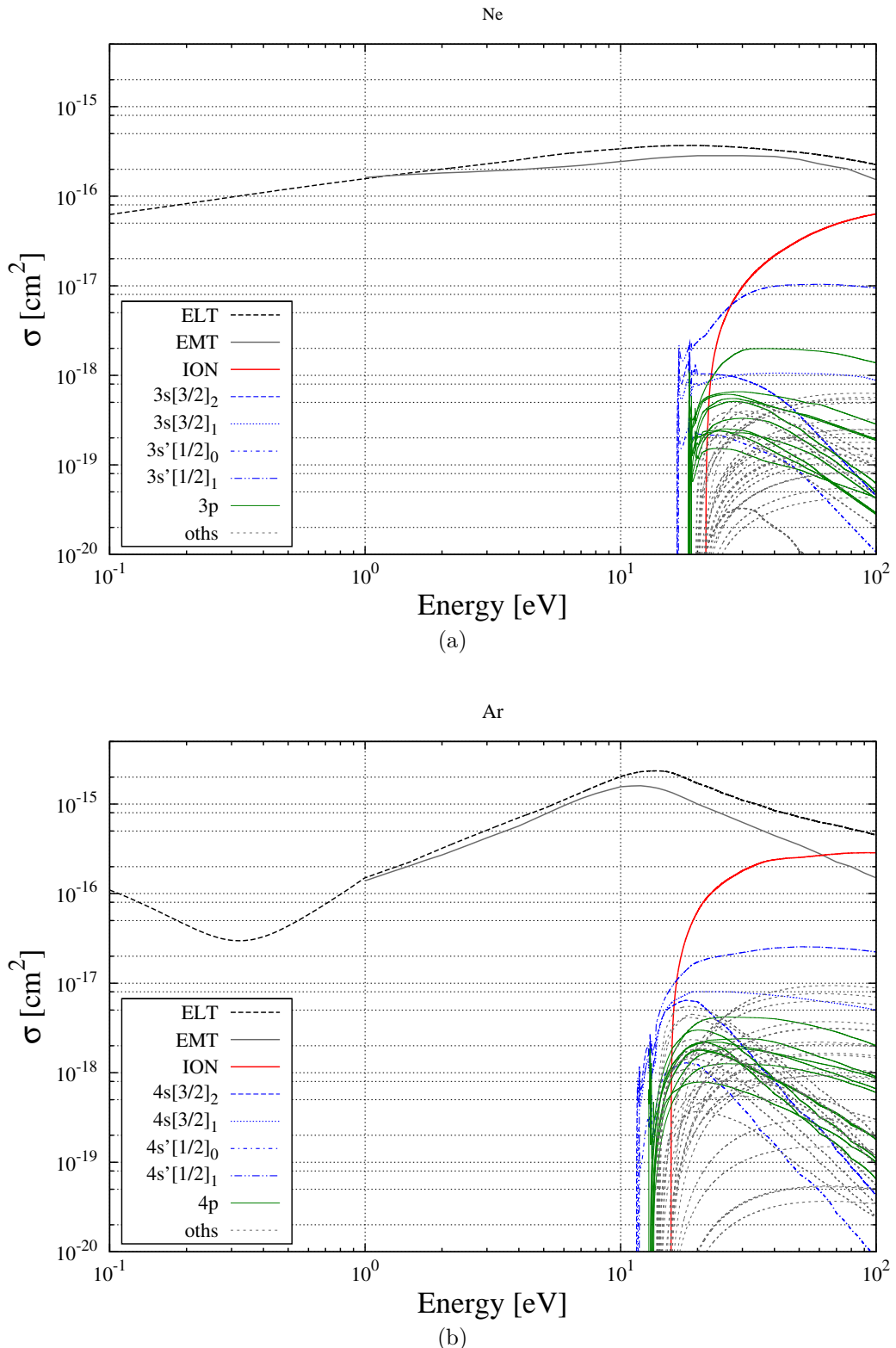


Figure A.1: Cross sections used in Magboltz 8.9.5 for (a) neon and (b) argon. EMT stands for Elastic Momentum Transfer cross section and ELT for Total ELastic cross section. The blue lines refer to the first four excited states of the electronic shell configuration $np^5(n+1)s^1$, the green lines correspond to the 10 levels of the $np^5(n+1)p^1$ configuration, and the gray dotted lines to other sparsely populated levels. The red line corresponds to ionization (ION).

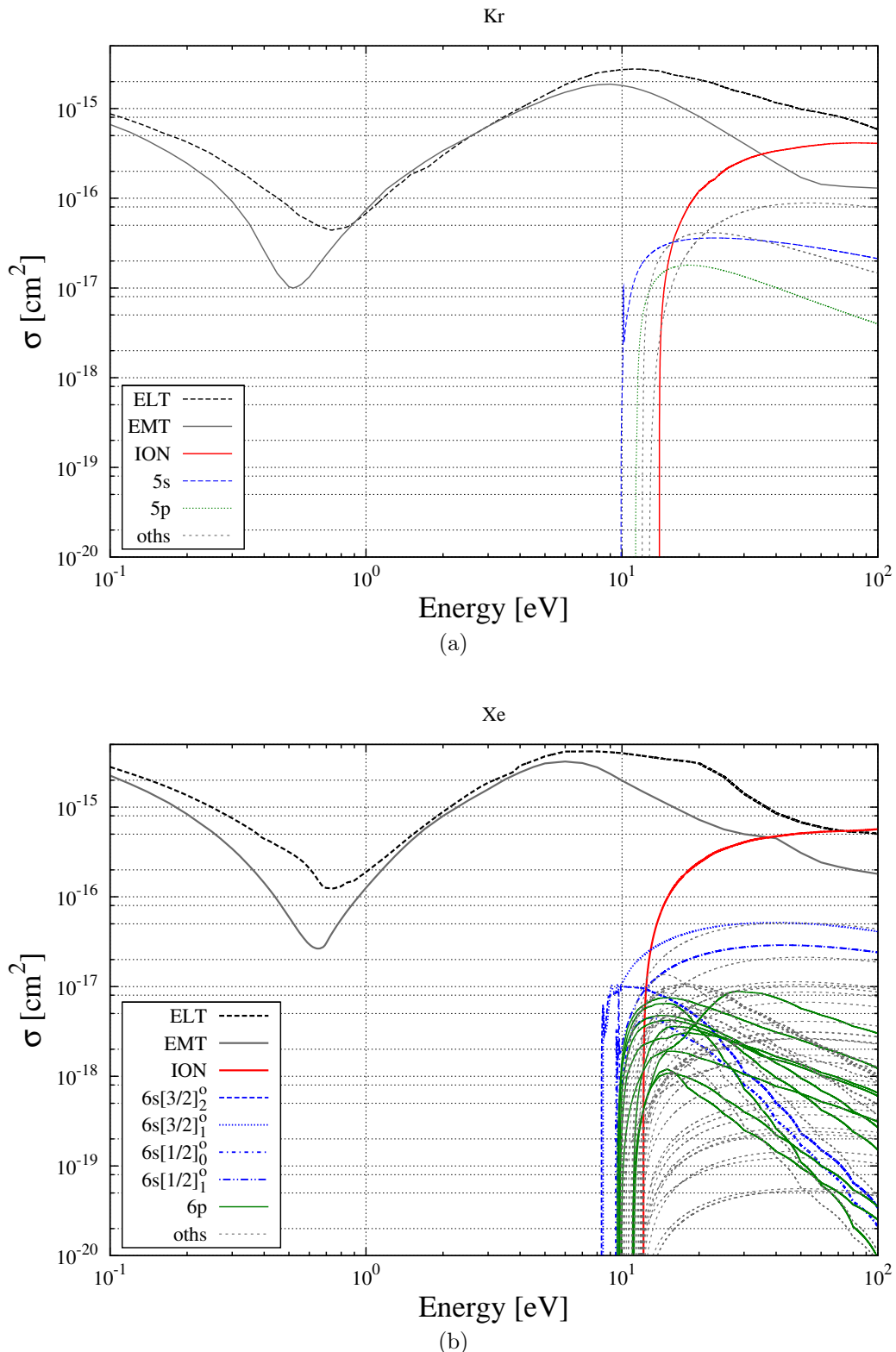


Figure A.2: Cross sections used in Magboltz 8.9.5 for (a) krypton and (b) xenon. EMT stands for Elastic Momentum Transfer cross section and ELT for Total ELastic cross section. The blue lines refer to the first four excited states of the electronic shell configuration $np^5(n+1)s^1$, the green lines correspond to the 10 levels of the $np^5(n+1)p^1$ configuration, and the gray dotted lines to other sparsely populated levels. The red line corresponds to ionization (ION).

collision type	ϵ_{loss} [eV]	Description (level / group)
elastic	0	—
ionization	21.5645	—
excitation	16.6191	3s[3/2]_2
excitation	16.6708	3s[3/2]_1
excitation	16.7154	3s'[1/2]_0
excitation	16.8480	3s'[1/2]_1
excitation	18.3816	3p[1/2]_1
excitation	18.5551	3p[5/2]_3
excitation	18.5758	3p[5/2]_2
excitation	18.6127	3p[3/2]_1
excitation	18.6368	3p[3/2]_2
excitation	18.6934	3p[1/2]_0
excitation	18.7041	3p'[3/2]_1
excitation	18.7114	3p'[3/2]_2
excitation	18.7264	3p'[1/2]_1
excitation	18.9660	3p'[1/2]_0
excitation	19.6640	4s[3/2]_2
excitation	19.6882	4s[3/2]_1
excitation	19.7606	4s[1/2]_0
excitation	19.7798	4s[1/2]_1
excitation	20.0246	2d[1/2]_0
excitation	20.0264	2d[1/2]_1
excitation	20.0347	2d[7/2]_4
excitation	20.0349	2d[7/2]_3
excitation	20.0368	2d[3/2]_2
excitation	20.0404	2d[3/2]_1
excitation	20.0482	2d[5/2]_2
excitation	20.0484	2d[5/2]_3
excitation	20.1361	2d'[5/2]_2
excitation	20.1363	2d'[5/2]_3
excitation	20.1375	2d'[3/2]_2
excitation	20.1395	2d'[3/2]_1
excitation	20.1497	4p[1/2]_1+4p[5/2]_3+4p[5/2]_2+4p[3/2]_1+4p[3/2]_2
excitation	20.2592	4p[1/2]_0+4p'[3/2]_1+4p'[3/2]_2+4p'[1/2]_1
excitation	20.3689	4p'[1/2]_0
excitation	20.5706	5s[3/2]_1
excitation	20.6628	5s'[1/2]_1
excitation	20.7023	3d[1/2]_1
excitation	20.7087	3d[3/2]_1
excitation	20.8055	3d'[3/2]_1
excitation	20.9493	6s[3/2]_1
excitation	21.0139	4d[1/2]_1
excitation	21.0174	4d[3/2]_1
excitation	21.0435	6s'[1/2]_1
excitation	21.1140	4d'[3/2]_1
excitation	21.1464	sum of higher s states
excitation	21.1829	sum of higher d states

Table A.1: Description of the levels/groups used in Magboltz 8.9.5 for neon. The collision type and the energy loss are also included.

collision type	ϵ_{loss} [eV]	Description (level / group)
elastic	0	–
ionization	15.760	–
excitation	11.548	4s[3/2]₂
excitation	11.624	4s'[3/2]₁
excitation	11.723	4s'[1/2]₀
excitation	11.828	4s'[1/2]₁
excitation	12.907	4p[1/2]₁
excitation	13.076	4p[5/2]₃
excitation	13.095	4p[5/2]₂
excitation	13.153	4p[3/2]₁
excitation	13.172	4p[3/2]₂
excitation	13.273	4p[1/2]₀
excitation	13.283	4p'[3/2]₁
excitation	13.302	4p'[3/2]₂
excitation	13.328	4p'[1/2]₁
excitation	13.480	4p'[1/2]₀
excitation	13.845	3d[1/2]₀
excitation	13.864	3d[1/2]₁
excitation	13.903	3d[3/2]₂
excitation	13.979	3d[7/2]₄
excitation	14.013	3d[7/2]₃
excitation	14.063	3d[5/2]₂
excitation	14.068	5s[3/2]₂
excitation	14.090	5s[3/2]₁
excitation	14.099	3d[5/2]₃
excitation	14.153	3d[3/2]₁
excitation	14.214	3d'[5/2]₂
excitation	14.234	3d'[3/2]₂
excitation	14.236	3d'[5/2]₃
excitation	14.241	5s'[1/2]₀
excitation	14.255	5s'[1/2]₁
excitation	14.304	3d'[3/2]₁
excitation	14.711	4d[1/2]₁
excitation	14.848	6s[3/2]₁
excitation	14.859	4d[3/2]₁
excitation	15.004	4d'[3/2]₁
excitation	15.022	6s'[1/2]₁
excitation	15.118	5d[1/2]₁
excitation	15.186	7s[3/2]₁
excitation	15.190	5d[3/2]₁
excitation	15.308	6d[1/2]₁
excitation	15.351	5d'[3/2]₁
excitation	15.360	7s'[1/2]₁
excitation	15.366	8s[3/2]₁
excitation	15.374	6d[3/2]₁
excitation	15.660	sum of higher states

Table A.2: Description of the levels/groups used in Magboltz 8.9.5 for argon. The collision type and the energy loss are also included.

collision type	ϵ_{loss} [eV]	Description (level / group)
elastic	0	—
ionization	13.996	—
excitation	9.915	$5s[3/2]_2 + 5s[3/2]_1 + 5s'[1/2]_0 + 5s'[1/2]_1$
excitation	11.304	$5p[1/2]_1 + 5p[5/2]_3 + 5p[5/2]_2 + 5p[3/2]_1 + 5p[3/2]_2 + 5p[1/2]_0$
excitation	11.998	$4d[1/2]_0 + 4d[1/2]_1 + 4d[7/2]_4 + 4d[7/2]_3$ $4d[3/2]_2 + 4d[3/2]_1 + 4d[5/2]_2 + 4d[5/2]_3$ $5p'[3/2]_1 + 5p'[3/2]_2 + 5p'[1/2]_1 + 5p'[1/2]_0$ $6s[3/2]_2 + 6s[3/2]_1 + 6s'[1/2]_0 + 6s'[1/2]_1$
excitation	12.750	sum of higher states

Table A.3: Description of the levels/groups used in Magboltz 8.9.5 for krypton. The collision type and the energy loss are also included.

collision type	ϵ_{loss} [eV]	Description (level / group)
elastic	0	—
ionization	12.1298	—
excitation	8.3153	6s[3/2]₂
excitation	8.4365	6s[3/2]₁
excitation	9.4472	6s'[1/2]₀
excitation	9.5697	6s'[1/2]₁
excitation	9.5802	6p[1/2]₁
excitation	9.6856	6p[5/2]₃
excitation	9.7207	6p[5/2]₂
excitation	9.7893	6p[3/2]₁
excitation	9.8211	6p[3/2]₂
excitation	9.8904	5d[1/2]₀
excitation	9.9171	5d[1/2]₁
excitation	9.9335	6p[1/2]₀
excitation	9.9431	5d[7/2]₄
excitation	9.9588	5d[3/2]₂
excitation	10.0391	5d[7/2]₃
excitation	10.1575	5d[5/2]₂
excitation	10.2200	5d[5/2]₃
excitation	10.4010	5d[3/2]₁
excitation	10.5621	7s[3/2]₂
excitation	10.5932	7s[3/2]₁
excitation	10.9016	7p[1/2]₁ + 7p[5/2]₃ + 7p[5/2]₂ + 7p[3/2]₁ + 7p[3/2]₂ + 7p[1/2]₀
excitation	10.9576	6p'[3/2]₁
excitation	10.9715	6d[1/2]₀ + 6d[7/2]₄ + 6d[7/2]₃ + 6d[3/2]₂ + 6d[5/2]₂ + 6d[5/2]₃
excitation	10.9788	6d[1/2]₁
excitation	11.0547	6p'[3/2]₂
excitation	11.0691	6p'[1/2]₁
excitation	11.1412	6p'[1/2]₀
excitation	11.1626	6d[3/2]₁
excitation	11.2742	8s[3/2]₁
excitation	11.4225	7d[1/2]₁
excitation	11.4951	7d[3/2]₁
excitation	11.5829	9s[3/2]₁
excitation	11.6072	5d'[3/2]₁
excitation	11.6828	8d[1/2]₁
excitation	11.7395	8d[3/2]₁
excitation	11.7521	10s[3/2]₁
excitation	11.8068	9d[1/2]₁
excitation	11.8403	9d[3/2]₁
excitation	11.8518	11s[3/2]₁
excitation	11.8778	7s[1/2]₁
excitation	11.8917	10d[1/2]₁
excitation	11.9082	10d[3/2]₁
excitation	11.9177	12s[3/2]₁
excitation	11.9416	11d[1/2]₁
excitation	11.9550	11d[3/2]₁
excitation	11.9621	13s[3/2]₁
excitation	11.9789	12d[1/2]₁
excitation	11.9886	12d[3/2]₁
excitation	11.9939	14s[3/2]₁
excitation	12.0000	sum of higher states

Table A.4: Description of the levels/groups used in Magboltz 8.9.5 for xenon. The collision type and the energy loss are also included.

APPENDIX B

Toolkit C++ code and illustrative script

The C++ code that implements the simulation toolkit is included in the CD attached to this document (see folder “\$CD_ROOT_DIR/garf++/”).

The instructions for preparing and compiling the code are included in the file “README.txt”.

It is possible to find an illustrative script for the VUV EL simulation of pure noble gases in uniform electric fields in the folder “\$ROOT_DIR/garf++/online”.

For further updates of the toolkit please consult “<http://cern.ch/garfieldpp>”.

Bibliography

- [1] E. Aprile et al. First Dark Matter Results from the XENON100 Experiment. *Phys. Rev. Lett.*, 105(13):131302, 2010.
- [2] WARP proposal, <http://warp.lngs.infn.it/papers/proposal.pdf> [2011, May 18].
- [3] P. Benetti et al. First results from a dark matter search with liquid argon at 87 K in the Gran Sasso underground laboratory. *Astropart. Phys.*, 28(6):495 – 507, 2008.
- [4] Large Underground Xenon, <http://lux.brown.edu/> [2011, May 17].
- [5] M. C. Gonzalez-Garcia and M. Maltoni. Phenomenology with massive neutrinos. *Phys. Rep.*, 460(1-3):1 – 129, 2008.
- [6] S. R. Elliott and J. Engel. Double-beta decay. *J. Phys. G: Nucl. Part. Phys.*, 30(9):R183, 2004.
- [7] D. Sinclair. EXO Gas: Ba tagging and tracking. *Xenon Detector Workshop*, November 16-18, 2009, Berkeley, CA, USA.
- [8] The NEXT collaboration. The NEXT experiment. *J. Phys. Conf. Ser.*, 179(1):012005, 2009.
- [9] Justo Martín-Albo and the Next Collaboration. The NEXT experiment: neutrinoless double beta decay searches at the LSC. *J. Phys. Conf. Ser.*, 259(1):012040, 2010.
- [10] The NEXT Collaboration. NEXT, a HPGXe TPC for neutrinoless double beta decay searches. *arXiv:0907.4054v1 [hep-ex]*, 2009.
- [11] G. F. Knoll. *Radiation Detection and Measurement, 3rd Edition*. Springer-Verlag, 1992.
- [12] XCOM: Photon Cross Sections Database, <http://www.nist.gov/pml/data/xcom/index.cfm> [2011, May 21].
- [13] NIST, Stopping-Power and Range Tables for Electrons, Protons, and Helium Ions, <http://www.nist.gov/pml/data/star/index.cfm> [2011, May 24].
- [14] H. Bethe. Zur Theorie des Durchgangs schneller Korpuskularstrahlen durch Materie. *Annalen der Physik*, 397(3):325–400, 1930.

- [15] H. Bethe. Bremsformel für Elektronen relativistischer Geschwindigkeit. *Zeitschrift für Physik A Hadrons and Nuclei*, 76:293–299, 1932. 10.1007/BF01342532.
- [16] Stephen M. Seltzer and Martin J. Berger. Bremsstrahlung spectra from electron interactions with screened atomic nuclei and orbital electrons. *Nucl. Instrum. Methods Phys. Res., Sect. B*, 12(1):95 – 134, 1985.
- [17] Ground levels and ionization energies for the neutral atoms, <http://physics.nist.gov/physrefdata/ionenergy/tblnew.html> [2011, march 15].
- [18] N. Ishida, J. Kikuchi, T. Doke, and M. Kase. Fano factor in xenon. *Phys. Rev. A*, 46(3):1676–1679, 1992.
- [19] R. L. Platzman. Total ionization in gases by high-energy particles: An appraisal of our understanding. *Int. J. Appl. Radiat. Isot.*, 10(2-3):116 – 127, 1961.
- [20] L. M. P. Fernandes, E. D. C. Freitas, M. Ball, J. J. Gómez-Cadenas, C. M. B. Monteiro, N. Yahlali, D. Nygren, and J. M. F. dos Santos. Primary and secondary scintillation measurements in a Xenon Gas Proportional Scintillation Counter. *J. Instrum.*, 5(09):P09006, 2010.
- [21] S. J. C. do Carmo, F. I. G. M. Borges, F. P. Santos, T. H. V. T. Dias, and C. A. N. Conde. Absolute primary scintillation yield of gaseous xenon under low drift electric fields for 5.9 keV X-rays. *J. Instrum.*, 3(07):P07004, 2008.
- [22] A. Parsons, B. Sadoulet, S. Weiss, T. Edberg, J. Wilkerson, G. Smith, R.P. Lin, and K. Hurley. High pressure gas scintillation drift chambers with wave shifter fiber readout. *IEEE Trans. Nucl. Sci.*, 36(1):931 – 935, 1989.
- [23] U. Fano. Ionization Yield of Radiations. II. The Fluctuations of the Number of Ions. *Phys. Rev.*, 72(1):26–29, 1947.
- [24] A. J. P. L. Policarpo, M. A. F. Alves, M. Salete, S. C. P. Leite, and M. C. M. dos Santos. Detection of soft X-rays with a xenon proportional scintillation counter. *Nucl. Instrum. Methods*, 118(1):221 – 226, 1974.
- [25] H. Sipilä. Energy resolution of the proportional counter. *Nucl. Instrum. Methods*, 133(2):251 – 252, 1976.
- [26] D. F. Anderson, T. T. Hamilton, W. H.M. Ku, and R. Novick. A large area, gas scintillation proportional counter. *Nucl. Instrum. Methods*, 163(1):125 – 134, 1979.
- [27] M. M. F. Ribeirete, A. J. P. L. Policarpo, M. Salete, S. C. P. Leite, M. A. F. Alves, and E. P. de Lima. Fano factors of krypton-xenon mixtures. *Nucl. Instrum. Methods Phys. Res.*, 214(2-3):561 – 563, 1983.
- [28] E. P. de Lima, M. Salete, S. C. P. Leite, M. A. F. Alves, and A. J. P. L. Policarpo. Fano factors of rare gases and their mixtures. *Nucl. Instrum. Methods Phys. Res.*, 192(2-3):575 – 581, 1982.

- [29] T. Doke, N. Ishida, and M. Kase. Fano factors in rare gases and their mixtures. *Nucl. Instrum. Methods Phys. Res., Sect. B*, 63(4):373 – 376, 1992.
- [30] A. Hashiba, K. Masuda, T. Doke, T. Takahashi, and Y. Fujita. Fano factor in gaseous argon measured by the proportional scintillation method. *Nucl. Instrum. Methods Phys. Res., Sect. A*, 227(2):305 – 310, 1984.
- [31] M. Kase, T. Akioka, H. Mamyoda, J. Kikuchi, and T. Doke. Fano factor in pure argon. *Nucl. Instrum. Methods Phys. Res., Sect. A*, 227(2):311 – 317, 1984.
- [32] T. H. V. T. Dias, J. M. F. dos Santos, P. J. B. M. Rachinhas, F. P. Santos, C. A. N. Conde, and A. D. Stauffer. Full-energy absorption of x-ray energies near the Xe L- and K-photoionization thresholds in xenon gas detectors: Simulation and experimental results. *J. Appl. Phys.*, 82(6):2742–2753, 1997.
- [33] J. Miyamoto and G. F. Knoll. The statistics of avalanche electrons in micro-strip and micro-gap gas chambers. *Nucl. Instrum. Methods Phys. Res., Sect. A*, 399(1):85 – 93, 1997.
- [34] A. Ravazzani, A. Foglio Para, R. Jaime, M. Looman, M. Marn Ferrer, P. Peerani, and P. Schillebeeckx. Characterisation of ${}^3\text{He}$ proportional counters. *Radiat. Meas.*, 41(5):582 – 593, 2006.
- [35] G. Charpak, R. Bouclier, T. Bressani, J. Favier, and C. Zupancic. The use of multiwire proportional counters to select and localize charged particles. *Nucl. Instrum. Methods*, 62(3):262 – 268, 1968.
- [36] D. Nygren. *PEP-198-1975*.
- [37] H. J. Hilke. Time projection chambers. *Rep. Prog. Phys.*, 73(11):116201, 2010.
- [38] ALICE collaboration. ALICE time projection chamber: Technical Design Report, CERN-LHCC-2000-001, <http://cdsweb.cern.ch/record/451098>.
- [39] ALICE, A Large Ion Collider Experiment, <http://aliceinfo.cern.ch/Public/en/Chapter1/firstHI.html> [2011, June 3].
- [40] L. Evans and P. Bryant. LHC Machine. *J. Instrum.*, 3(08):S08001, 2008.
- [41] A. Oed. Position-sensitive detector with microstrip anode for electron multiplication with gases. *Nucl. Instrum. Methods Phys. Res., Sect. A*, 263(2-3):351 – 359, 1988.
- [42] F. Angelini, R. Bellazzini, A. Brez, E. Focardi, M. M. Massai, F. Sauli, G. Span-dre, and M. R. Torquati. The microstrip gas avalanche chamber: a new detector for the next generation of high-luminosity machines. *Proceedings of ECFA Study Week on Instrumentation Technology for High-luminosity Hadron Colliders (Barcelona)*, CERN-89-10, page 645, 1989.

- [43] F. Angelini, R. Bellazzini, A. Brez, M. M. Massai, G. Spandre, M. R. Torquati, R. Bouclier, J. Gauden, and F. Sauli. Test-beam study of the performance of the microstrip gas avalanche chamber. *IEEE Trans. Nucl. Sci.*, 37(2):112 –118, 1990.
- [44] J. E. Bateman, J. F. Connolly, A. B. Lodge, R. Stephenson, R. Mutikainen, I. Suni, and J. Morse. A gas microstrip detector for X-ray imaging with readout of the anode by resistive division. *Nucl. Instrum. Methods Phys. Res., Sect. A*, 477(1-3):29 – 36, 2002.
- [45] F. Sauli. GEM: A new concept for electron amplification in gas detectors. *Nucl. Instrum. Methods Phys. Res., Sect. A*, 386(2-3):531 – 534, 1997.
- [46] F. Sauli. Progress with the gas electron multiplier. *Nucl. Instrum. Methods Phys. Res., Sect. A*, 522(1-2):93 – 98, 2004. TRDs for the Third Millenium. Proceedings of the 2nd Workshop on Advanced Transition Radiation Detectors for Accelerator and Space Applications.
- [47] A. Bressan, R. de Oliveira, A. Gandi, J. C. Labbé, L. Ropelewski, F. Sauli, D. Mörmann, T. Müller, and H. J. Simonis. Two-dimensional readout of GEM detectors. *Nucl. Instrum. Methods Phys. Res., Sect. A*, 425(1-2):254 – 261, 1999.
- [48] B. Ketzer, Q. Weitzel, S. Paul, F. Sauli, and L. Ropelewski. Performance of triple GEM tracking detectors in the COMPASS experiment. *Nucl. Instrum. Methods Phys. Res., Sect. A*, 535(1-2):314 – 318, 2004. Proceedings of the 10th International Vienna Conference on Instrumentation.
- [49] S. Lami, G. Latino, E. Oliveri, L. Ropelewski, and N. Turini. A triple-GEM telescope for the TOTEM experiment. *Nucl. Phys. B Proc. Suppl.*, 172:231 – 233, 2007. Proceedings of the 10th Topical Seminar on Innovative Particle and Radiation Detectors, Proceedings of the 10th Topical Seminar on Innovative Particle and Radiation Detectors.
- [50] A. Balla, G. Bencivenni, S. Cerioni, P. Ciambrone, E. De Lucia, G. De Robertis, D. Domenici, G. Felici, M. Gatta, M. Jacewicz, N. Lacalamita, S. Lauciani, R. Liuzzi, F. Loddo, M. Mongelli, G. Morello, A. Pelosi, M. Pistilli, L. Quintieri, A. Ranieri, and V. Valentino. Status of the cylindrical-GEM project for the KLOE-2 inner tracker. *Nucl. Instrum. Methods Phys. Res., Sect. A*, 628(1):194 – 198, 2011. VCI 2010 - Proceedings of the 12th International Vienna Conference on Instrumentation.
- [51] S. D. Pinto, M. Alfonsi, I. Brock, G. Croci, E. David, R. de Oliveira, L. Ropelewski, M. van Stenis, H. Taureg, and M. Villa. Spherical gems for parallax-free detectors. In *Nuclear Science Symposium Conference Record (NSS/MIC), 2009 IEEE*, pages 225 –230, 2009.
- [52] R. Chechik and A. Breskin. Advances in gaseous photomultipliers. *Nucl. Instrum. Methods Phys. Res., Sect. A*, 595(1):116 – 127, 2008. RICH 2007 - Proceedings of the Sixth International Workshop on Ring Imaging Cherenkov Detectors.

- [53] F. Sauli, T. Meinschad, L. Musa, and L. Ropelewski. Photon detection and localization with GEM. In *Nuclear Science Symposium Conference Record, 2004 IEEE*, volume 1, pages 12 – 15 Vol. 1, 2004.
- [54] A. Buzulutskov, A. Breskin, R. Chechik, G. Garty, F. Sauli, and L. Shekhtman. The GEM photomultiplier operated with noble gas mixtures. *Nucl. Instrum. Methods Phys. Res., Sect. A*, 443(1):164 – 180, 2000.
- [55] A. Breskin, A. Buzulutskov, and R. Chechik. GEM photomultiplier operation in CF4. *Nucl. Instrum. Methods Phys. Res., Sect. A*, 483(3):670 – 675, 2002.
- [56] J. F. C. A. Veloso, J. M. F. dos Santos, and C. A. N. Conde. A proposed new microstructure for gas radiation detectors: The microhole and strip plate. *Rev. Sci. Instrum.*, 71(6):2371–2376, 2000.
- [57] H. Natal da Luz, J. F. C. A. Veloso, F. D. Amaro, L. F. Requicha Ferreira, J. M. F. dos Santos, A. Breskin, and R. Chechik. MHSP operation in pure xenon. *Nucl. Instrum. Methods Phys. Res., Sect. A*, 552(3):259 – 262, 2005.
- [58] J. M. Maia, D. Mörmann, A. Breskin, R. Chechik, J. F. C. A. Veloso, and J. M. F. dos Santos. Avalanche-ion back-flow reduction in gaseous electron multipliers based on GEM/MHSP. *Nucl. Instrum. Methods Phys. Res., Sect. A*, 523(3):334 – 344, 2004.
- [59] J. F. C. A. Veloso, C. C. Caldas, C. A. B. Oliveira, C. D. R. Azevedo, J. M. F. dos Santos, A. Breskin, and R. Chechik. High-rate operation of the Micro-Hole and Strip Plate gas detector. *Nucl. Instrum. Methods Phys. Res., Sect. A*, 580(1):362 – 365, 2007. Proceedings of the 10th International Symposium on Radiation Physics - ISRP 10.
- [60] H. Natal da Luz, C. Oliveira, C. Azevedo, J. A. Mir, R. de Oliveira, J. dos Santos, and J. F. C. Veloso. Single Photon Counting X-Ray Imaging System Using a Micro Hole and Strip Plate. *IEEE Trans. Nucl. Sci.*, 55(4):2341 – 2345, 2008.
- [61] C. A. B. Oliveira, C. A. Santos, L. F. Carramate, A. L. M. Silva, N. da Luz, J. M. F. dos Santos, and J.F.C.A. Veloso. Energy Weighting in a 2D-MHSP X-Ray Single Photon Detector. *IEEE Trans. Nucl. Sci.*, 57(3):938 – 943, 2010.
- [62] L. F. N. D. Carramate, C. A. B. Oliveira, A. L. M. Silva, A. M. da Silva, J. M. F. dos Santos, and J. F. C. A. Veloso. Energy weighting technique in Quantum Computed Tomography using a MPGDI. *J. Instrum.*, 6(02):C02002, 2011.
- [63] C. A. N. Conde and A. J. P. L. Policarpo. A gas proportional scintillation counter. *Nucl. Instrum. Methods*, 53:7 – 12, 1967.
- [64] J. F. C. A. Veloso, J. A. M. Lopes, J. M. F. dos Santos, and C. A. N. Conde. A microstrip gas chamber as a VUV photosensor for a xenon gas proportional scintillation counter. *IEEE Trans. Nucl. Sci.*, 43(3):1232 – 1236, 1996.

- [65] K. Tsuji, J. Inhuk, and R. V. Grieken. *X-Ray Spectrometry: Recent Technological Advances*. John Wiley & Sons, Ltd, 2004.
- [66] M. Moszynski, M. Szawlowski, M. Kapusta, and M. Balcerzyk. Large area avalanche photodiodes in scintillation and X-rays detection. *Nucl. Instrum. Methods Phys. Res., Sect. A*, 485(3):504 – 521, 2002.
- [67] C. M. B. Monteiro, L. M. P. Fernandes, J. A. M. Lopes, L. C. C. Coelho, J. F. C. A. Veloso, J. M. F. dos Santos, K. Giboni, and E. Aprile. Secondary scintillation yield in pure xenon. *J. Instrum.*, 2(05):P05001, 2007.
- [68] C. M. B. Monteiro, J. A. M. Lopes, J. F. C. A. Veloso, and J. M. F. dos Santos. Secondary scintillation yield in pure argon. *Phys. Lett. B*, 668(3):167 – 170, 2008.
- [69] A. S. Conceição, L. F. Requicha Ferreira, L. M. P. Fernandes, C. M. B. Monteiro, L. C. C. Coelho, C. D. R. Azevedo, J. F. C. A. Veloso, J. A. M. Lopes, and J. M. F. dos Santos. GEM scintillation readout with avalanche photodiodes. *J. Instrum.*, 2(09):P09010, 2007.
- [70] J. M. F. dos Santos, J. A. M. Lopes, J. F. C. A. Veloso, P. C. P. S. Simes, T. H. V. T. Dias, F. P. Santos, P. J. B. M. Rachinhas, L. F. Requicha Ferreira, and C. A. N. Conde. Development of portable gas proportional scintillation counters for x-ray spectrometry. *X-Ray Spectrom.*, 30(6):373–381, 2001.
- [71] G. Charpak, S. Majewski, and F. Sauli. The scintillating drift chamber: A new tool for high-accuracy, very-high-rate particle localization. *Nucl. Instrum. Methods*, 126(3):381 – 389, 1975.
- [72] A. Bolozdynya, V. Egorov, A. Koutchenkov, G. Safronov, G. Smirnov, S. Medved, and V. Morgunov. A high pressure xenon self-triggered scintillation drift chamber with 3D sensitivity in the range of 20-140 keV deposited energy. *Nucl. Instrum. Methods Phys. Res., Sect. A*, 385(2):225 – 238, 1997.
- [73] L. C. C. Coelho, J. F. C. A. Veloso, D. S. Covita, L. F. Requicha Ferreira, and J. M. F. dos Santos. High-pressure operation of a xenon-GPSC/MSGC hybrid detector for hard X-ray spectrometry. *Nucl. Instrum. Methods Phys. Res., Sect. A*, 569(3):796 – 802, 2006.
- [74] C. D. R. Azevedo, A. L. M. Silva, A. L. Ferreira, H. Natal da Luz, L. M. Moutinho, J. M. F. dos Santos, and J. F. C. A. Veloso. 2D-sensitive hpxe gas proportional scintillation counter concept for nuclear medical imaging purposes. *J. Instrum.*, 6(01):C01067, 2011.
- [75] J. F. C. A. Veloso, F. D. Amaro, J. M. F. dos Santos, A. Breskin, A. Lyashenko, and R. Chechik. The Photon-Assisted Cascaded Electron Multiplier: a concept for potential avalanche-ion blocking. *J. Instrum.*, 1(08):P08003, 2006.
- [76] J. F. C. A. Veloso, F. D. Amaro, C. D. R. Azevedo, J. M. F. dos Santos, A. Breskin, A. Lyashenko, and R. Chechik. PACEM: a new concept for high avalanche-ion blocking. *Nucl. Instrum. Methods Phys. Res., Sect. A*, 581(1-2):261 – 264,

2007. VCI 2007 - Proceedings of the 11th International Vienna Conference on Instrumentation.
- [77] J. L. Campbell and K. W. D. Ledingham. Pulse height distributions from proportional counters. *Br. J. Appl. Phys.*, 17(6):769, 1966.
 - [78] D. G. Simons and P. A. J. de Korte. Soft X-ray energy resolution and background rejection in a driftless gas scintillation proportional counter. *Nucl. Instrum. Methods Phys. Res., Sect. A*, 277(2-3):642 – 656, 1989.
 - [79] I. I. Sobelman. *Atomic spectra and radiative transitions, 2nd Edition*. Springer-Verlag, 1992.
 - [80] G. Racah. On a New Type of Vector Coupling in Complex Spectra. *Phys. Rev.*, 61(7-8):537, 1942.
 - [81] et al. Y. Ralchenko. NIST Atomic Spectra Database (ver. 4.0.0), <http://www.nist.gov/physlab/data/asd.cfm> [2010, September 9].
 - [82] NIST, Basic Atomic Spectroscopic Data, <http://www.nist.gov/physlab/data/handbook/index2.cfm> [2011, March 15].
 - [83] NIST, Persistent Lines of Neutral Neon (Ne I), <http://physics.nist.gov/PhysRefData/Handbook/Tables/neontable3.htm> [2011, July 05].
 - [84] NIST, Persistent Lines of Neutral Argon (Ar I), <http://physics.nist.gov/PhysRefData/Handbook/Tables/argontable3.htm> [2011, July 05].
 - [85] NIST, Persistent Lines of Neutral Krypton (Kr I), <http://physics.nist.gov/PhysRefData/Handbook/Tables/kryptontable3.htm> [2011, July 05].
 - [86] NIST, Persistent Lines of Neutral Xenon (Xe I), <http://physics.nist.gov/PhysRefData/Handbook/Tables/xenontable3.htm> [2011, July 05].
 - [87] L. G. H. Huxley, R. W. Crompton, and M. T. Elford. Use of the parameter E/N. *Br. J. Appl. Phys.*, 17(9):1237, 1966.
 - [88] H. Katori and F. Shimizu. Lifetime measurement of the $1s_5$ metastable state of argon and krypton with a magneto-optical trap. *Phys. Rev. Lett.*, 70(23):3545–3548, 1993.
 - [89] M. Walhout, A. Witte, and S. L. Rolston. Precision measurement of the metastable $6s$ $[3/2]_2$ lifetime in xenon. *Phys. Rev. Lett.*, 72(18):2843–2846, 1994.
 - [90] M. Walhout, U. Sterr, A. Witte, and S. L. Rolston. Lifetime of the metastable $6s'$ $[\frac{1}{2}]0$ clock state in xenon. *Opt. Lett.*, 20(10):1192–1194, 1995.

- [91] N. D. Bhaskar and A. Lurio. Lifetime of the $1s_2$ ($^1P_{11}$) and $1s_4$ (3P_1) levels of neon by the cascade Hanle effect. *Phys. Rev. A*, 13(4):1484–1496, 1976.
- [92] G. M. Lawrence. Radiance Lifetimes in the Resonance Series of Ar I. *Phys. Rev.*, 175(1):40–44, 1968.
- [93] P. G. Wilkinson. Oscillator strengths of the resonance lines of the rare gases—I. Krypton. *J. Quant. Spectrosc. Radiat. Transfer*, 5(3):503 – 510, 1965.
- [94] D. Kent Anderson. Lifetimes of the $(5p^56s)^1P_1$ and 3P_1 States of Xenon. *Phys. Rev.*, 137(1A):A21–A26, 1965.
- [95] M. Suzuki and S. Kubota. Mechanism of proportional scintillation in argon, krypton and xenon. *Nucl. Instrum. Methods*, 164(1):197 – 199, 1979.
- [96] Y. Tanaka. Continuous Emission Spectra of Rare Gases in the Vacuum Ultraviolet Region. *J. Opt. Soc. Am.*, 45(9):710–713, 1955.
- [97] Y. Tanaka, A. S. Jursa, and F. J. Leblanc. Continuous Emission Spectra of Rare Gases in the Vacuum Ultraviolet Region. II. Neon and Helium. *J. Opt. Soc. Am.*, 48(5):304–307, 1958.
- [98] P. K. Leichner, K. F. Palmer, J. D. Cook, and M. Thieneman. Two- and three-body collision coefficients for $Xe(^3P_1)$ and $Xe(^3P_2)$ atoms and radiative lifetime of the $Xe_2(1_u)$ molecule. *Phys. Rev. A*, 13(5):1787–1792, 1976.
- [99] R. Boucqué and P. Mortier. On the production and the decay of delayed molecular ultraviolet radiation in rare gas Townsend discharges. *J. Phys. D: Appl. Phys.*, 3(12):1905, 1970.
- [100] M. S. B. Munson, J. L. Franklin, and F. H. Field. A Mass Spectrometric study of Homonuclear and Heteronuclear Rare Gas Molecule Ions. *J. Phys. Chem.*, 67(7):1542–1548, 1963.
- [101] R. E. Huffman and D. H. Katayama. Photoionization Study of Diatomic-Ion Formation in Argon, Krypton, and Xenon. *J. Chem. Phys.*, 45(1):138–146, 1966.
- [102] R. S. Mulliken. Potential Curves of Diatomic Rare-Gas Molecules and Their Ions, with Particular Reference to Xe_2 . *J. Chem. Phys.*, 52(10):5170–5180, 1970.
- [103] H. A. Koehler, L. J. Ferderber, D. L. Redhead, and P. J. Ebert. Vacuum-ultraviolet emission from high-pressure xenon and argon excited by high-current relativistic electron beams. *Phys. Rev. A*, 9(2):768–781, 1974.
- [104] J. W. Keto, R. E. Gleason, and G. K. Walters. Production Mechanisms and Radiative Lifetimes of Argon and Xenon Molecules Emitting in the Ultraviolet. *Phys. Rev. Lett.*, 33(23):1365–1368, 1974.
- [105] G. M. Barrow. *Introduction to Molecular Spectroscopy*. McGraw-Hill International Editions, 1962.

- [106] C. N. Banwell. *Fundamentals of Molecular Spectroscopy, 3rd Edition.* McGraw-Hill International Editions, 1972.
- [107] A. Morozov, T. Heindl, R. Krucken, A. Ulrich, and J. Wieser. Conversion efficiencies of electron beam energy to vacuum ultraviolet light for Ne, Ar, Kr, and Xe excited with continuous electron beams. *J. Appl. Phys.*, 103(10):103301, 2008.
- [108] F. P. Santos, T. H. V. T. Dias, P. J. B. M. Rachinhas, A. D. Stauffer, and C. A. N. Conde. The electroluminescence of Xe-Ne gas mixtures: a Monte Carlo simulation study. *IEEE Trans. Nucl. Sci.*, 45(2):176 –185, 1998.
- [109] F. P. Santos, T. H. V. T. Dias, A. D. Stauffer, and C. A. N. Conde. Three-dimensional Monte Carlo calculation of the VUV electroluminescence and other electron transport parameters in xenon. *J. Phys. D: Appl. Phys.*, 27(1):42, 1994.
- [110] T. H. V. T. Dias, A. D. Stauffer, and C. A. N. Conde. A unidimensional Monte Carlo simulation of electron drift velocities and electroluminescence in argon, krypton and xenon. *J. Phys. D: Appl. Phys.*, 19(4):527, 1986.
- [111] M. Salete, S. C. P. Leite, A. J. P. L. Policarpo, M. Alegria Feio, and M. A. F. Alves. Detection of VUV photons with a photoionization proportional scintillation chamber. *Nucl. Instrum. Methods*, 179(2):295 – 300, 1981.
- [112] M. Suzuki, J. Ruan(Gen), and S. Kubota. Time dependence of the recombination luminescence from high-pressure argon, krypton and xenon excited by alpha particles. *Nucl. Instrum. Methods Phys. Res.*, 192(2-3):565 – 574, 1982.
- [113] P. Lindblom and O. Solin. Atomic near-infrared noble gas scintillations I: Optical spectra. *Nucl. Instrum. Methods Phys. Res., Sect. A*, 268(1):204 – 208, 1988.
- [114] J. W. Keto and Chien-Yu Kuo. Cascade production of Ar(3p⁵4p) following electron bombardment. *J. Chem. Phys.*, 74(11):6188–6196, 1981.
- [115] M. M. F. R. Fraga, F. A. F. Fraga, and A. J. P. L. Policarpo. Modelling of an IR scintillation counter. *Nucl. Instrum. Methods Phys. Res., Sect. A*, 442(1-3):423 – 427, 2000.
- [116] G. Bressi, G. Carugno, E. Conti, D. Iannuzzi, and A. T. Meneguzzo. A first study of the infrared emission in argon excited by ionizing particles. *Phys. Lett. A*, 278(5):280 – 285, 2001.
- [117] A. Buzulutskov, A. Bondar, and A. Grebenuk. Infrared scintillation yield in gaseous and liquid argon. *Europhys. Lett.*, 94(5):52001, 2011.
- [118] Garfield++ – simulation of tracking detectors,
<http://cern.ch/garfieldpp> [2011, March 15].
- [119] Magboltz – transport of electrons in gas mixtures
<http://cern.ch/magboltz> [2011, March 15].

- [120] Garfield - simulation of gaseous detectors, <http://cern.ch/garfield> [2011, May 16].
- [121] S. Mukhopadhyay and N. Majumdar. A study of three-dimensional edge and corner problems using the neBEM solver. *Eng. Anal. Boundary Elem.*, 33(2):105 – 119, 2009.
- [122] S. F. Biagi. Monte Carlo simulation of electron drift and diffusion in counting gases under the influence of electric and magnetic fields. *Nucl. Instrum. Methods Phys. Res., Sect. A*, 421(1-2):234 – 240, 1999.
- [123] Electron Scattering Database, <http://www.lxcat.laplace.univ-tlse.fr/> [2011, July 08].
- [124] H. R. Skallerud. The stochastic computer simulation of ion motion in a gas subjected to a constant electric field. *J. Phys. D: Appl. Phys.*, 1(11):1567, 1968.
- [125] J. E. Furst, D. E. Golden, M. Mahgerefteh, Jiaxiang Zhou, and D. Mueller. Absolute low-energy e^- -Ar scattering cross sections. *Phys. Rev. A*, 40(10):5592– 5600, 1989.
- [126] O. Zatsarinny, K. Bartschat, and M. Allan. High-resolution experiments and B -spline R -matrix calculations for elastic electron scattering from krypton. *Phys. Rev. A*, 83(3):032713, 2011.
- [127] A. Okhrimovskyy, A. Bogaerts, and R. Gijbels. Electron anisotropic scattering in gases: A formula for Monte Carlo simulations. *Phys. Rev. E*, 65(3):037402, 2002.
- [128] G. G. Raju. *Gaseous Electronics: Theory and Practice*. Taylor and Francis, 2006.
- [129] S. Agostinelli and et al. G4 – a simulation toolkit. *Nucl. Instrum. Methods Phys. Res., Sect. A*, 506(3):250 – 303, 2003.
- [130] J. Allison and et al. Geant4 developments and applications. *IEEE Trans. Nucl. Sci.*, 53(1):270 – 278, 2006.
- [131] ROOT – A Data Analysis Framework, <http://root.cern.ch/> [2011, July 12].
- [132] D. Nygren. Is it possible to surpass the intrinsic energy resolution of xenon? Talk presented at the 5th Symposium on Large TPCs for Low Energy Rare Event Detection, Paris – France, 14-17 December 2010.
- [133] Ö Şahin, İ Tapan, E N Özmutlu, and R Veenhof. Penning transfer in argon-based gas mixtures. *J. Instrum.*, 5(05):P05002, 2010.
- [134] T. H. V. T. Dias, F. P. Santos, P. J. B. M. Rachinhas, F. I. G. M. Borges, J. M. F. dos Santos, C. A. N. Conde, and A. D. Stauffer. Xenon-neon gas proportional scintillation counters: Experimental and simulation results. *J. Appl. Phys.*, 85(9):6303–6312, 1999.

- [135] D. Nygren. High-pressure xenon gas electroluminescent TPC for $\nu^0\beta\beta$ - decay search. *Nucl. Instrum. Methods Phys. Res., Sect. A*, 603(3):337 – 348, 2009.
- [136] M. Gai, D. N. McKinsey, K. Ni, D. A. R. Rubin, T. Wongjirad, R. Alon, A. Breskin, M. Cortesi, and J. Miyamoto. Toward Application of a Thick Gas Electron Multiplier (THGEM) Readout for a Dark Matter Detector. *ArXiv:0706.1106v1 [physics.ins-det]*, 2007.
- [137] F. Balau, V. Solovov, V. Chepel, A. Pereira, and M. I. Lopes. GEM operation in double-phase xenon. *Nucl. Instrum. Methods Phys. Res., Sect. A*, 598(1):126 – 129, 2009. Instrumentation for Colliding Beam Physics - Proceedings of the 10th International Conference on Instrumentation for Colliding Beam Physics.
- [138] C. M. B. Monteiro, A. S. Conceição, F. D. Amaro, J. M. Maia, A. C. S. S. M. Bento, L. F. R. Ferreira, J. F. C. A. Veloso, J. M. F. dos Santos, A. Breskin, and R. Chechik. Secondary scintillation yield from gaseous micropattern electron multipliers in direct Dark Matter detection. *Phys. Lett. B*, 677:133, 2009.
- [139] ANSYS, <http://www.ansys.com/> [2011, Ago 27].
- [140] Singiresu S. RAO. *The Finite Element Method in Engineering, 5th Edition*. Elsevier, 2011.
- [141] R. Veenhof. Numerical methods in the simulation of gas-based detectors. *J. Instrum.*, 4(12):P12017, 2009.
- [142] M. Redshaw, E. Wingfield, J. McDaniel, and E. G. Myers. Mass and Double-Beta-Decay Q Value of ^{136}Xe . *Phys. Rev. Lett.*, 98(5):053003, 2007.